Reduction of acoustic fields of horn-like structures by optimization of network resonators

Bin Wang

UNIVERSITÉ PARIS-EST

École doctorale Sciences, Ingénierie et Environnement

THÈSE de doctorat
Discipline : Mécanique

Présentée par:

Bin WANG

Sujet de la thèse :

REDUCTION OF ACOUSTIC FIELDS OF HORN-LIKE STRUCTURES BY OPTIMIZATION OF NETWORK RESONATORS

Soutenue publiquement le DD MM YY devant un jury composé de :

M. Mabrouk BEN TAHAR	Université de Technologie de Compiègne	Examinateur
M. Michel BERENGIER	IFSTTAR	Rapporteur
M. Denis DUHAMEL	Ecole des Ponts ParisTech	Directeur de thèse
M. Philippe KLEIN	IFSTTAR	Examinateur
M. Vincent PAGNEUX	Université du maine	Rapporteur

Résumé

Le bruit généré dans la zone de contact entre un pneumatique et une route peut être amplifié par des dièdres constitués des surfaces du pneumatique et la route. Cette étude est consacrée à l'optimisation et à la conception de bandes de roulement et de textures de la route pour réduire l'amplification de l'effet dièdre sur la base de l'annulation de sons. Les bandes de roulement et les textures de la route peuvent être considérées comme deux réseaux dans la zone de contact. Les surfaces du pneumatique et de la route peuvent être considérées comme des baffles. Un modèle de réseau à baffle est constitué pour le système pneumatique / chaussée, et des procédés de couplage multi-domaines sont développés pour le calcul des champs acoustiques autour des réseaux à baffles. Avec ce modèle, la réduction des amplifications de l'effet dièdre par les réseaux peut être estimée. Étant donné que les réductions sont autour des fréquences de résonance de l'air à l'intérieur des réseaux, des méthodes numériques simples pour estimer les fréquences de résonance sont développées. Afin de concevoir des réseaux pour obtenir les fréquences de résonance recherchées, une méthode d'optimisation sur la base des algorithmes génétiques est proposée. Les méthodes d'estimation des fréquences de résonance sont validées avec des mesures. Les méthodes d'optimisation et le modèle des réseaux bafflés sont également vérifiées par les expériences. Une structure avec un cylindre en bois et une feuille de contreplaqué est construite pour les validations. Un vrai pneumatique sur une feuille de contreplaqué est également mesuré et calculé avec les méthodes proposées. Les bandes de roulement sont optimisées avec les méthodes proposées. Plusieurs réductions des amplifications de l'effet dièdre peuvent être vues et sont estimées avec les méthodes de couplage multi-domaines. La dimension des motifs de texture de la route est également étudiée afin de trouver les réductions maximales des amplifications.

Mots clés : Bruit; Pneumatique; Route; Effet dièdre; Résonance; Correction de longueur; Résonateur acoustique; Sculpture; Texture; Optimisation.

Abstract

The noise generated in the contact zone between a tire and a road can be amplified by horns constituted of the surfaces of the tire and the road. This study is devoted to the optimization and the design of tire treads and road textures for reducing the amplification of horn effect based on the sound cancellation. The tire treads and the road textures can be considered as two dimensional networks in the contact zone. The surfaces of the tire and the road can be seen as flanges. A model of flanged networks is established for the tire/road system, and multi-domain coupling methods are developed for the calculation of the acoustic fields around the flanged networks. With this model the reductions of the amplifications of horn effect by the networks can be estimated. Since the reductions are around the resonant frequencies of air inside the networks, simple numerical methods for estimating the resonant frequencies are developed. In order to design the networks to get wanted resonant frequencies, an optimization method based on genetic algorithms is proposed. The methods for estimating the resonant frequencies are validated with measurements. The optimization methods and the model of the flanged networks are also proved to be effective by the experiments. The wooden networks between a wooden cylinder and a sheet of plywood are built for the validation. A real tire on a sheet of plywood is also measured and calculated with the proposed methods. Last the tire treads are optimized with the optimization methods. Multiple reductions of the amplifications of horn effect can be seen and are estimated with the multi-domain coupling methods. The road brick dimension is also investigated in order to find the maximum reductions of the amplifications.

Keywords: Noise; Tire; Road; Horn effect; Pipe resonance; End correction; Acoustic network resonator; Tire treads; Road textures; Optimization.

Long Résumé

Le bruit généré par le trafic automobile est responsable d'une grande partie de la pollution de l'environnement sonore. Grace à la technologie moderne, le bruit des moteurs de voiture et d'autres pièces mécaniques a été considérablement réduit. Par conséquent, le bruit des pneumatiques en interaction avec la route est de plus en plus perceptible. Au-dessus d'une vitesse de $50km/h$, le bruit généré par les pneumatiques roulant sur la route est le bruit dominant [1]. Le bruit des pneumatiques de poids-lourds domine également lorsque la vitesse est supérieure à $80km/h$. Ainsi une réduction de la génération du bruit de contact pneumatique / chaussée va grandement améliorer l'environnement en bordure de route et la qualité de vie associée.

Il est essentiel de comprendre les mécanismes de génération du bruit de contact pneumatique / chaussée pour faciliter la recherche de sa réduction sans compromettre la sécurité routière. Ainsi, les mécanismes de la génération et du rayonnement du bruit de roulement provoqué par l'interaction entre un pneumatique et la surface d'une route ont reçu une attention considérable au cours des dernières décennies. Les phénomènes physiques responsables de la génération et du rayonnement du bruit de contact pneumatique / chaussée sont bien connus, et sont essentiellement les vibrations de pneumatiques, le pompage d'air, l'effet dièdre et les résonances d'air.

L'objectif de cette étude est concentré sur la réduction de l'effet dièdre par la résonance de l'air à l'intérieur des conduits entre le pneumatique et la route. Le bruit généré dans la zone de contact peut être amplifié par les dièdres comprenant des surfaces du pneumatique et de la route. Les recherches antérieures sur l'effet dièdre ont seulement considéré un pneumatique et une route lisses. Dans ce travail, nous prenons en compte les bandes de roulement et les textures de la route dans cet effet dièdre. Le couplage entre les résonances de l'air et l'effet dièdre sera étudié dans le même modèle.

Un modèle de réseau bafflé est établi pour calculer les champs acoustiques dans le système pneumatique / chaussée. Les bandes de roulement et la texture de la route peuvent être considérées comme deux réseaux tridimensionnels dans la zone

de contact entre le pneumatique et la route. Les surfaces du pneumatique et de la route peuvent être considérées comme des baffles. Dans ce modèle à la fois l'effet dièdre et la résonance de l'air sont pris en compte. Il peut être utilisé pour estimer la réduction de l'effet dièdre en utilisant les résonateurs du réseau. L'impédance de rayonnement peut être pris en compte à l'extrémité d'un tuyau. En calculant un simple tuyau droit à bride avec les méthodes d'impédance de rayonnement, la description physique de la propagation des ondes et l'interaction entre les champs acoustiques en dehors de la structure et à l'intérieur du tuyau sont présentés clairement. Pour des baffles et des réseaux complexes les méthodes de couplage multi-domaines sont proposées pour obtenir les solutions. Dans les procédés de couplage multi-domaine, le domaine acoustique est divisé en sous-domaines extérieur et intérieur, sous-domaines qui sont couplés aux interfaces entre eux par la continuité de la pression et de la vitesse. Nous utilisons des méthodes d'éléments de frontières pour obtenir un système d'équations pour le sous-domaine extérieur. Si le sous-domaine intérieur est un tuyau droit, nous pouvons utiliser la matrice de transfert pour le résoudre. La théorie de Miles [2] est adaptée pour calculer deux jonctions de réseau tridimensionnel, on peut donc combiner la matrice de transfert et la théorie de Miles pour résoudre un réseau complexe. Les méthodes numériques (telles que les méthodes d'éléments de frontière et les méthodes d'éléments finis) peuvent être utilisées pour des réseaux tridimensionnels. Bien entendu, les méthodes numériques peuvent également être appliquées à des cas à une ou deux dimensions. En résolvant le problème couplé, la pression et la vitesse sur l'ensemble de la frontière peuvent être obtenues. Puis, les champs acoustiques peuvent être calculés par une formule intégrale. Les formes de tuyau en T sont résolus par la méthode des éléments de frontière et les méthodes de couplage multi-domaines. De bons accords entre ces méthodes prouvent la fiabilité des méthodes de couplage multi-domaines. Comme pour les deux réseaux tridimensionnels, les procédés de couplage multi-domaine permettent de ne pas mailler le réseau, ils sont plus efficaces que les méthodes d'éléments de frontière. Les pertes dues aux conductivités visqueuses et thermiques à la paroi du tube peuvent être prises en compte dans les méthodes de couplage multi-domaines afin d'améliorer la précision des solutions. Un tuyau droit à bride et un réseau bridé sont calculés pour comparer les méthodes de couplage multi-domaine avec et sans pertes.

D'importantes réductions des amplifications de l'effet dièdre peuvent être vues autour des fréquences de résonance. Par conséquent des méthodes numériques simples (méthode des éléments finis) pour estimer les fréquences de résonance de l'air à l'intérieur des réseaux sont développées. Il n'est pas nécessaire de calculer les champs acoustiques à l'extérieur des baffles pour obtenir les fréquences de résonance, ce qui

est consommateur de temps de calcul. Nous pouvons obtenir les fréquences de résonance facilement en résolvant un problème de valeurs propres par la méthode des éléments finis. Nous avons développé un programme à cet effet dans lequel nous devons saisir les paramètres tels que la dimension de réseau, les conditions aux limites et ou les corrections de longueur. Puisque les réseaux bridés non seulement ont des extrémités fermées, mais aussi des extrémités ouvertes, les corrections d'extrémité aux extrémités ouvertes doivent être calculées en premier. Ces corrections seront utilisées dans l'estimation des fréquences de résonance. Basé sur les méthodes numériques (méthodes d'éléments de frontière) proposées dans [3], les corrections des extrémités ouvertes bafflées peuvent être obtenues. Les fréquences de résonance de plusieurs réseaux à brides sont estimées par nos méthodes proposées et comparées avec les résultats de champs acoustiques à partir desquels nous pouvons aussi voir les fréquences de résonance. De bons accords peuvent être observés.

Pour un réseau spécifié, nos méthodes peuvent donner les fréquences de résonance. Toutefois, si nous concevons le réseau pour obtenir les fréquences de résonance recherchées, une méthode d'optimisation des structures de réseau est nécessaire. Les fréquences de résonance dépendent de la structure du réseau. Un procédé d'optimisation sur la base des algorithmes génétiques et des méthodes d'estimation pour des fréquences de résonance est développé à cet effet. Les paramètres de la dimension de réseau tels que les types de jonction, les positions de jonction et la surface de section transversale peuvent être optimisés. Nous choisissons trois types de jonctions pour construire le réseau: un T tourné vers la gauche, un T tourné vers la droite et une jonction en croix. Deux fonctions objectifs sont définies. L'une est pour une seule fréquence de résonance déterminée, et l'autre est pour un nombre maximal de fréquences de résonance dans une plage de fréquences spécifiée. Avec cette méthode, les deux réseaux tridimensionnels avec la fréquence cible ou le nombre maximal de fréquences de résonance dans une bande de fréquences peuvent être trouvés. Nous pouvons réduire les amplifications de l'effet dièdre autour de ces fréquences de résonance optimisées. Plusieurs exemples d'optimisation de deux réseaux avec et sans baffles sont donnés.

Le modèle proposé, les méthodes de calcul, les méthodes d'estimation pour les fréquences de résonance et les méthodes d'optimisation sont validés avec des mesures de plusieurs tuyaux bafflés en bois et un vrai pneumatique. D'abord un guide d'onde droit en bois et un réseau en bois entre un cylindre de bois et une feuille de contreplaqué sont respectivement mesurés. Les tendances concernant la pression sonore sont similaires aux résultats prédits par les méthodes de couplage multi-domaine, et de bons accords entre les résultats mesurés et prévus peuvent être vus. Les fréquences

de résonance sont très proches des estimations. Ensuite, le réseau est optimisé afin d'obtenir un nombre maximum de fréquences de résonance inférieures à $2000Hz$. Quatre fréquences de résonance peuvent être trouvées. Nous avons calculé et mesuré les champs acoustiques pour l'un des réseaux optimisés. D'après les résultats prévus, nous pouvons voir les fréquences de résonance optimisées. Les résultats prédits concordent bien avec les résultats mesurés. Ensuite un réseau non bafflé est optimisé pour une des fréquences de résonance spécifiées. A partir des champs acoustiques mesurés, nous pouvons voir la fréquence de résonance ciblée qui est très proche de la fréquence de résonance prédite. Finalement un véritable pneumatique sur une surface plane est mesuré et calculé. En raison de l'erreur sur la longueur estimée de la zone de contact, les résultats prévus sont en accord partiel avec les résultats mesurés. Dans notre expérience, la zone de contact ne peut pas être pressée fermement sur le sol car la charge que l'on utilise est très inférieure à la charge d'un véhicule réel. Ainsi, la longueur de la zone de contact n'est pas vraiment estimée correctement.

Pour l'optimisation des bandes de roulement et de la texture de la route, nous supposons que le pneumatique peut être appuyé fermement sur la route dans la zone de contact. Les bandes de roulement sont optimisées de deux manières. Dans la première optimisation, on insère le réseau optimisé un par un pour les pics de fréquence ciblés. Dans la seconde optimisation, les réseaux optimisés ont un nombre maximum de fréquences de résonance inférieures à $2000Hz$. Pour les deux types de réseaux optimisés, de multiples réductions des amplifications de l'effet dièdre peuvent être vues à travers les calculs avec les méthodes de couplage multi-domaines. La dimension de la texture de route est étudiée afin de trouver les réductions maximales des amplifications de l'effet dièdre jusqu'à $2000Hz$. Le nombre maximum de fréquences de résonance que nous pouvons trouver est 3. Nous pouvons voir trois réductions claires des champs acoustiques calculés par les méthodes de couplage multi-domaines.

Long Summary

Noise generated by traffic is responsible for a great portion of environmental noise pollution. Thanks to modern technology, noise from car engines and other mechanical parts has been significantly reduced. Therefore, noise from tire and road interaction is becoming increasingly noticeable. Above the moderate speed of $50km/h$, the sound generated by the tires rolling over the road is the dominant noise [1]. Tire noise from trucks also dominates when the speed is higher than $80km/h$. Hence a reduction in tire/road noise generation will greatly improve the roadside environment and the associated quality of life.

It is essential to understand the mechanisms of noise generation to facilitate the search for quiet tire/road surface without compromising road safety. So the mechanisms of the generation and radiation of rolling noise caused by the interaction between a tire and the surface of a road have received considerable attention over the past few decades. The physical phenomena responsible for the generation and radiation of tire/road contact noise are well known, basically due to tire vibrations, air-pumping, horn effect and air resonances.

The focus of this study is put on the reduction of horn effect by the resonance of air inside the pipes between the tire and the road based on the sound cancellation. The noise generated in the contact zone can be amplified by the horns comprised of the surfaces of the tire and the road. Previous researches on the horn effect only investigate smooth tires and roads. In this work we take into account the tire treads and the road textures in the calculation of horn effect. The air resonances and horn effect will be studied in the same model.

A model of flanged networks is established for calculating the acoustic fields around the tire/road system. The tire treads and the road textures can be considered as two dimensional networks in the contact zone between the tire and the road. The surfaces of the tire and the road can be seen as flanges. In this model both the horn effect and the air resonance are taken into account. It can be used to estimate the reduction of the horn effect by using the network resonators. Radiation impedance can be

applied to the calculation of the simple flange and pipe. By computing a simple flanged straight pipe with the radiation impedance methods, the physical description of the wave propagation and the interaction between the acoustic fields outside the flange and inside the pipe are presented clearly. For the complex flanges and networks multi-domain coupling methods are proposed to get the solutions. In the multi-domain coupling methods, the acoustic domain is divided into an exterior subdomain and an interior subdomain which are coupled at the interfaces between them by the continuity of pressure and velocity. We use boundary element methods to get an equation system for the exterior subdomain. If the interior subdomain is one dimensional straight pipe, we can use transfer matrix to solve it. The theory of Miles [2] is suitable for calculating two dimensional network junctions, so we can combine the transfer matrix and the theory of Miles to solve a complex network. Numerical methods (such as boundary element methods and finite element methods) can be used for three dimensional networks. Of course the numerical methods can also be applied to the one and two dimensional cases. By solving the coupled problem, the pressure and velocity on the whole flange can be obtained. Then the acoustic fields can be calculated by an integral formula. A flanged T shaped pipe is solved by the boundary element method and multi-domain coupling methods. Good agreements between these methods prove the reliability of the multi-domain coupling methods. Since for two dimensional networks the multi-domain coupling methods don't use network meshes, they are more effective than boundary element methods. The viscous and thermal conductivity losses at the pipe walls can be taken into account in the multi-domain coupling methods in order to improve the accuracy of the solutions. A flanged straight pipe and a flanged network are calculated to compare the multi-domain coupling methods with and without losses.

Large reductions of the amplifications of horn effect can be seen around the resonant frequencies. Therefore simple numerical methods (finite element methods) for estimating the resonant frequencies of air inside the flanged networks are developed. It is not necessary to calculate the acoustic fields outside the flanges to get the resonant frequencies, which is quite time-consuming. We can get the resonant frequencies easily by solving an eigenvalue problem with the finite element method. We developed a program for this purpose where we should input the parameters such as the network dimension, boundary conditions and end corrections. Since the flanged networks not only have closed ends but also have open ends, the end corrections of the open ends should be calculated first. These end corrections will be used in the estimation of resonant frequencies. Based on the numerical methods (boundary element methods) proposed in [3], the corrections of the flanged open ends can be obtained. The resonant

frequencies of several flanged networks are estimated by our proposed methods and compared with the results of acoustic fields from which we can also see the resonant frequencies. Good agreements can be seen.

For a specified flanged network, our proposed methods can give the resonant frequencies. However, if we design the network to get the wanted resonant frequencies, optimization methods of the network structures are requisite. The resonant frequencies depend on the network structures. An optimization method based on genetic algorithms and the estimation methods for the resonant frequencies is developed for this purpose. Parameters of the network dimension such as junction types, junction positions and cross sectional area can be optimized. We choose three types of junctions to build the network: left T junction, right T junction and cross junction. Two objective functions are defined. One is for a single specified resonant frequency, and the other one is for the maximum number of resonant frequencies within a specified frequency range. With this method, the two dimensional networks with the targeted or the maximum number of resonant frequencies within a frequency range can be found. We can reduce the amplifications of horn effect around these optimized resonant frequencies. Several optimization examples of unflanged and flanged two dimensional networks are given.

The proposed model, computational methods, estimation methods for the resonant frequencies and the optimization methods are validated with measurements of several wooden flanged pipes and a real tire. First a straight wooden pipe and a wooden network between a wooden cylinder and a sheet of plywood are respectively measured. The tendencies of sound pressure are similar to the results predicted by the multi-domain coupling methods, and good agreements between the measured and predicted results can be seen. The resonant frequencies are very close to the estimations. Then the network is optimized in order to get a maximum number of resonant frequencies within $2000Hz$. Four resonant frequencies can be found. We calculated and measured the acoustic fields for one of the optimized networks. From the predicted results we can see the optimized resonant frequencies. The predicted results agree well with the measured results. Next an unflanged network is optimized for a specifed resonant frequencies. From the measured acoustic fields we can see the targeted resonant frequency that is very close to the predicted resonant frequency. Last a real tire on a plane surface is measured and calculated. Due to the error of the estimated length of the contact zone, the predicted results partly agree with the measured results. In our experiment, the contact zone may not be pressed firmly in the whole contact zone because the load that we use is much smaller than the load from a real car. So the length of the contact zone may not be estimated correctly.

For the optimization of the tire treads and the road textures, we assume that the tire can be pressed firmly on the road in the whole contact zone. The tire treads are optimized in two ways. In the first optimization, we insert the optimized networks one by one for the targeted peaks. In the second optimization, the optimized networks have a maximum number of resonant frequencies within $2000Hz$. For both types of optimized networks, multiple reductions of the amplifications of horn effect can be seen through the calculations with the multi-domain coupling methods. The road brick dimension is investigated in order to find the maximum reductions of the amplifications of horn effect within $2000Hz$. Since the maximum number of the resonant frequencies that we can find is 3, we can see three clear reductions from the acoustic fields computed by the multi-domain coupling methods.

Acknowledgement

I would like to start by thanking my supervisor, Doctor and Professor Denis Duhamel, for his insights, rigorous working attitude and constant guidance on my studies. I am really grateful for the opportunity of studying with him. I would also appreciate Dr. Honoré Yin for his helpful suggestions. Many thanks to Dr. Gwendal Cumunel and Mrs Anne Ferri for their assistances in conducting experiments. Great appreciation is also expressed to my parents for their warm care and support.

Lastly, I would like to take this opportunity to thank my wife, Mayao Cheng, for her great care and love.

Contents

Résumé **I**

Abstract **III**

Long Résumé **V**

Long Summary **IX**

Acknowledgement **XIII**

Contents **XVII**

List of Figures **XXIV**

List of Tables **XXV**

1 Introduction **1**

1.1 Tire/road noise 1

1.1.1 Mechanisms 2

1.1.2 Tire vibration and air pumping 3

1.1.3 Horn effects 4

1.2 Acoustic resonators 6

1.2.1 Straight tube resonator 7

1.2.2 Helmholtz resonator 9

1.2.3 T-pipe resonator 10

1.3 Acoustic radiation of baffled piston 11

1.3.1 Boundary element methods 11

1.3.2 Fast multipole boundary element methods 12

1.4 Optimization methods 13

1.5 Objective and Scope of Research 15

2 Modelling of networks in horn-like structures **17**
2.1 Introduction . . . 17
2.2 Problem specification . . . 19
2.2.1 Flanged network . . . 19
2.2.2 Wave propagation . . . 19
2.2.3 Boundary condition . . . 20
2.3 Radiation impedance methods . . . 21
2.4 Multi-domain coupling methods . . . 23
2.4.1 Exterior subdomain . . . 24
2.4.2 Interior subdomain . . . 25
2.5 Simulations . . . 30
2.5.1 Calculations without losses . . . 30
2.5.2 Calculations with losses . . . 38
2.6 Conclusions . . . 41

3 Calculation of network resonant frequencies **43**
3.1 Determination of end corrections . . . 43
3.1.1 Previous researches . . . 44
3.1.2 Numerical procedures . . . 44
3.1.3 Complex flanges and networks . . . 46
3.2 Resonant frequencies . . . 51
3.2.1 Analytical methods . . . 51
3.2.2 Numerical methods . . . 54
3.3 Examples of resonant frequencies . . . 56
3.3.1 T pipe . . . 56
3.3.2 Networks . . . 59
3.4 Conclusions . . . 63

4 Optimization of junctions and end positions of 2D networks **65**
4.1 Genetic algorithm . . . 66
4.1.1 Population Representation . . . 66
4.1.2 The objective and fitness functions . . . 67
4.1.3 Selection . . . 68
4.1.4 Crossover(Recombination) . . . 69
4.1.5 Mutation . . . 70
4.1.6 Reinsertion . . . 72
4.1.7 Termination of the GA . . . 72
4.2 Optimizations and designs of 2D networks . . . 72

4.2.1 Unflanged networks . . . 73
4.2.2 Network between a cylinder and a plane surface . . . 78
4.3 Conclusions . . . 80

5 Validations with measurements **81**
5.1 Sound pressure fields of pipes between a cylinder and a plane surface . 81
5.1.1 Point source . . . 83
5.1.2 Plane surface with or without a cylinder . . . 83
5.1.3 Straight pipe . . . 84
5.1.4 Network . . . 85
5.1.5 Optimized network . . . 87
5.2 Tire . . . 89
5.3 Conclusions . . . 94

6 Optimization of tire treads and road textures **97**
6.1 Acoustic excitations . . . 98
6.1.1 Comparison of excitations . . . 98
6.1.2 Point source position . . . 99
6.2 Optimization of tire treads . . . 101
6.2.1 Parallel networks . . . 101
6.2.2 Periodic networks . . . 102
6.3 Optimization of road textures . . . 105
6.3.1 Determination of end corrections . . . 106
6.3.2 Estimation of resonant frequencies . . . 108
6.3.3 Road dimensions . . . 110
6.3.4 Calculation of acoustic radiations . . . 111
6.4 Conclusions . . . 112

7 Conclusions and future work **115**
7.1 Conclusions . . . 115
7.2 Future work . . . 116

Bibliography **119**

List of Figures

1.1 Sound generation and enhancement mechanisms of tire/road noise [4] 2
1.2 Horn effect: multiple refections of sound in the horn-like structure . . 4
1.3 (a) Tire on the road; (b) Tire without the road. 5
1.4 Pipe resonators in the contact zone between a tire and a road 7
1.5 A sound absorbing wall with quarter-wave resonators. 8
1.6 Two axially coupled tubes. 9
1.7 T-shaped acoustic resonator. 10
1.8 A piston with an infinite baffle. 11
1.9 A simple example of a two dimensional wooden network with open and closed ends 14

2.1 (a) Flanged network; (b) Network. 19
2.2 (a) Total pressure; (b) Pressure directly from the source and reflected by the flange; (c) Pressure radiating from the network 20
2.3 A straight pipe at the center of a cylinder 21
2.4 Junction 28
2.5 Pressure at the imaginary end of a straight pipe: (a) $200-2000Hz$; (b) Around the resonant frequencies 31
2.6 Pressure at receiver R: (a) $200-2000Hz$; (b) Around the resonant frequencies 32
2.7 T pipe with rectangular flange 33
2.8 Pressure at the imaginary end ($z = 0.005m$): (a) $200-2000Hz$; (b) Around the second resonant frequencies 34
2.9 Pressure at point R near flange 34
2.10 (a) Network between a round surface and a rigid plane surface; (b) The network with open ends. 35
2.11 Pressure at point R outside the tire 35

2.12 Half of a tire with a network in the contact zone between a tire and a road . . . 36
2.13 (a) Network 1; (b) Network 2 . . . 37
2.14 Modulus of sound pressure at R: (a) $200 - 200HZ$; (b) Around the resonant frequencies . . . 37
2.15 Pressure modulus in a circle around the body (a) Frequency $200Hz$; (b) Frequency $1410Hz$; (c) Frequency $1455Hz$ . . . 38
2.16 (a) Meshes of half a cylinder with half of a straight pipe at the center of the contact zone; (b) Details of meshes of the contact zone. . . . 39
2.17 Predicted results for a straight pipe between a cylinder and a plane surface . . . 40
2.18 Predicted results for a network between a cylinder and a plane surface: (a) $200 - 2000HZ$; (b) Around the resonant frequencies . . . 40

3.1 Mesh of the boundary element model of a tube with a circular flange (case r/R =1/2) . . . 45
3.2 (a) End corrections divided by pipe radius from [3] (ka<2): (dots) fit formula (3.3) results, (plus sign) BEM results by Dalmont, (straight line) experimental results; (b) Errors between fit formula and BEM results (ka<0.23). (Symbol a in the figures represents the radius r) . . 46
3.3 (a) Half of meshes of the boundary element model of a rectangular tube with a flange of cylinder; (b) Details of the mesh of the tube. . . . 47
3.4 End corrections of longitudinal pipes with cylindrical flanges of different widths within $2000Hz$ ($ka < 0.23$) . . . 48
3.5 Standard deviations and mean values of end corrections of longitudinal pipes with cylindrical flanges of different widths . . . 48
3.6 (a) Half of meshes of the boundary element model of a rectangular tube with a part of tire flange; (b) Details of the mesh of the tube. . . . 49
3.7 End corrections of a longitudinal pipe with tire flanges of different widths within $2000Hz$ . . . 50
3.8 Standard deviations and mean values of end corrections of a longitudinal pipe with tire flanges of different widths . . . 50
3.9 T-shaped pipe . . . 52
3.10 Flow chart of Matlab program 2DNRF for calculating network resonant frequencies . . . 55

3.11 Modes of T pipe within 2000 Hz obtained from Abaqus by 2DNRF: (a) The first resonant frequency 912Hz; (b) The second resonant frequency 1605Hz. 57
3.12 Total pressure modulus at the open end of branch 3 58
3.13 Total pressure modulus distributions on the T pipe surface at resonant frequencies within 2000Hz by BEM: (a) The first resonant frequency 914Hz; (b) The second resonant frequency 1610Hz. 58
3.14 Modes of half network within 2000 Hz: (a) The first resonant frequency 1232Hz; (b) The second resonant frequency 1823Hz. 60
3.15 Total pressure modulus at the open end 2 61
3.16 Modes of half network within 2000 Hz obtained from Abaqus by 2DNRF: (a) The first resonant frequency 1224Hz; (b) The second resonant frequency 1770Hz. 62
3.17 Total pressure modulus at the open end 2 63
3.18 Total pressure modulus distributions of a half network at resonant frequencies within 2000 Hz by BFEM: (a) The first resonant frequency 1213Hz; (b) The second resonant frequency 1771Hz. 63

4.1 (a) T junction with left branch; (b) T junction with right branch; (c) Cross junction 65
4.2 An example of network for the chromosome representation 67
4.3 (a) Stochastic sampling with replacement (SSR) with one pointer; (b) Stochastic universal sampling (SUS) with ten pointers. 69
4.4 Single-point crossover 70
4.5 Multi-point mutation of an integer individual 70
4.6 Flow chart of GA process 71
4.7 An example of the networks generated randomly in the first generation of GA procedure 73
4.8 (a) Network with the resonant frequency 1254Hz; (b) Network with the resonant frequency 1400Hz; (c) Network with the resonant frequency 1590Hz. 74
4.9 (a) Mode of acoustic pressure at 1254Hz; (b) Mode of acoustic pressure at 1400Hz; (c) Mode of acoustic pressure at 1590Hz 75
4.10 The minimum difference between the targeted frequency 1400Hz and the resonant frequencies of individuals in each generation in GA procedure 76
4.11 (a) Network 1; (b) Network 2; (c) Network 3; (d) Network 4 77
4.12 (a) Network 1; (b) Network 2. 79

4.13 The maximum number of resonant frequencies for each generation in GA procedure 79

5.1 Sketch of experimental setup 82
5.2 (a) The experimental set-up; (b) flange used in calculations and experiments 82
5.3 (a) Generator and amplifier; (b) B&K pulse data acquisition system . 82
5.4 (a) A cylinder on a plane surface (no pipe between the cylinder and the plane surface); (b) A rigid plane surface between a source and an image source. 84
5.5 (a) Predicted results; (b) Measured results. 84
5.6 A straight pipe between a cylinder and a plane surface 85
5.7 Measured results of flange with a straight pipe 85
5.8 A network between a cylinder and a plane surface 86
5.9 Measured results of flange with a network 86
5.10 A optimized network between a cylinder and a plane surface 87
5.11 (a) Predicted results of a optimized network between a cylinder and a plane surface; (b) Measured results of a optimized network between a cylinder and a plane surface. 87
5.12 Optimized wooden network with the resonant frequency $1400Hz$ . . . 88
5.13 Measured SPL for the optimized wooden network with the resonant frequency $1400Hz$ 88
5.14 (a) Tire with an open network; (b) Tire with a closed network. 89
5.15 (a) The load of five concrete cylinders; (b) The contact zone between the tire and the road. 90
5.16 (a) The tire on the flour; (b) The contact area given by the flour. . . . 90
5.17 The tire with and without the lumps of flour 91
5.18 (a) The simplified network; (b) The meshes of the BEM model of the tire used in the multi-domain coupling methods. 91
5.19 (a) Measured results of the network between a tire and a plane surface; (b) Predicted results of the network between a tire and a plane surface. 91
5.20 Modes of the network obtained from Abaqus by 2DNRF: (a) The first resonant frequency $868Hz$; (b) The second resonant frequency $1734Hz$. 92
5.21 (a) The tire footprint in the contact zone; (b) The measured sound pressure level for a tire with the open or closed treads in the contact zone. 93

6.1 Optimization process of tire treads and road textures 98

6.2 (a) Point source and velocity excitation; (b) A simple network between the tire and the road. 98
6.3 Modulus of pressure at R under different excitations (a) Point source excitation; (b) Velocity excitation on the tire. 99
6.4 Pressure modulus at R $(1, 0, 0.265)$ for different source positions: $S1$ $(0.1, 0, 0.005)$ and $S2$ $(0.1, 0.0325, 0.005)$ 99
6.5 Networks (including end corrections) in the contact zone with targeted resonant frequencies (The vertical direction is the rolling direction): (a) $1400Hz$; (b) $1400Hz$ and $1250Hz$; (c) $1400Hz$, $1250Hz$ and $1050Hz$ (There are five closed ends in the middle of the contact zone). SPL at R for a tire with networks in the contact zone: (d) One network targeting $1400Hz$; (e) Two networks targeting $1400Hz$ and $1250Hz$; (f) Three networks targeting $1400Hz$, $1250Hz$ and $1050Hz$. 100
6.6 Periodic networks (including end corrections) with 4 resonant frequencies (The vertical direction is the rolling direction): (a) Network 1; (b) Network 2; (c) Network 3. SPL at R for periodic networks with 4 resonant frequencies: (d) Network 1; (e) Network 2; (f) Network 3. . . 103
6.7 SPL at R $(1, 0, 0.265)$ for the network 2 with different cross-sections . 105
6.8 The road tiles texture 105
6.9 (a) Half of meshes of the boundary element model of a longitudinal tube between a smooth tire and a road; (b) Details of the mesh of the model. 106
6.10 (a) Half of meshes of the boundary element model of a transverse tube between a smooth tire and a road; (b) Details of the mesh of the model. 106
6.11 (a) End corrections of longitudinal pipes under tires of different widths within $2000Hz$; (b) Standard deviations and mean values of end corrections of longitudinal pipes under tires of different widths. 107
6.12 End corrections of the transverse pipe in the middle of the contact zone under the tire within $2000Hz$. 108
6.13 Road texture in the contact zone 109
6.14 (a) Meshes of half the boundary element model of a longitudinal pipe at the center of the contact zone between a smooth tire and a road; (b) Details of the meshes of the model. 110
6.15 Road dimensions 111
6.16 Meshes of half the boundary element model of the texture with 2 columns and 3 rows under the smooth tire 111
6.17 SPL at R $(1, 0, 0.265)m$ for the network with 2 columns and 3 rows . . 112

List of Tables

2.1 Differences of SPL in Fig.2.18a between the case without network and the case with one network around resonant frequencies 41

3.1 The resonant frequencies of flanged T pipe 59
3.2 The resonant frequencies of a network with cylindrical flange 61
3.3 The resonant frequencies of a network with tire flange 62

4.1 Coordinates of central points of open ends of a unflanged network . . 73
4.2 Results for the targeted resonant frequencies 74
4.3 Networks with three resonant frequencies 77
4.4 Coordinates of central points of open ends of network between a cylinder and a plane surface 78
4.5 Networks with four resonant frequencies 79

5.1 Predicted and measured results 85

6.1 Four resonant frequencies for the three optimized networks 102
6.2 SPL reductions at the resonant frequencies of the three optimized networks 104
6.3 The number of resonant frequencies of networks with different number of columns and rows 109
6.4 The resonant frequencies of networks with 2 columns and $3-5$ rows . 109
6.5 The modulus of the sound pressure at the receiver for different dimensions of the road 110

Chapter 1

Introduction

The tire/road system can be seen as a horn-like structure. The surfaces of the tire and the road constitute horns in front of and behind the contact zone. The noise generated in the contact zone is amplified by the horn-like structures. Tire treads and road textures in the contact zone between the tire and the road can be considered as acoustic network resonators. The acoustic fields around the tire/road system are also influenced by the network resonances. In this chapter, first the importance and the mechanisms of the tire/road noise are presented. Then studies and applications of the acoustic resonators are reviewed. Next boundary element methods used for calculating the acoustic fields of the horn-like structure are introduced. Last optimization methods are compared in order to choose a suitable one for the optimization of tire treads and road textures.

1.1 Tire/road noise

The road traffic noise is a part of the community noise which also includes other traffic, industries, construction, public work and so on [5]. Among these noise sources, the road traffic noise is a dominant source [6]. About 40% of the Europeans are exposed to levels of the road traffic noise exceeding $55dBA$ daytime, and 20% are exposed to levels exceeding $65dBA$ according to the study [7] by Lambert in 1994. Nowadays this problem is even worse due to the population growth, urbanization and the enlargements of the highway systems.

The traffic noise is very annoying and has many adverse health effects. It can cause population annoyance, interference with communication and intended activities, disturbance of sleep, hearing impairment and so on. It also has large economic effects. From the EU Green Paper of 1996 we know that the cost of traffic noise in 17 European

countries is about 0.65% of GDP.

The traffic noise emitted to the environment includes the tire/road noise, power-train noise and the aerodynamic noise. The contribution of the tire/road noise is the largest [1]. Tire/road noise is the loudest component in the total noise level of cars traveling faster than 50 km/h and trucks traveling faster than 80 km/h [8].

1.1.1 Mechanisms

The tire/road noise is generated between the tire and road, and then radiates from the horn-like structure formed by the tire and road. In [4] the mechanisms that create the energy of the noise are referred as sound generation mechanisms, and the mechanisms that convert the energy to noise and radiate it are referred as sound enhancement mechanisms. These mechanisms are shown in Fig.1.1.

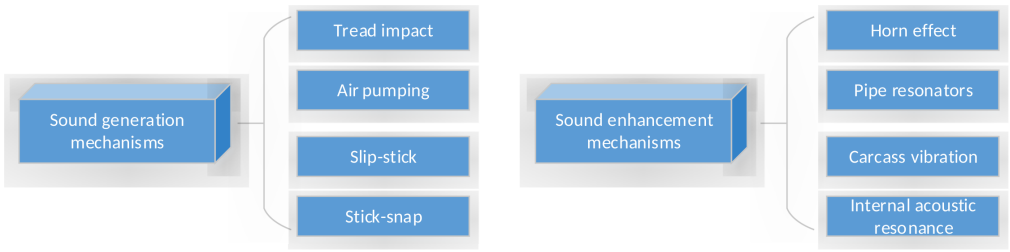

Figure 1.1: Sound generation and enhancement mechanisms of tire/road noise [4]

The sound generation mechanisms are tread impact, air pumping, slip-stick and stick-snap. The tire treads keep hitting the road at the entrance of the contact interface when the tire is rolling. The impacts of small rubbers on the road result in vibrations of the tire. In the contact zone between the rolling tire and road, the grooves on the tire surface are compressed and then recover, so air is pumped in and out. The noise is generated by the pumping effect. The treads will slip briefly if the horizontal forces from the road exceed the limits of friction, and then stick to the road during acceleration, braking or cornering. Both noise and vibration will be generated by the repeated slipping and sticking. When the tire treads leaves the contact zone, the release of the adhesion between the tire and road will generate noise and vibration.

The sound enhancement mechanisms includes horn effect, pipe resonances, carcass vibration and cavity resonance. The tire surface and the road create horn-like structure both in front of the tire and behind the tire. The noise generated in the contact patch is enhanced by the horn. The pipes between the tire and road in the contact resonate at the resonant frequencies. The carcass vibration is generated by the energy created in the contact patch. Noise is radiated from the tire carcass. The air in the

cavity inside the tire resonate.

A prominent peak in the range of $700 - 1300Hz$ can be found in most frequency spectra of the exterior tire/road noise. In [9] this peak is investigated. The causes include characteristics such as tread pattern pitch, pipe resonances, tangential block resonances, belt resonances, the horn effect and road texture geometry. The author even inferred that the developments in tire design, dictated by other concerns than exterior noise, had tended to increase this problem.

In [10] the influence of the pavement characteristics on the generation and propagation of the tire road noise is studied. The tire road noise can be reduced by the road absorption effect. A numerical correspondence is found between the acoustic absorption coefficient in normal incidence and the difference of the pass by noise level between the absorbing and the reflecting surfaces in [10].

1.1.2 Tire vibration and air pumping

The mechanisms of tire vibration and air pumping are the tasks of this work, so we only give a short review in this subsection.

This mechanism is studied in many publications [11–17]. In [11] tire/road interaction and radial tire vibrations are studied by the measurement of a rolling smooth tire for tire/road noise characterisation. This study gave a physical insight on generation mechanisms of tire radial vibrations. Larsson [12] proposed a double-layer tire model in order to take into account the tangential motion and the local deformation of the tread. The model was validated by comparing the calculations and measurements of the response of a smooth tire under an external excitation. In [18] the measured road profiles are used as input data in INRETS rolling tire model to estimate the tire/road noise. The tire/road noise due to the tire vibration is within about $1kHz$. Nackenhorst [13] studied the arbitrary Lagrangian Eulerian formulation of rolling, and developed the weak form of the equations of motion. Tatsuo Fujikawa [14] defined the essential road roughness parameters that govern tire tread vibration and provide information on tire/road noise reduction. He used a tire/road contact model to estimate the effects of road roughness parameters on tire tread vibration. The conclusion is that the pavement asperity height itself is not an important parameter. However, asperity height unevenness, asperity radius, and asperity spacing are essential for the reduction of tire vibration noise. Kozhevnikov [15] calculated the spectrum of natural frequencies and natural forms of vibration for a free and a loaded tire using the model of a wheel with a reinforced tire in order to estimate the level of noise of a tire moving on an uneven surface. Rustighi [16] presented a simple model for the prediction of tire behavior in the frequency range up to $400Hz$. A linear model was used to calculate

the contact forces and the average spectral properties of the resulting radial velocity. Kim [17] used a circular ring model in a low frequency range and a cylindrical shell model above $300Hz$ to investigate the wave propagation of a tire. He found that one of the most important features in sound radiation of a tire shell is acoustically excited wave motions of the tire wall.

Today the noise due to the vibrations of a rolling tire can be calculated with convincing accuracy. However, air pumping is not understood very well. In [19] Hayden described the air movement in the contact zone between a rolling tire and a road. Air is squeezed out when the treads at the entrance of the contact zone are compressed on the road surface, and flows into the voids when the treads lift up from the road surface. Daffayet et al. [20] measured the pressure in cylindrical cavities over which a smooth tire rolled. They assumed that the noise generated by opening and closing the cavities in the contact zone. Ronneberger [21] thought that air was displaced by the changing gaps between the tire and road surfaces, because the treads are deformed by road roughness.

1.1.3 Horn effects

Horn effect in Fig.1.2 is an essential noise enhancement mechanism. The tire/road system can be seen as a horn-like structure. The surfaces of the tire and the road constitute horns in front of and behind the contact zone. The noise generated in the contact zone is amplified by the multiple reflections between the tire surface and the road surface which are acoustically reflecting surfaces. The amplification of the horn effect reaches up to 10 to $20dB$ in the results of previous studies, where the road and the tire are modeled with smooth surfaces. The amplification can be calculated by equation (1.1), where P is obtained in Fig.1.3a and P_{ref} is calculated in Fig.1.3b. In the calculations of P and P_{ref}, a source is located in the horn between the tire and the road.

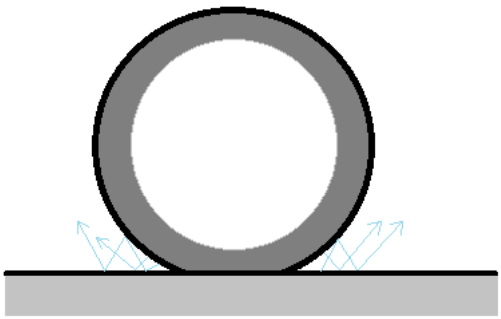

Figure 1.2: Horn effect: multiple refections of sound in the horn-like structure

In this work, we try to optimize the tire treads and road textures in order to reduce the amplification of horn effect. P is still calculated in the case where a tire is on the road, and P_{ref} is still obtained in the case where no road is under the tire. In the latter case, whether the tire is smooth or has treads P_{ref} is almost the same. Therefore, in the following calculations we only investigate the influences of the networks between the tire and the road on the acoustic pressure P.

$$A = 20log(\frac{P}{P_{ref}}) \tag{1.1}$$

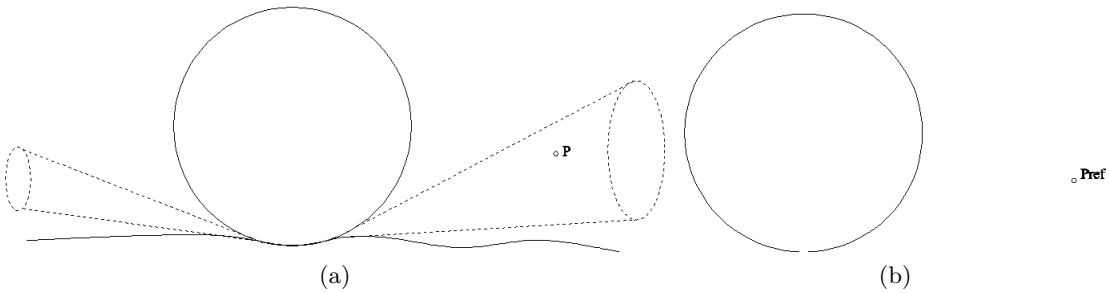

Figure 1.3: (a) Tire on the road; (b) Tire without the road.

A first attempt at an analytical description of the horn effect was made by Ronneberger [22]. He represented the tire geometry as a flat rigid surface extending to infinity at a small angle to the road, forming a wedge-shaped horn. Contributions from a single source and its images then sum to produce a far-field acoustic pressure spectrum which exhibits a characteristic, lobed interference pattern. The finite width of the tire is accounted for by superimposing a low-frequency dependence derived from the spectrum of a decaying sine wave. Although this model describes the general shape of the amplification spectrum, it does not fully resolve the low frequency behavior, nor does it predict the correct lobe structure for high frequencies. It therefore seems necessary to describe the tire geometry more accurately.

Kropp et al. [23] suggested a theoretical model based on multipole synthesis. The model can provide a reasonable prediction of noise levels at mid and high frequencies for a tire placed on a hard surface. However, it overestimates the horn amplification effect at low frequencies. Since the Kropp model is a two-dimensional one, the model can only be valid for estimating the amplification of sound when the receiver is located in the plane of a tire.

Graf et al. [24, 25] first investigated experimentally the horn amplification of sound generated by a simple acoustic source. The boundary element method is then shown to give predictions. And the dependence of the horn-effect on different geomet-

rical parameters is also investigated both through experiment and boundary element calculations. It shows that for the intermediate frequency range the BEM provides an excellent tool to calculate the horn effect for practical geometries. However, the computations are expensive, limited to frequencies below 2500 Hz, and provide little physical insight. So two supplementary asymptotic approaches are developed in Kuo et al. [26]: a ray theory for high frequencies and a compact body scattering model for low frequencies. These methods are found to have good predictive capabilities, at frequencies above 3 kHz and below 300 Hz respectively. Ray theory provides a useful physical basis for the interpretation of the lobed interference patterns seen at these frequencies. The main strength of the low frequency theory is the insight it yields into the parametric dependence of the amplification.

The aim of the work by Anfosso et al. [27, 28] is also to predict the amplification due to horn effect. Sound pressure amplification of a 2D infinite rigid cylinder is obtained using the analytical approach based on modal decomposition of sound pressure. It gives quick and accurate results, but is limited to simple geometrical configurations and purely reflecting properties of boundaries. Horn effect is reduced for porous road surface because of sound absorption properties. To introduce sound absorption of the road surface, 2D Boundary Element Method was used to describe the porous pavement by a phenomenological model. The parameters of the mesh are optimized by comparison with the results from the analytical model. The BEM models are more time consuming but more realistic situations can be predicted. Then the analysis was extended to a 3D rigid sphere.

In [29] Fadavi et al deal with the horn effect using a 3D cylinder tire model. The sound pressure and sound amplification are calculated in the space around the 3D tire model using the Boundary Element Method. The influence of different parameters such as the position and size of the source are studied in terms of amplification and sound pressure spectrums.

Wai keung lui et al. [30] offered a simplified theoretical model to carry out a parametric study when selecting appropriate materials for porous road pavement. A study of the influence of porous ground on the horn effect is discussed considering the parameters such as the thickness of the porous layer, double layer, porosity, and the variations in the angular position of the source.

1.2 Acoustic resonators

Tire treads and road textures in the contact zone between the tire and the road can be considered as acoustic network resonators. The acoustic fields around the tire/road

system are influenced by the network resonances. The resonances of the pipes in the contact zone between the tire and the road in Fig.1.4 are seen as one of the noise enhancement mechanisms in [4]. However, this conclusion may be not correct if the pipe resonances are investigated together with horn effects, because the horns between the tire/road system and the pipes in the contact zone constitute the boundary of the acoustic fields together. In fact, the sound fields can be reduced around the resonant frequencies. Since the network resonators in the contact zone have large influences on the acoustic field around their resonant frequencies, the acoustic behaviors inside the networks and the resonant frequencies should be investigated in detail. First the studies of some simple acoustic resonators are reviewed in the following sections.

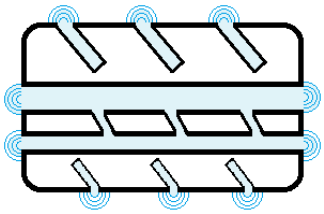

Figure 1.4: Pipe resonators in the contact zone between a tire and a road

1.2.1 Straight tube resonator

The straight tube resonators are applied to many acoustic problems, such as sound absorption, radiation and transmission, in the previous studies. The straight tube with one open and one closed end or two open ends are first used. Then two straight tubes are coupled to improve the performance.

1.2.1.1 Sound absorption

For the sound absorption, there are several ways. Porous materials show a broadband sound absorbing behaviour above a certain frequency and the acoustic energy is converted to heat because of the viscosity inside the materials. Perforated panel, which can be seen as a row of Helmholtz resonators, can be used for the absorption of a small band of low and medium frequency sound.

Besides porous materials and perforated panels, narrow quarter-wave tube resonators are also widely used for the sound absorption in a wall (see Fig.1.5) or panel for a narrow frequency band based on the resonance of air inside the tube and the viscous shear and thermal conductivity losses on the tube walls. The model by Zwikker and kosten [31] for wave propagation in cylindrical tubes included the viscosity and thermal conductivity. Tijdeman [32] proved that this model is complete and accurate

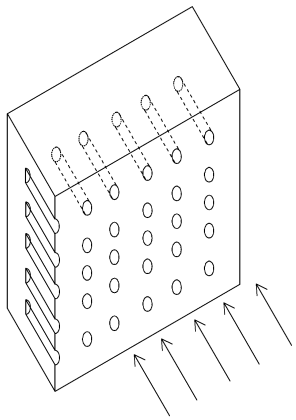

Figure 1.5: A sound absorbing wall with quarter-wave resonators.

for both narrow and wide tubes. Eerden [33] studied the influence of the viscous and thermal conductivity losses on the absorption coefficient and concluded that the viscothermal effects cannot be neglected if the resonators are used for sound absorption because they result in energy being dissipated and the effective speed of sound inside the tube can be considerable reduced. Around the resonant frequencies, we can see a maximum sound absorption. For the wall or panel with the tube resonators, the tube radius and the porosity (the ratio of the sum of the tube cross-sections and the panel area) determine the height and the width of the absorption peaks. The theory and applications of quarter-wave resonators are summarized in [34]. The attenuation of fan noise by the quarter-wave resonators can be found in many researches [35–38]. The combination of noise barrier and the quarter-wave resonators can be seen in [39–41]. Studies [42–44] applied the quarter wave resonators to the attenuation of noise entering buildings through ventilation openings.

The quarter-wave tube has an open and a closed end, but resonators with two open ends can also be used for the sound absorption, especially for the case where air needs to be transported through wall or one needs to see through the wall. Eerden also studied this case, and concluded that at low frequencies ($f < 2000Hz$) the waves propagating in the resonator are not absorbed at the end but are reflected back into the resonator due to the mass reactance at the free end. For higher frequencies ($2000-10000Hz$) the waves are absorbed due to radiation into infinity.

In order to create broadband sound absorption, coupled tube resonators with different cross-sectional areas and lengths in Fig.1.6 are designed and applied by Eerden. The mechanism for the broadband absorption is that the sound energy is dissipated by the viscothermal effects and the incident waves are cancelled due to the broadband resonance of air in the coupled resonators. Experiments for the quarter-wave tubes

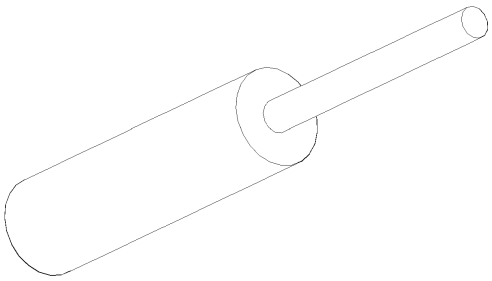

Figure 1.6: Two axially coupled tubes.

with different porosities and lengths, tube resonator with two open ends and different coupled tubes are performed by Eerden to validate the methods and design tools. Eerden [33] used a simple and efficient network of small couple tubes to predict the acoustic behaviour of conventional sound absorbing materials, for example glass wool and foams. The sound absorption of the one-dimensional case agrees well with the empirical and theoretical models.

1.2.1.2 Sound radiation and transmission

The tube resonators can also be applied for the reduction of sound radiation of a panel based on the resonance of the air inside the tube. The viscothermal effects are much less important in this case. On a small partition of the panel, no sound will be radiated if the velocities at the panel surface and at the tube end are equal but opposite in phase. By tuning the length, the radius and the porosity of the panel, different sound reducing properties can be obtained. Weak radiating cells are used for passive noise reduction based on a similar principle by Ross and Burdisso [45].

Parallel resonators of the straight tubes are applied for the reduction of sound radiation from and transmission through the rigid or flexible panels in [46]. Analytical with viscothermal effects and numerical models are proposed to predict the influences of the panels with the parallel tube resonators. For the sound radiation, good agreements between the calculations and measurements can be seen. But the models need to be developed because the predictions of the increases of the sound transmission loss by the application of tube resonators are larger than the measured results.

1.2.2 Helmholtz resonator

Helmholtz resonator can be considered as a mass-spring system. The spring stiffness is represented by the volume of air and the mass is given by the small column of vibrating air in a perforation of the panel. The energy can be dissipated by the vi-

brating air and the porous material placed in the volume. The Helmholtz resonators (HRs) are used to control the noise inside the enclosure in many studies [47–51]. In [47] the coupling between a single resonator and a single enclosure mode was taken into account, and damping materials were used inside the resonator to improve the dissipation and broaden the working bandwidth. In the study of damped HR [48] the optimal resonator resistance can be seen in the experiments. Then the model in [47] was further developed by Cummings [49] so that multiple resonators and multiple modes of the enclosure can be taken into account. In [50] two serially connected chambers are used to compose a resonator in order to deal with two enclosure resonances at the same time. Similarly, one resonator with multiple serially connected chambers were used to target multiple enclosure modes in [51].

1.2.3 T-pipe resonator

T-shaped acoustic resonators in Fig.1.7 can be seen in many researches for noise control in small enclosures. Merkli [52] first proposed a theoretical model for the calculations of the resonant frequencies of a T-shaped tube. Then Li and Vipperman [53, 54] use a multi-mode model for the design of the T-shaped acoustic resonators in order to control noise in the enclosures. T-shaped acoustic resonators are also used in [55] to reduce the resonances of an enclosure based on the wave cancelation around the resonant frequencies. The acoustic interaction between the enclosure and the resonators are studied and design tools for optimizing the resonators are developed. Then experiments are done to validate them. The model and design tools are applied to the noise transmission control through a double-glazed window by using the T-shaped acoustic resonators. Besides, in the expendable launch vehicle payload fairing [56] and the chamber core fairing [57] there are applications of the T-shaped acoustic resonators.

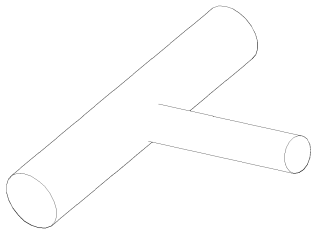

Figure 1.7: T-shaped acoustic resonator.

1.3 Acoustic radiation of baffled piston

In this thesis, the horn effect and the pipe resonances will be investigated in the same model. In this model, the surfaces of the tire and the road can be seen as flanges, and air at the ends of the pipes between the tire and the road can be considered as pistons on these flanges. If there are incident waves on the pistons, the acoustic fields inside the pipes will be excited and there will be waves radiating from the pistons to the exterior domain. So the computational methods of the acoustic radiation of the baffled pistons should be developed. For the acoustic radiation of a piston with an infinite flange in Fig.1.8, we have analytical solutions. But the surfaces of the tire and the road are very complex, numerical methods should be used. Since boundary element methods are suitable for the complex surfaces, we will propose a multi-domain coupling method in chapter 2 based on BEM to solve the problem. There is a brief review of BEM in the following.

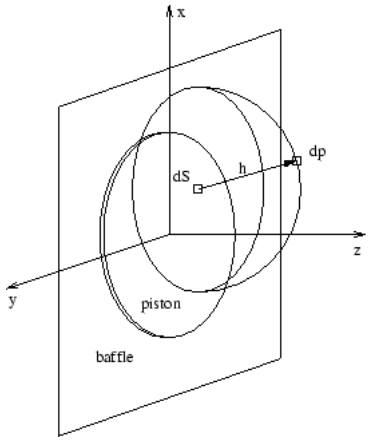

Figure 1.8: A piston with an infinite baffle.

1.3.1 Boundary element methods

The numerical solutions (using boundary elements) of the direct BIE (boundary integral equations) formulations are first applied to 2D potential problem in [58]. Then they are extended to 2D elastostatic problem in [59]. One of the most important applications of the BEM is solving acoustic problems and predicting acoustic fields for noise control. We can find many researches on the development of the BEM for solving the exterior acoustic problem. The work in [60] is considered as classical work and the BIE formulation in [60] is used by many researchers for solving acoustic problems. More researches on the boundary element methods (BEM) are reviewed by Liu [61].

The BEM only requires discretization of the boundary of the domain. Boundary meshing is simple when modeling many problems with complicated geometries. However due to the dense and non-symmetric matrices produced by the conventional BEM, for large-scale problems its efficiency in solutions is a big problem.

1.3.2 Fast multipole boundary element methods

Thanks to the acceleration of the fast multipole method (FMM), the BEM can solve large-scale problems. The fast multipole method stemmed from the computation of the potential field of interactive discretized multi-particles system. For all particles, the computation complexity is $O(N^2)$. In 1986, Barnes and Hut published a paper in Nature proposing the Tree Codes. It uses the tree structure and reduces the computation of mutli-particles system to O(NlogN) by recursive operation [62]. The prototype of FMM was first proposed by Rokhlin when calculating the boundary value problem of ellipse and introduced the concepts of multipole expansion and local expansion [63]. In 1987, Rokhlin and Greengard formally proposed the fast multipole method and combined the tree structure with the multipole and local expansion. It reduces the computation complexity of multi-particles systems to O(N) [64]. However, when the particles are unevenly distributed, the former tree structure will lead to the reduction of computation efficiency. So in 1988, Carrier et al. introduced the adaptive tree structure which generates according to the distribution of the particles [65]. In order to further improve the computation efficiency of FMM, Rokhlin introduced the concept of diagonalization in 1993 [66]. And in 1997, Greengard and Rokhlin [67] proposed the new version of FMM which greatly improved the computation efficiency of FMM by introducing the new exponent expansion.

The discretized multi-particles system are similar to the continuous medium. Suppose that the particles are continuously distributed on the space curved surface, the discretized multi-particles system can be transformed to continuous distribution system. After discretizing the curved surface into surface elements, every surface element can be regarded as a particle. So the curved surface is equivalent to the discretized multi-particle systems and FMM can be used to accelerate the computation of the integral on the curved surface. Therefore, FMM can also be used to accelerate the boundary integral which includes the kernel function and boundary variable in the boundary integral equation.

In the BEM system of equations, each equation represents the sum of the integrals on all the elements when the source point is placed at one node. The conventional approach is still used to evaluate the integrals on the elements that are close to the source point. The FMM is applied to evaluate the integrals on the elements that

are far away from the source point. The advantages of fast multipole BEM can be described as follows:
1. When solving the BEM system of linear equations using an iteration method, the multiplication operator of the coefficient matrix and iterative vector should be done at least once for every iteration. But with FMM, for every iterative operator of BEM, use the tree structure to describe the multiplication of coefficient matrix and iterative vector, so the coefficient matrix needn't be stored using an array.
2. The multiplication result of the coefficient matrix and iterative vector can be got by the recursive operator of the tree structure, and the accuracy can be controlled.
3. Both the computation and storage of the tree structure are O(N), so on the premise that the iterations converges rapidly, the relationship between the degrees of freedom and the computation and storage of the fast multipole BEM is linear.

With the help of the FMM, the BEM is unmatched by other methods for solving large-scale acoustic problems. Researches on solving the Helmholtz equation by the fast multipole BEM are reviewed in [61].

1.4 Optimization methods

For the acoustic resonators, the resonant frequencies are very important because their working frequency bands are around the resonant frequencies. In order to get two dimensional networks with wanted resonant frequencies, we need to know what parameters of the networks govern their resonant frequencies. The networks in Fig.1.9 that we investigate have perpendicular rows and columns. The parameters of the network structure include junction type, end type, cross sectional area and positions of the junctions and the ends. These parameters should be optimized with the optimization methods to get the wanted resonant frequencies. A program based on the optimization methods is developed for this purpose.

The objective function of our optimization problem is quite clear. We want to get the networks with the targeted or maximum number of resonant frequencies within a specified frequency range. So for the targeted resonant frequency, we can calculate the difference between the obtained resonant frequency and the resonant frequency. The network with the minimum frequency difference will be chosen. For the maximum number of resonant frequencies, we can count the resonant frequencies of the obtained networks. Then we add a minus sign to the number in order to get a minimization problem. The ones with the smallest number will be selected.

The goal of our optimization is to minimize the objective functions by modifying the parameters of the network junctions. But the parameters cannot take arbitrary

Figure 1.9: A simple example of a two dimensional wooden network with open and closed ends

values. They should stay within a range of feasible values which is defined as the search space. The search space determine which type of optimization method should be used. Each parameter can vary continuously or take only a set of discrete values.

For the case where all the parameters vary continuously, we can introduce the derivative or sensitivity which quantifies how much the objective function are changed as the parameters are varied. Only a local solution can be found by this kind of approach. Because only a neighborhood of the initial guess is searched. However, the solution can be improved by using several randomly chosen starting points. This kind of method is used in [68] for the optimization of tramway low height noise barriers and in [55] for the optimization of T-resonator location in an enclosure. However, some of the network parameters take discrete values. For instance the junction type varies in several specified junctions. In this case, we cannot define the derivative, and therefore we should use a different approach. Evolutionary optimization methods are well-suited for this purpose, for example genetic algorithms. Since they do not necessarily require a discrete search space, other network parameters, such as the cross sectional area and the position of a junction, can vary in continuous ranges. These methods allow a more global search. Therefore, genetic algorithms will be used in our optimization of network structures for the wanted resonant frequencies.

Besides, the simulated annealing method is also a global search method. Similar as genetic algorithms, it does not require the derivative information of the physical problem. It can be applied to discrete and continuous problems. It is inspired from the physical process of the cooling of a metal. Initially the metal is under the disordered state at a high temperature. If the annealing time is long enough, the thermal equilibrium can be reached at each cooling stage, which warrants the minimum energy level. Eventually, the metal becomes a crystalline structure. In the simulated annealing

method, the process starts at a high temperature. In order to find the minimum value of the objective function at each subsequent temperature, sufficient iterative searches are carried out. The temperature keeps decreasing until the process is terminated, so the optimal solution can be obtained.

For the calculation of our objective functions, the resonant frequencies should be estimated. There are analytical methods for the estimations of the simple straight and T-shaped resonators. However, the networks to be treated in this work are more complex. It is difficult to give accurate estimations of the resonant frequencies analytically. Therefore, numerical methods (finite element methods) will be proposed.

1.5 Objective and Scope of Research

This work is conducted within the framework of the German-French DEUFRAKO project **ODSurf** concerning the reduction of the rolling noise of the road traffic by optimizing the road surfaces. Researchers in this project focus on the improvement of the theoretical models (air pumping, tire/road contact, horn effect and pipe resonance), the validation of new measurement systems including the 3D texture analyser and the industrial realizations of optimized low noise dense road pavement. After testing the models on all the low noise surfaces and comparing these surfaces, the acoustic characteristics of these surfaces will be used to complement and extend the capabilities of the common database DEUFRABASE.

The topic of this study is about the two mechanisms of the tire/road noise: pipe resonance and horn effect. Although a lot of researches have been done in order to reduce the tire/road noise, some mechanisms of the tire/road noise should be taken into account together. In this thesis, the pipe resonances and the horn effect of the tire/road noise will be calculated in the same model. In the previous studies of the horn effect, the tire and the road are modeled with smooth surfaces. In this work we try to use the resonances of the networks formed by the tire treads and the road textures in the contact zone to reduce the amplification of the horn effect around the resonant frequencies. The acoustic resonators are widely used for the noise control. The original peaks of sound pressures can be reduced by inserting the acoustic resonators.

For simple T-shaped pipes, the resonant frequencies can be estimated analytically. But for the networks their structures are too complex to be estimated by the analytical methods. So numerical methods should be developed. In order to reduce the amplification of the horn effect at targeted frequencies, a design and optimization method of the network structures should be given to obtain the wanted resonant frequencies. Because the resonant frequencies of the networks depend on their structures.

A systematic study on the pipe resonances and the horn effect of the tire/road will be carried out in this thesis. Systematic analysis tools for the tire/road noise including the calculation of the acoustic fields, the estimation of the resonant frequencies and the optimization of the network structures are developed. The scope of this work is listed as follows:

(1) A model to characterize the interaction between the flanged networks and the exterior domain is proposed. The influence of the viscous and thermal conductivity losses is studied.

(2) The determination of the end corrections of the network inside arbitrary body is carried out. A numerical method for the estimation of the resonant frequencies of the network is developed.

(3) A design and optimization method based on the genetic algorithm for obtaining the network with the wanted resonant frequencies is proposed.

(4) Experiments of wooden cylinders, wooden networks and a real tire are carried out to validate the interaction model and the methods for the estimation of the resonant frequencies and the optimization of the network.

(5) The optimized tire treads and road textures are applied to reduce the amplification of the horn effect.

This chapter involves an overview of the tire/road noise and a review of the horn effect, the acoustic resonators and the boundary element methods. In chapter 2, a model for the flanged networks is proposed. For a simple structure, radiation impedance can be used to calculate the acoustic fields. For a complex flange, multi-domain coupling methods are developed. The viscous and thermal conductivity losses can be taken into account. Chapter 3 includes the numerical methods for estimating the end corrections and calculating the resonant frequencies. Boundary element methods and Finite element methods are used for the estimation of the end corrections and the calculation of the resonant frequencies, respectively. Chapter 4 focuses on the methods for designing and optimizing the network structures in order to obtain the wanted resonant frequencies. The genetic algorithm is adopted for this purpose. Measurements are performed in chapter 5 to validate the model and the methods proposed in the previous chapters. A Wooden cylinder and networks are built and measured as well as a real tire. Chapter 6 concerns the optimizations of the tire treads and road textures for the reductions of amplifications of the horn effect. Final conclusions and future works are presented in Chapter 7.

Chapter 2

Modelling of networks in horn-like structures

2.1 Introduction

Horn-like structures with networks inside can be considered as bodies with macro porosities, which can be seen in the analysis of porous walls, horn effects of road/tire and so on. It is essential to calculate the sound pressure field around them. Such problems include the acoustic transmission-radiation problems. The networks constituting the porosities could be networks, several parallel pipes or a mixture of them.

In such systems the networks to be analyzed have small cross sections. However, the cross sections are neither as small as the arbitrary microscopic holes in many porous materials nor as complicated as the pipes in the mufflers, so it is not suitable to use the same methods to calculate the sound pressure fields. Besides, in porous materials acoustic energy is dissipated as heat because of viscosity, so noise could be reduced by porous materials. But for the networks considered in this work the main mechanisms of noise reduction by networks are the pipe resonances. However, the methods for mufflers could give some inspirations.

Mufflers have complicated internal structures such as inlet/outlet tubes, thin baffles, perforated tubes, and sound absorbing materials. There are several methods for the analysis of mufflers summarized in [69]. The multi-domain boundary element method (BEM) and BEM with the transfer matrix could be used for the calculation of the flanged network, but some changes should be made.

A brief introduction of the applications of multi-domain BEM can be seen in [70]. It was first used to analyze the potential problem and elasticity [71]. Then it was introduced to solve acoustic problems. An important application of multi-

domain BEM to acoustics is the coupled interior/exterior problems [72] where the interior boundary integral equation is used for a finite internal domain and the exterior boundary integral equation is used for an infinite external domain. The solution at the interface between the two domains is coupled by the continuity constraint equations. So the problem can be solved as a continuous field problem to get a solution at any point in the whole domain. The multi-domain BEM is also used to deal with problems with several acoustic media [73]. Another wide application is the problem about thin bodies [74, 75] before using the hypersingular integral equation.

Transfer matrix techniques have been applied to the analysis of the series connection pipes with many changes of sectional area in [76]. The advantage is that only two-by-two matrices are needed and it is possible to work on a desktop computer, but only using the transfer matrix is not easily applied to network. In [77] a different form of transfer matrix is used, together with the matrices derived for the two-dimensional junctions by the finite element method, to describe a complete network. In [78] the transfer matrix is used to combine the impedance matrix of each substructure of a silencer.

The transfer matrix can easily connect two substructures and describe the relation of pressure and particle velocity between them. But an assumption should be true to get the transfer matrix, which is the plane wave propagation in the connected part.

For the network analyzed in this part, BEM of one computational domain is available, but only for very simple case, as BEM needs fine mesh around the resonant frequency of the air in the network to get converged solutions. Substructuring techniques can reduce the matrix size and the total computational time for complex structures. Dividing the whole acoustic domain into several subdomains is the main idea of the multi-domain coupling method. Each subdomain, which could be an exterior or an interior one, has a well-defined boundary and the same material property. The exterior boundary integral equation is used for the infinite external subdomain. For the interior subdomain, transfer matrix, 2D analytical relations, FEM or BEM can be used. The solutions at the interfaces between the subdomains are coupled by the continuity constraints of sound pressure and normal particle velocity.

First the structures to be analyzed and wave propagation are introduced. Then the computational methods are described in the next section. Next comparisons are made to check the accuracy of the proposed methods. Last viscous and thermal conduction losses are taken into account in the simulations to show their influences.

2.2 Problem specification

2.2.1 Flanged network

The structure to be analyzed here has arbitrary flange and macro porosities (see Fig.2.1a). The network constituting the porosities could have any connection pattern: arbitrary network like Fig.2.1b, parallel pipes or a mixture of them. The pipes here have small cross sections.

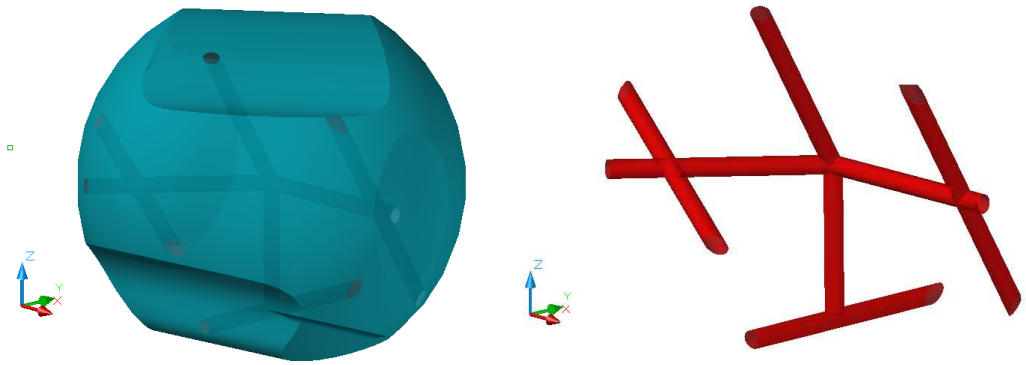

(a) (b)

Figure 2.1: (a) Flanged network; (b) Network.

2.2.2 Wave propagation

Fig.2.2a represents three dimensional networks with arbitrary flange. A point source S is put near the flange. The acoustic wave at point R includes three parts (see Fig.2.2a): a wave directly from the source, a wave reflected from the flanged without network (see Fig.2.2b) and a wave radiating from the network with flange (see Fig.2.2c).

The wave from the source arrives at pipes ends and then propagates in the network. The straight parts of the network are very thin compared with the wavelength to be analyzed. The working frequencies of the source are below the cut off frequencies of straight parts. So there is only a plane wave motion in the straight parts that consists of a forward travelling wave and a backward reflected wave. The waves in the junctions of the network have higher order modes, but they don't propagate in the straight parts.

In Fig.2.2b, imaginary pipe ends are used instead of the real ends. The imaginary ends are inside the network but close to the real ones. The imaginary surfaces S_{imag} are perpendicular to pipes walls. Thus, at S_{imag} the wave is uniform and the velocity is perpendicular to the imaginary end, which is useful in the method proposed in

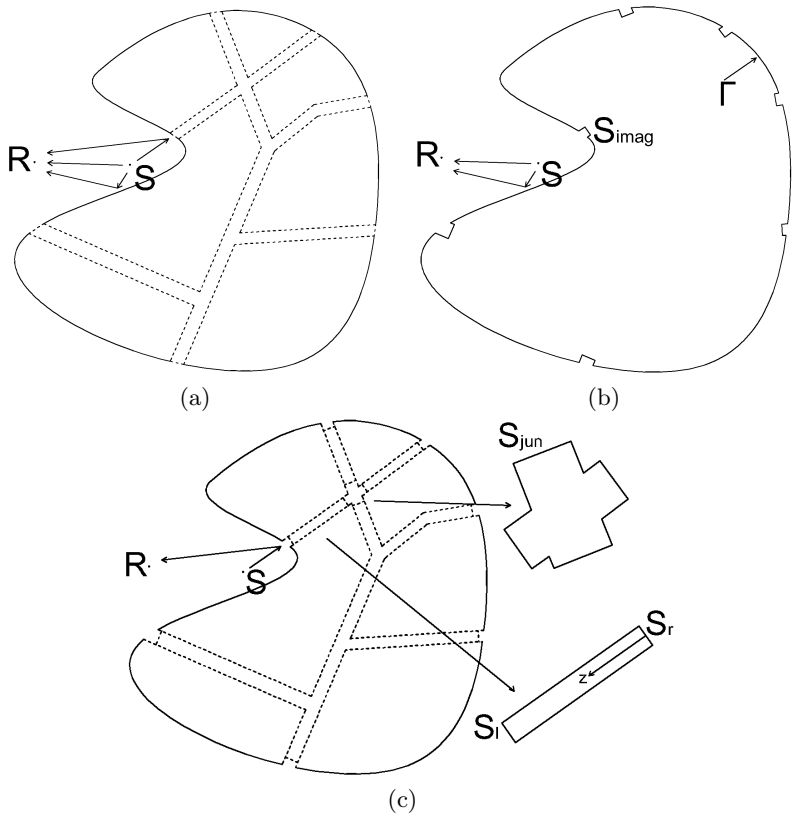

Figure 2.2: (a) Total pressure; (b) Pressure directly from the source and reflected by the flange; (c) Pressure radiating from the network

this chapter. However, it is not uniform at the real ends, even if the real ends are perpendicular to the network walls, because the cross sections change suddenly.

2.2.3 Boundary condition

The boundary conditions on the flange surfaces could be the pressure, the normal derivative of the pressure, the impedance, the surface velocity, or a mixture of them (see equation (2.1)). For network walls, boundary conditions are rigid.

$$\begin{cases} p = p_0 \quad (on \quad \Gamma_p) \\ p = Zv \quad (on \quad \Gamma_Z) \\ v = v_0 \quad (on \quad \Gamma_v) \end{cases} \tag{2.1}$$

Pressure p_0, impedance Z and velocity v_0 are known. We have $\Gamma_p \bigcup \Gamma_Z \bigcup \Gamma_v = \Gamma$.

2.3 Radiation impedance methods

For a simple flange and a straight pipe, we can get radiation impedances of open ends easily. So acoustic fields can be obtained by using the radiation impedances. An example is given to show the calculations. The simple flange in our example is a cylinder. There is a thin pipe at the center (see Fig.2.3). The flange and pipe wall are rigid. The radius of the pipe and the flange are $0.005m$ and $0.6m$ respectively. The pipe length is $0.1m$. The source S is at $(0, 0, -0.1)$. The total pressure at receiver R

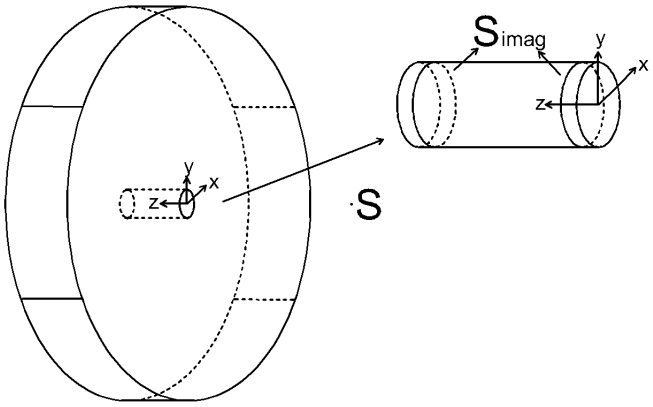

Figure 2.3: A straight pipe at the center of a cylinder

$(0.1, 0.1, -0.1)$ can be calculated approximately by

$$p_{tot} = p_{rad} + p_{inc} \tag{2.2}$$

p_{inc} in this part is the incident pressure from the source and reflected by the cylinder without pipe. p_{rad} is the pressure radiating from the open ends of the flanged straight pipe. We will compare this method with the multi-domain coupling methods proposed in the next section.

The first step to get p_{rad} is calculating the pressure p_{end} and particle velocity v_{end} at the open ends analytically. However, at the open ends the pressure and velocity are not uniform. So we can create imaginary ends for the pipe to ensure that the pressure and velocity are uniform at these ends (see Fig.2.3). Then we calculate p_{end} and v_{end} at the imaginary ends. The coordinates of the imaginary ends are $z = 0.005m$ and $z = 0.095m$. Since the pipe is straight and thin, there is only a plane wave. If we don't take into account viscous and thermal conduction losses at the rigid walls of the straight pipe, the wave equation is

$$\frac{\partial^2 p}{\partial z^2} = \frac{1}{c^2}\frac{\partial^2 p}{\partial t^2} \tag{2.3}$$

c is the sound speed.

Suppose that the solution of equation (2.3) is

$$p(z) = a\cos kz + b\sin kz \tag{2.4}$$

k is the wave number.

The convention $e^{-i\omega t}$ is adopted, where $i^2 = -1$, ρ is the density of air and ω is the angular frequency. The velocity is given as

$$v(z) = \frac{1}{i\rho\omega}\frac{\partial p}{\partial z} \tag{2.5}$$

At the right real end of the pipe ($z = 0$), the total pressure and velocity are

$$p_{rt} = a \tag{2.6}$$

$$v_{rt} = \frac{kb}{i\rho\omega} \tag{2.7}$$

From equations (2.6) and (2.7), one can get a and b. So at the left real end of the pipe ($z = l$), the pressure and velocity are

$$p_{lt} = p_{rt}\cos kl + i\rho c v_{rt}\sin kl \tag{2.8}$$

$$v_{lt} = -\frac{1}{i\rho c}(p_{rt}\sin kl - i\rho c v_{rt}\cos kl) \tag{2.9}$$

At the two real ends the pressure and velocity also satisfy

$$p_{rt} = p_{rr} + p_{ri} \qquad v_{rt} = v_{rr} + v_{ri} \tag{2.10}$$

$$p_{lt} = p_{lr} + p_{li} \qquad v_{lt} = v_{lr} + v_{li} \tag{2.11}$$

p_{rr} and v_{rr} are values of wave radiating from the right real end, and p_{lr} and v_{lr} are from the left real end. p_{ri} and v_{ri} are values of incident wave at the right real end, and p_{li} and v_{li} are at the left real end.

Substitute equation (2.10) and (2.11) into (2.8) and (2.9), one has

$$p_{rr}\cos kl + i\rho c v_{rr}\sin kl - p_{lr} = -p_{ri}\cos kl - i\rho c v_{ri}\sin kl + p_{li} \tag{2.12}$$

$$p_{rr}\sin kl - i\rho c v_{rr}\cos kl + i\rho c v_{lr} = -p_{ri}\sin kl + i\rho c v_{ri}\cos kl - i\rho c v_{li} \tag{2.13}$$

The pressure and velocity radiating from the pipe satisfy

$$\frac{p_{rr}}{v_{rr}} = -Z_r \tag{2.14}$$

$$\frac{p_{lr}}{v_{lr}} = Z_r \tag{2.15}$$

Z_r is the radiation impedance. Since the pipe is thin and the source is closed to the pipe, the flange can be considered as infinite. One has

$$Z_r \approx \rho c(\frac{1}{2}(kr)^2 - i(0.8216kr)) \tag{2.16}$$

r is the pipe radius.

From equation (2.12)-(2.15) one can obtain the following system of linear equations

$$\begin{bmatrix} \cos kl & \sin kl & -1 & 0 \\ \sin kl & -\cos kl & 0 & 1 \\ 1 & Z_r/i\rho c & 0 & 0 \\ 0 & 0 & 1 & -Z_r/i\rho c \end{bmatrix} \begin{bmatrix} p_{rr} \\ i\rho c v_{rr} \\ p_{lr} \\ i\rho c v_{lr} \end{bmatrix} = \begin{bmatrix} -p_{ri}\cos kl - i\rho c v_{ri}\sin kl + p_{li} \\ -p_{ri}\sin kl + i\rho c v_{ri}\cos kl - i\rho c v_{li} \\ 0 \\ 0 \end{bmatrix} \tag{2.17}$$

In system (2.17), p_{ri}, v_{ri}, p_{li} and v_{li} should be given. In Fig.2.3 one can close the real ends of the pipe and then put a rigid boundary condition on the whole surface. These values can be obtained by boundary element method, and so is the incident pressure p_{inc} at receiver R in the exterior domain. After substituting them into (2.17) and solving one can get the pressure p_{rr}, p_{lr} and velocity v_{rr}, v_{lr} at the two ends for a given frequency.

Then one can get a and b from equations (2.6) and (2.7). By substituting them in equation (2.4), one obtains the pressure p_{end} and v_{end} at the imaginary ends. With p_{end}, the pressure p_{rad} radiating for the pipe can be obtained by BEM. By closing the pipe at imaginary ends in Fig.2.3, putting p_{end} on the ends surfaces and rigid boundary conditions on the other part of the surface, removing the source and solving this problem by BEM, one has p_{rad} at R. Then the total pressure at the point R can be obtained by equation (2.2).

From the analyses above, we know that the pipe ends act as pistons, and surfaces of the cylinder can be considered as flanges. So the interactions between the cylinder and the exterior subdomain are acoustic incidences and radiations at pipe ends, and reflections by the surfaces. For complex networks with many ends and arbitrary flanges, the interactions with the exterior subdomains are the same. But the radiation impedances are not easy to get, so we should develop new calculation methods which are the multi-domain coupling methods introduced in the following section.

The example in this section can also be solved directly by BEM, if we create meshes of the straight pipe at the center of the cylinder. However, the pipe is very thin, so very fine meshes are needed to get converged results around the resonant frequencies. That is why we try to avoid using BEM directly to solve this example, especially for more complex networks with arbitrary flanges.

2.4 Multi-domain coupling methods

The network to be analyzed consists of cylindrical or rectangular pipes with small cross sections. For complex networks and flanges, we have to find new calculation methods, because BEM needs fine meshes leading to long computational time or

memory problems in the computers and the radiation impedances of complex flanged pipe ends are not easy to get. The calculation of the total acoustic pressure p_{tot} at a point R in the exterior domain in Fig.2.2a by multi-domain coupling methods is introduced in this section.

In boundary element methods, for a problem with a bounded domain, the integral equation to be solved is given by

$$c_e(\mathbf{x})p(\mathbf{x}) = \int_\Gamma p(\mathbf{y})\frac{\partial G}{\partial \mathbf{n}_y}(\mathbf{x},\mathbf{y})d\mathbf{y} - \int_\Gamma \frac{\partial p}{\partial \mathbf{n}_y}(\mathbf{y})G(\mathbf{x},\mathbf{y})d\mathbf{y} + p_{inc}(\mathbf{x}) \tag{2.18}$$

Γ includes the flange and the imaginary network ends (see Fig.2.2b). $p_{inc}(\mathbf{x})$ is the incident pressure from the source without the structure. G is the Green function. $\mathbf{n}$ is the unit normal vector pointing into the domain. To get the total pressure p_{tot} in the exterior domain, let $c_e(x) = 1$, and the pressure $p(\mathbf{y})$ and its derivative $\dfrac{\partial p}{\partial \mathbf{n}_y}$ on the surface Γ should be calculated first.

To get the pressure $p(\mathbf{y})$ and its derivative $\dfrac{\partial p}{\partial \mathbf{n}_y}$ on the surface Γ of a complex network with flange, the computational domain in Fig.2.2a should be divided into an exterior subdomain and an interior subdomain by creating imaginary ends for the network. The exterior subdomain is solved by BEM to get BEM system matrices and an excitation vector. The interior subdomain can be solved by analytical methods (transfer matix) or numerical methods (FEM or BEM) to get the relation between p and $q = \dfrac{\partial p}{\partial \mathbf{n}}$ at these ends. Then the exterior and interior subdomains are coupled at the interfaces. Finally by solving the overall equation system, and one has $p(\mathbf{y})$ and $\dfrac{\partial p}{\partial \mathbf{n}_y}$ on the surface Γ. The process is described in detail in the following.

2.4.1 Exterior subdomain

In Eq. (2.18), for a point $\mathbf{x}$ on Γ, $c_e(\mathbf{x})$ equals 1/2 if the surface Γ is regular at this point. The discretization of Eq. (2.18) is obtained from a mesh of the surface of the domain. Then a linear system (2.19) can be obtained whose solution gives an approximation of the solution on the surface Γ. More information can be found in [79].

$$\mathbf{AP} + \mathbf{BQ} = \mathbf{P}_{inc} \tag{2.19}$$

$\mathbf{P}$, $\mathbf{Q}$ and $\mathbf{P}_{inc}$ are vectors of pressure, derivative of pressure and incident pressure, respectively. $\mathbf{A}$ and $\mathbf{B}$ are BEM system matrices.

For the exterior subdomain in Fig.2.2b, dividing the vectors in Eq. (2.19) into vectors of imaginary ends and vectors of flange, one has

$$\mathbf{A}_E \begin{bmatrix} \mathbf{P}_{ep}^E \\ \mathbf{P}_f^E \end{bmatrix} + \mathbf{B}_E \begin{bmatrix} \mathbf{Q}_{ep}^E \\ \mathbf{Q}_f^E \end{bmatrix} = \begin{bmatrix} \mathbf{P}_{inc}^{ep} \\ \mathbf{P}_{inc}^f \end{bmatrix} \tag{2.20}$$

The subscripts and superscripts ep and f mean the imaginary ends of the pipes and flange, respectively, and E means exterior. Matrices $\mathbf{A}_E$ and $\mathbf{B}_E$ can be obtained by solving the problem in Fig.2.2b with BEM software. In the BEM software, using the rigid boundary condition on the surface Γ, one can get $\mathbf{A}_E$. Using the soft boundary condition, one can get $\mathbf{B}_E$. The incident pressure p_{inc} can be obtained in either of the two computations above.

2.4.2 Interior subdomain

For 1D parallel straight pipes, the transfer matrix can give the relation between pressures and velocities. For 2D networks, the theory of Miles [2] is suitable to get the relations. For 3D complex networks, FEM or BEM should be used to get the system equations.

2.4.2.1 One dimension without losses

The straight pipe through the flange or straight part of a network between the flange and a junction or two junctions in Fig.2.2c, whose central axis is labelled as z, is thin compared to the wavelength to be analyzed. There is only plane wave consisting of a forward travelling wave and a backward reflected wave. Pressure p and its derivated q are constant on a plane perpendicular to z. So one has the wave equation (2.3) and its solution (2.4) and (2.5).

Surfaces S_r and S_l in Fig.2.2c have different normal directions. For one node on S_r ($z = z_r$), p and q can be written as

$$\begin{aligned} p_r &= a\cos kz_r + b\sin kz_r \\ q_r &= ka\sin kz_r - kb\cos kz_r \end{aligned} \tag{2.21}$$

On S_l ($z = z_l$)

$$\begin{aligned} p_l &= a\cos kz_l + b\sin kz_l \\ q_l &= -ka\sin kz_l + kb\cos kz_l \end{aligned} \tag{2.22}$$

Get a and b from equation (2.21), and then substitute them into (2.22). The relation of p and q between one node on S_r and another node on S_l can be obtained

$$\begin{bmatrix} q_r \\ q_l \end{bmatrix} = \begin{bmatrix} t_{11} & t_{12} \\ t_{21} & t_{22} \end{bmatrix} \begin{bmatrix} p_r \\ p_l \end{bmatrix} \tag{2.23}$$

In (2.23), p can be expressed as the mean value because the pressure is constant at

each pipe end. So q of any node i on S_r and q of any node j on S_l becomes

$$\begin{bmatrix} q_{ri} \\ q_{lj} \end{bmatrix} = \begin{bmatrix} t_{11} & t_{12} \\ t_{21} & t_{22} \end{bmatrix} \begin{bmatrix} \frac{1}{n_r} \sum_{i=1}^{i=n_r} p_{ri} \\ \frac{1}{n_l} \sum_{j=1}^{j=n_l} p_{lj} \end{bmatrix} \tag{2.24}$$

Here n_r and n_l are node numbers at each end.

Thus, the relation between p vector $\mathbf{P}_e$ and q vector $\mathbf{Q}_e$ at the two ends can be written as

$$\mathbf{Q}_e = \mathbf{S}\mathbf{P}_e \tag{2.25}$$

where the transfer matrix

$$\mathbf{S} = \begin{bmatrix} \frac{t_{11}}{n_r}\mathbf{J}_{n_r,n_r} & \frac{t_{12}}{n_l}\mathbf{J}_{n_r,n_l} \\ \frac{t_{21}}{n_r}\mathbf{J}_{n_l,n_r} & \frac{t_{22}}{n_l}\mathbf{J}_{n_l,n_l} \end{bmatrix} \tag{2.26}$$

$\mathbf{J}_{i,j}$ is a matrix with i lines and j columns, where each element is equal to one.

For a body with parallel pipes, one has the system equations (2.20) for the exterior subdomain. And for the two ends of each straight pipe one has the analytical relation (2.25). Therefore the overall system can be obtained. After applying the boundary condition in section 2.2.3 to the flange and tube walls and solving the overall system, the values of p and q for each node on the whole surface Γ can be obtained.

2.4.2.2 One dimension with losses

According to the study by Kinsler [80], there are viscous losses at rigid walls of thin pipes. In this case, the equation of motion, which is given in the book [81], is

$$-\frac{\partial p}{\partial z} = \rho\frac{\partial \bar{v}}{\partial t} + R\bar{v} \tag{2.27}$$

with the average velocity $\bar{v}$ at the pipe cross-section, and the damping coefficient of the thin pipe

$$R = \frac{1}{r}\sqrt{2\eta\rho\omega} \tag{2.28}$$

where r is the radius of the circular pipe, and η is the coefficient of shear viscosity.

The equation of continuity and equation of state do not change, then the wave equation (2.29) can be obtained

$$\frac{\partial^2 p}{\partial z^2} = \frac{1}{c^2}\frac{\partial^2 p}{\partial t^2} + \frac{R}{\rho c^2}\frac{\partial p}{\partial t} \tag{2.29}$$

The solution of equation (2.29) can be given as

$$p(z) = a\cos k'z + b\sin k'z \tag{2.30}$$

with $k' = k + i\alpha$, where α is the absorption coefficient for the viscous losses

$$\alpha = \frac{1}{rc}\sqrt{\frac{\eta\omega}{2\rho}} \tag{2.31}$$

The average velocity can be obtained from the equation (2.27)

$$\bar{v} = \frac{1}{i\rho\omega - R}\frac{\partial p}{\partial z} \tag{2.32}$$

Equations, which are similar to equations (2.21)-(2.26), can be obtained, in which k should be replaced by k'. So an equation similar to equation (2.25), describing the relation between p vector $\mathbf{P}_e$ and q vector $\mathbf{Q}_e$ at the two ends, can be written as

$$\mathbf{Q}_e = \mathbf{S}'\mathbf{P}_e \tag{2.33}$$

where in matrix S', wave number k is replaced by k'.

Impedance of pipe with viscous losses is also given in the book [81]

$$Z_v = \frac{l}{\pi r^3}\sqrt{2\eta\omega\rho} - \frac{\rho l}{\pi r^2}\omega i \tag{2.34}$$

where l is the pipe length.

Thermal conduction losses should also be taken into account in thin pipes besides viscous losses according to Kinsler's measurements. The coefficient of shear viscosity η used above should be replaced by an effective coefficient η_e. The latter is defined by

$$\eta_e = \eta[1 + \frac{\gamma - 1}{\sqrt{P_r}}]^2 \tag{2.35}$$

where γ is the ratio of specific heats of air, and P_r is the Prandtl number.

For a body with parallel pipes, one has the system equations (2.20) for the exterior subdomain. And for the two ends of each straight pipe one has the analytical relation (2.33) which includes the viscous and thermal conduction losses. Therefore the overall system can be obtained. After applying the boundary condition in section 2.2.3 to the flange and tube walls and solving the overall system, the values of p and q for each node on the whole surface Γ can be obtained.

2.4.2.3 Two dimensions

In this part, all the pipes and junctions constituting a network are in the same plane and have the same depth. Only rectangular pipes and three types of junctions will be considered, which are L shaped, T shaped and cross junctions. The straight pipes have sufficiently small transverse dimensions compared to the wave length under consideration, so the higher order waves can not propagate. However, the higher order modes are required in order to satisfy the boundary conditions imposed by the junctions.

Miles first introduced the transmission line and impedance analogies for plane discontinuities in the articles [82] and [83]. Then Miles [2] gave the relations between pressures and velocities of right-angled joint ends in rectangular pipes, which can be

used to get the boundary conditions at the junction ends.

In Miles theory the propagation of the principal wave is represented by the voltage and current on a transmission line. An impedance element of the equivalent circuit for the junctions is calculated to give the effect of the high order modes on the principal wave.

The junction under consideration is shown in Fig.2.4. There are n straight pipes and one has $n = 2$ for L junction, $n = 3$ for T junction and $n = 4$ for cross junction. The problem is considered as 2D, for the incident waves are assumed to be plane and the depth of the pipes is irrelevant. The voltages and currents are respectively denoted by U_0 and I_0 at the junction ends. They are assumed related through the admittance matrix (Y_{ij}) such that

$$I_0^i = \sum_{j=1}^{n} Y_{ij} U_0^j \quad i = 1, 2, ..., n \quad (n = 2, 3 \ or \ 4) \tag{2.36}$$

The equivalent circuits of the junctions and the calculation of Y_{ij} can be seen in

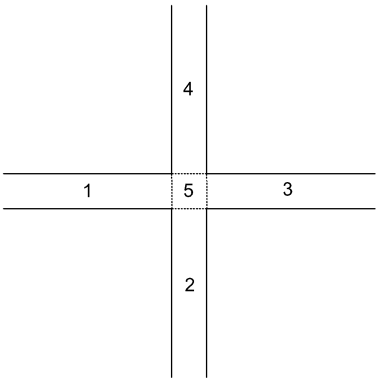

Figure 2.4: Junction

paper [2] where one can see the terms of high order modes of Y_{ij}. Here only the first approximations of Y_{ij} are given.

$$\begin{aligned} Y_{12} = Y_{21} = Y_{23} = Y_{32} = Y_{34} = Y_{43} = Y_{14} = Y_{41} = iY_0\theta^{-1} \\ Y_{13} = Y_{31} = Y_{24} = Y_{42} = iY_0 \csc\theta \\ Y_{11} = Y_{22} = Y_{33} = Y_{44} = iY_0 \cot\theta \end{aligned} \tag{2.37}$$

With $Y_0 = \rho c/S$ and $\theta = ka$. $S = a^2$ is the straight pipe cross section area.

At the junction ends, one has the relations

$$p = \sqrt{S} I_0 \tag{2.38}$$

$$v = \sqrt{S}^{-1} U_0 \tag{2.39}$$

Thus, one has the relations between pressures and velocities at the junction ends.

For a body with a 2D network, one has equations (2.36), (2.38) and (2.39) for each junction, the analytical relation (2.25) or (2.33) for the two ends of each straight pipe and the system equations (2.20) for the exterior subdomain. So one can get the overall equations system. After applying the boundary condition in section 2.2.3 to the flange and tube walls and solving the overall system, the values of p and q for each node on the whole surface Γ can be obtained.

2.4.2.4 Three dimensions

In this part two numerical methods are introduced to get the relations of pressures and velocities for the interior subdomain.

Finite element method

In the finite element method, for the network in Fig.2.2c one has

$$\mathbf{D}_a \begin{bmatrix} \ddot{\mathbf{u}} \\ \mathbf{P} \end{bmatrix} = \mathbf{P}_a \tag{2.40}$$

With $\mathbf{D}_a = \mathbf{K}_a - i\omega\mathbf{C}_a - \omega^2\mathbf{M}_a$. Subscript a repensents acoustic. $\mathbf{K}, \mathbf{C}$ and $\mathbf{M}$ are stiffness, damping and mass matrices, respectively. $\ddot{\mathbf{u}}$, $\mathbf{P}$ and $\mathbf{P}_a$ are the acceleration, sound pressure and acoustic excitation vectors, respectively. $\mathbf{D}_a$ and $\mathbf{P}_a$ can be obtained with FEM software.

In this work, Abaqus is used to get the coefficient matrix and excitation vector in equation (2.40). In Abaqus, the acoustic interface elements should be used if we want to apply the boundary conditions of accelerations on the pipe ends. The acoustic interface elements couple $\ddot{u}$ to the pressure in the acoustic medium (see the acoustic interface elements in Abaqus Analysis User's Manual).

Dividing the vectors into a vector for nodes at ends and a vector for the other nodes, one has

$$\mathbf{D}_a \begin{bmatrix} \ddot{\mathbf{u}}^I_{ep} \\ \ddot{\mathbf{u}}^I_{other} \\ \mathbf{P}^I_{ep} \\ \mathbf{P}^I_{other} \end{bmatrix} = \mathbf{P}_a \tag{2.41}$$

The superscript I means interior. At the interfaces between the exterior subdomain and interior subdomain, the pressure and acceleration are continuous. One has

$$\mathbf{P}^I_{ep} = \mathbf{P}^E_{ep} \tag{2.42}$$

and

$$\ddot{\mathbf{u}}^I_{ep} = -\frac{1}{\rho}\mathbf{Q}^E_{ep} \tag{2.43}$$

Identical meshes are needed to match the boundary conditions at the interfaces.

For a body with a network in Fig.2.2c, the overall system can be assembled with systems (2.20) and (2.41)-(2.43). After applying the boundary condition in section 2.2.3 to the flange and tube walls and solving the overall system, the values of p and q for each node on the whole surface Γ can be obtained.

Boundary element method

Besides FEM, BEM also can be used for the interior subdomain. To make a further reduction of the BEM matrix size and save computational costs, the interior subdomain can be divided into several subdomains: straight pipes and junctions. We can only mesh the junctions, and use the transfer matrix instead of meshing the straight pipes.

For the problem of a flanged network in Fig.2.2c one creates imaginary surfaces for network junctions. These surfaces should be perpendicular to the network walls. One can see the junction subdomain in Fig.2.2c. The normal direction of surface junction S_{jun} points inward.

The system equations for the junction are similar to equation (2.20). Since for the junction subdomain there is no source, the incident pressure equals zero, and one has

$$\mathbf{A}_I \begin{bmatrix} \mathbf{P}^I_{ej} \\ \mathbf{P}^I_w \end{bmatrix} + \mathbf{B}_I \begin{bmatrix} \mathbf{Q}^I_{ej} \\ \mathbf{Q}^I_w \end{bmatrix} = \begin{bmatrix} \mathbf{0} \\ \mathbf{0} \end{bmatrix} \tag{2.44}$$

The subscripts and superscripts ej and w mean the imaginary ends and the walls of the junction. Matrices $\mathbf{A}_I$ and $\mathbf{B}_I$ can be obtained by running BEM software.

For the whole problem of a flanged network in Fig.2.2a, one has the systems (2.20), (2.25) or (2.33) of two ends of each straight pipe and (2.44) for each junction, so the overall system can be assembled. After applying the boundary condition in section 2.2.3 to the flange and tube walls and solving the overall system, the values of p and q for each node on the surfaces Γ can be obtained.

2.5 Simulations

2.5.1 Calculations without losses

In this section, viscous and thermal conduction losses are ignored. First three examples are calculated by the methods introduced above. Comparisons of these methods are given. The first example is a straight pipe at the center of a cylinder. The seconde one is a T pipe at the center of a cuboid. The third one is a 2D network between a tire and a road. For simple straight networks with flat flanges, there are analytical solutions for interior acoustic fields. Full BEM also works although the computational costs are high around the resonant frequencies. Multi-domain coupling method with 1D interior relations can be used for the calculations as well. For a T pipe, the multi-domain

coupling methods with 3D interior relations introduced before are compared with full BEM. For a network between the tire and the road, multi-domain coupling methods with 2D interior relations are compared with the one with 3D interior relations. Then 3D networks at the center of a cuboid is computed to show the possibilities of the proposed methods to solve problems of complex networks. For the complex networks multi-domain coupling method with 3D interior relations is used to calculate the acoustic fields.

2.5.1.1 Straight pipe

One can solve the problem in Fig.2.3 by the multi-domain coupling methods introduced in section 2.4. There is no junction, so the systems (2.20) and (2.25) are needed.

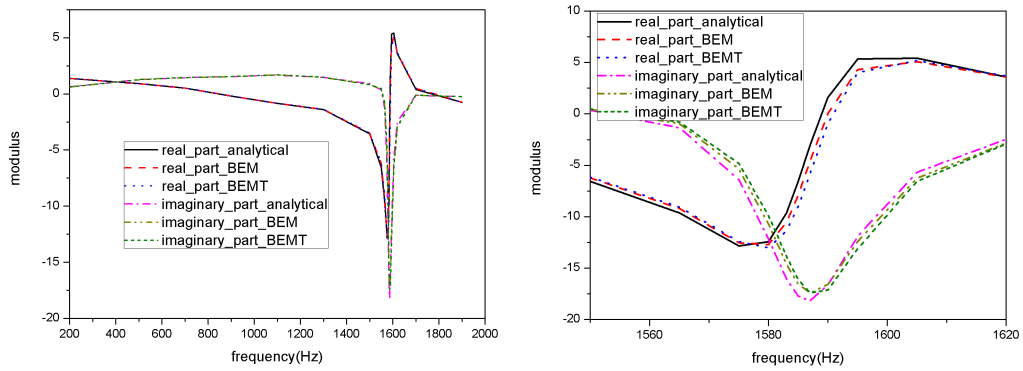

Figure 2.5: Pressure at the imaginary end of a straight pipe: (a) $200 - 2000Hz$; (b) Around the resonant frequencies

Fig.2.5a and 2.6a are the pressures at the right imaginary end of the straight pipe and at point $R(0.1, 0.1, -0.1)$ calculated by three methods. Good agreement can be seen in these figures. From Fig.2.5a we can see that the resonant frequency is about $1600Hz$. The error of pressure between two different methods can be calculated by $error = |p_1 - p_2|/|p_1|$. BEMT means BEM is used for the exterior subdomain and transfer matrix is used for the interior subdomain. Analytical methods in Fig.2.6a mean the radiation impedance methods introduced before. Around the resonant frequency at point R, the maximum error between BEMT and BEM is 2.6%. The maximum error between BEMT and analytical methods is 5.1%, and is 4.9% between BEM and analytical methods. In the analytical methods, the assumption of uniform pressure at the real pipe ends is used. Actually it is not a plane wave at the real ends, for the pipe radius changes suddenly. This assumption brings errors.

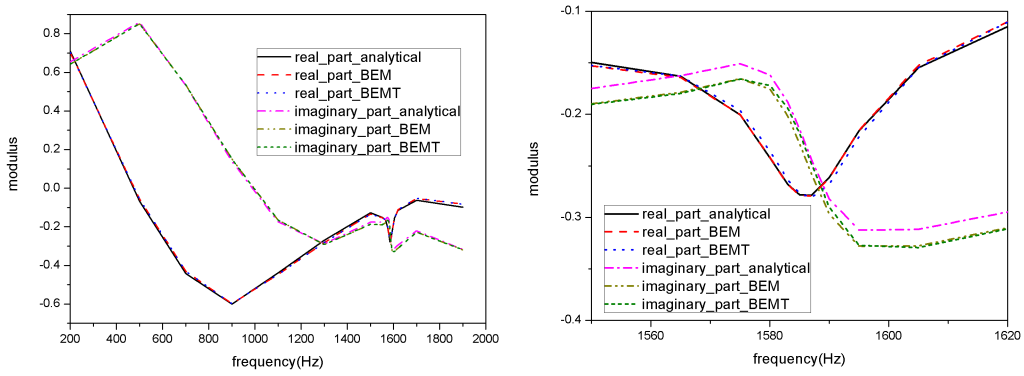

(a) (b)

Figure 2.6: Pressure at receiver R: (a) $200 - 2000Hz$; (b) Around the resonant frequencies

Good results can be seen in the example above, although the transfer matrix is only a 1D relation while the full BEM is a 3D method. We can conclude that the transfer matrix can be used for straight parts of interior subdomains in the multi-domain modelling.

2.5.1.2 T pipe

The flange in this example is a hexahedron. There is a T pipe at the center (see Fig.2.7). The flange and pipe walls are rigid. The cross section of the pipe and the flange is $0.02 \times 0.02m$ and $0.3 \times 0.3m$ respectively. The pipe length is $0.1m$ and the branch length is $0.14m$. The source S is at $(0, 0, -0.1)$. Since the T pipe is simple, full BEM of one computational domain can be used to solve this problem. If the computational domain is divided into two subdomains, the multi-domain coupling methods proposed in this chapter can also be used.

We can use FEM to solve the interior subdomain. We create imaginary ends $S_{imag,p}$ for the T pipe as the interfaces between the exterior and interior subdomains to ensure that the pressure is uniform and the velocity is perpendicular to the ends. The distance between imaginary ends and real ends is $0.005m$(see Fig.2.7). Assembling systems (2.20) and (2.41)-(2.43), applying the rigid boundary condition in section 2.2.3 to the flange and tube walls and solving the overall system, the values of p and q for each node on the whole surface can be obtained. Then the pressure in the exterior domain can be calculated by equation (2.18).

BEM can also be used to solve the interior subdomain. We create imaginary surfaces $S_{imag,j}$ for the junction. Thus, we can use different numbers of elements and

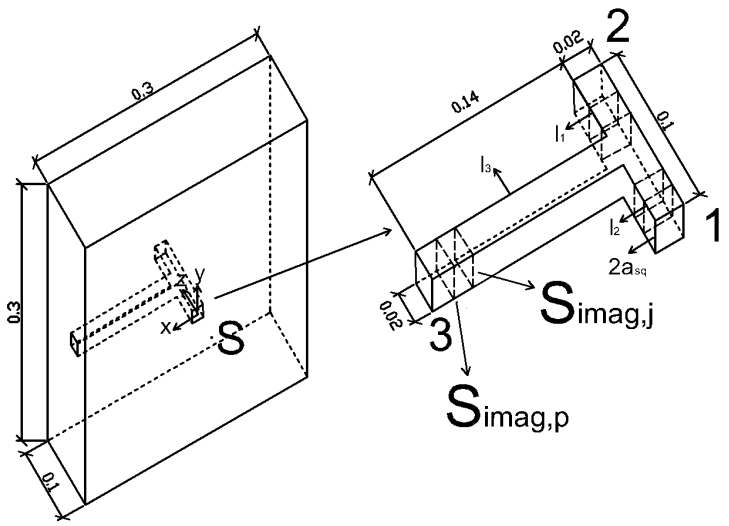

Figure 2.7: T pipe with rectangular flange

nodes on the two imaginary ends $S_{imag,j}$ and $S_{imag,p}$. It is easier to create the mesh. The distance between $S_{imag,p}$ and $S_{imag,j}$ is $0.005m$. The new interior subdomain is formed by pipe walls and the junction imaginary ends $S_{imag,j}$. The short straight parts between the exterior and new interior subdomains can be described by a transfer matrix. Assemble and solve Eqs. (2.20), (2.25) of each couple of imaginary surfaces $S_{imag,p}$ and $S_{imag,j}$ and (2.44), one can get the solution. By Eq. (2.18) one has the sound pressure field.

Fig.2.8a and Fig.2.9 are the pressures at the imaginary end ($z = 0.005m$) and at point R $(0.1, 0.1, -0.1)$ calculated by three methods. We can see good agreement. BFEM means BEM is used for the exterior subdomain and FEM is used for the interior subdomain. BBEM means BEM is used for the exterior subdomain and BEM is used for the interior subdomain.

From Fig.2.8a we can see that one resonant frequency is about $1600Hz$. Around the resonant frequency $1600Hz$ at the imaginary end ($z = 0.005m$), the maximum error of pressure between BBEM and BEM is 9.22%. Compared to BEM, there is a small resonant frequency shift for BFEM, about $5Hz$, and the error of the maximum pressure between BEM and BFEM is 3.39%. In BFEM the more elements are used, the smaller the frequency shift is.

In Fig.2.9 at receiver R the maximum error of pressure between BBEM and BEM is 1.35%, and the error of the maximum pressure between BEM and BFEM is 1.48%.

In this example, there is another resonant frequency within $2000Hz$, about $900Hz$, which can be obtained by the methods proposed in chapter 3. Around $900Hz$ we can

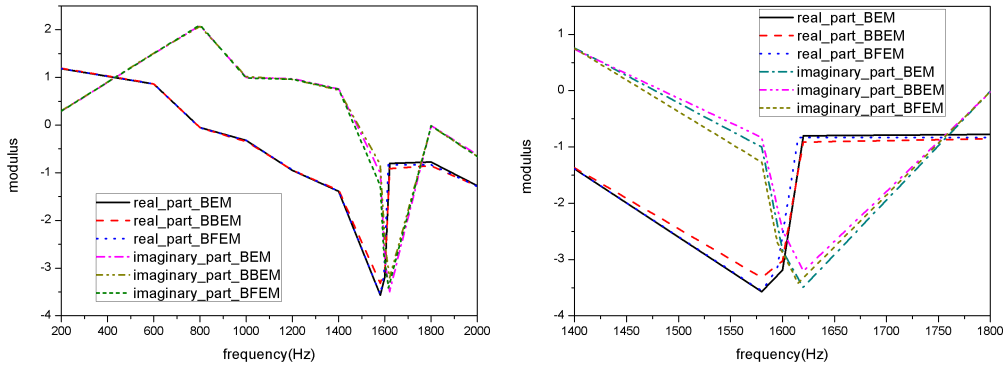

(a) (b)

Figure 2.8: Pressure at the imaginary end ($z = 0.005m$): (a) $200 - 2000Hz$; (b) Around the second resonant frequencies

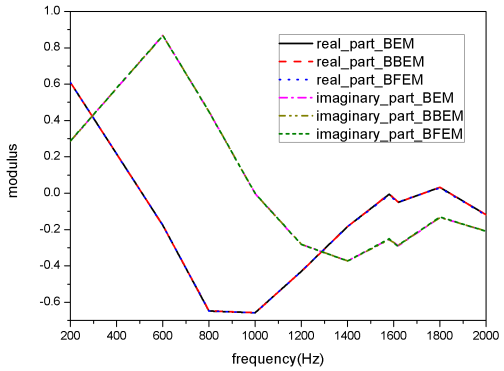

Figure 2.9: Pressure at point R near flange

also see very good agreements.

For this T pipe BBEM and BFEM, which are multi-domain coupling methods with 3D interior relations, have very good accuracy compared with full BEM. In BFEM, modelling the network is easier than in BBEM. BBEM is more suitable for networks with long straight parts, for the straight parts can be described with transfer matrices, thus less elements would be used. For complex networks they are better than BEM because BEM leads to high computational costs. But if the complex networks can be considered as 2D networks with right angle junctions, multi-domain coupling methods with 2D interior relations would be faster and easier to used than BBEM and BFEM. An example of 2D network is given in the following and comparisons with BFEM are shown.

2.5.1.3 Network between the tire and the road

In order to compare BFEM (BEM for the exterior subdomain and FEM for the network) and A2BEM (2D analytical relation for the network and BEM for the exterior subdomain), the network shown in Fig.2.10b between the tire and the road in Fig.2.10a is calculated by these two methods. In this example, the round surface in Fig.2.10a is the tire, and the rigid plane surface is the road. The radius of the round surface is $0.27m$, and its width is $0.015m$. The dimensions of the contact zone between the tire and the road are $0.01 \times 0.015m$. The network can be considered as a 2D network because all the pipes are in the same plane. Acoustic pressure at receiver R $(1, 0, 0.265)$ outside the tire and road can be seen in Fig.2.11.

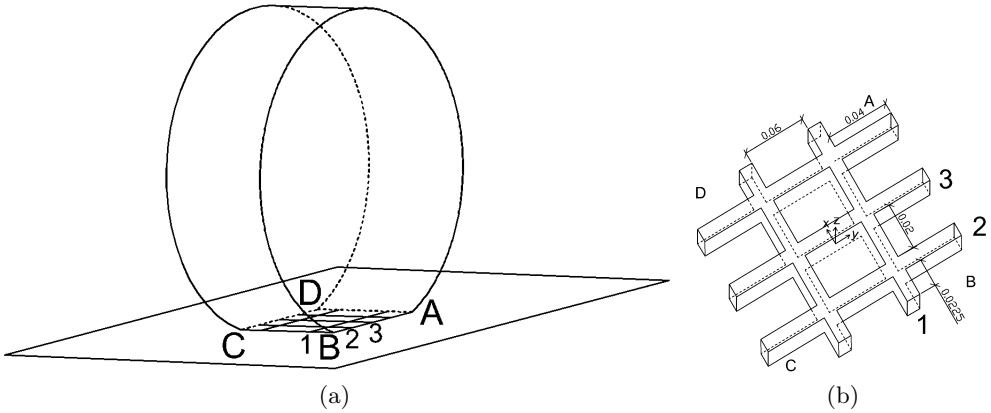

(a) (b)

Figure 2.10: (a) Network between a round surface and a rigid plane surface; (b) The network with open ends.

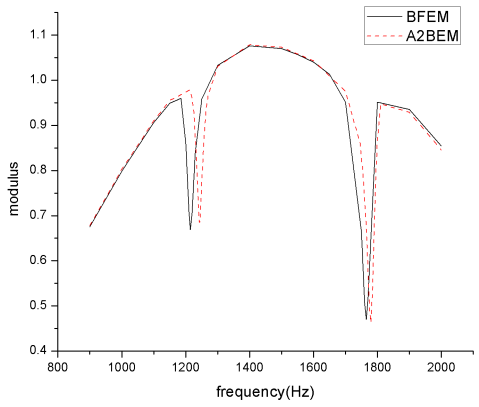

Figure 2.11: Pressure at point R outside the tire

There are several assumptions when modelling tire treads: a. there are only longitudinal grooves on the tire surface except in the contact zone, b. there are

only right-angled junctions in the networks in the contact zone, c. the pipes in the networks have the same cross-section. An example of network between the tire and the road is meshed in Fig.2.12.

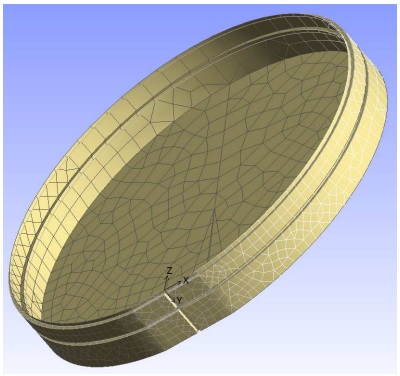

Figure 2.12: Half of a tire with a network in the contact zone between a tire and a road

The resonant frequencies obtained by matlab code 2DNRF developed in chapter 3 are $1224Hz$ and $1770Hz$. Around these two resonant frequencies, there are two valleys which are caused by the acoustic wave radiated from the network ends. Small shifts of the valleys between the two computational methods can be seen. The shift of the first valley is about $30Hz$, and for the second valley the shift is only $14Hz$. However, the values of valleys of the two computational methods are quite close, and the differences of the valleys between these two methods are 2.96% and 1.42%, respectively. For the non-resonant frequencies, the acoustic pressures between the two methods are almost the same.

Compared to BFEM, A2BEM can give acceptable results. So either of the two methods proposed in this chapter can be used to calculate the sound pressure fields of bodies with 2D right-angled network inside. But A2BEM is much easier to use because there is no need to mesh the network with FEM software.

2.5.1.4 Complex network

In order to explore the possibilities of calculating complex 3D networks by the methods introduced above in this chapter, flanged complicated networks (see Fig.2.13a and 2.13b) are calculated by the proposed method. Single domain full BEM doesn't work because of too many nodes. We divide the computational domain into two subdomains by creating imaginary ends, and FEM is used for the interior subdomain.

The flange size is $0.15 \times 0.15 \times 0.1034m$. The pipe cross sections are $a \times a = 0.01 \times 0.01m$ and $b \times c = 0.01 \times 0.005m$. The distance between two pipes is $0.025m$.

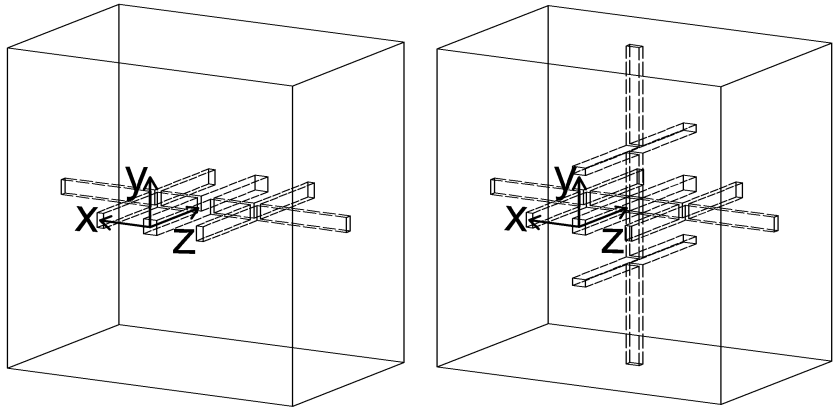

(a) (b)

Figure 2.13: (a) Network 1; (b) Network 2

The flange and network walls are rigid. The source S is at $(0, 0, -0.01)$. The observer R is at $(0, 0, -1)$.

Besides these two networks, a straight pipe and a cross pipe at the body center are also calculated, respectively. Comparisons of sound pressure fields for bodies with pipes and without pipes are shown in Fig.2.14a. Fig.2.14b shows the results around the resonant frequencies. The sound pressures increase and then decrease around the

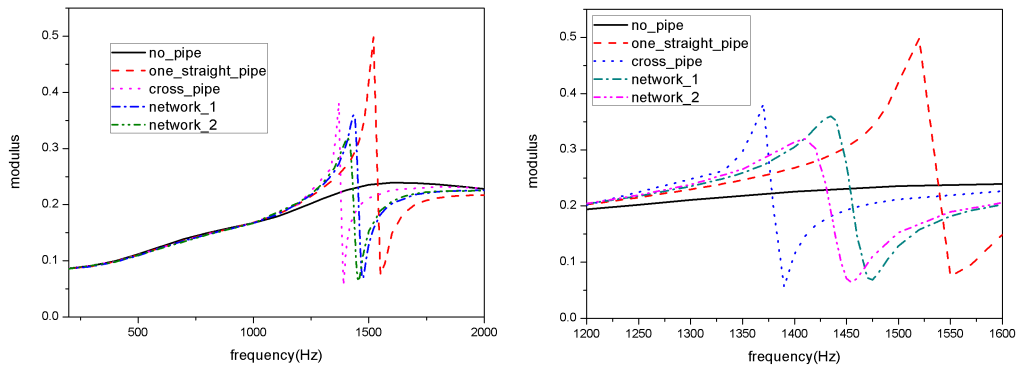

(a) (b)

Figure 2.14: Modulus of sound pressure at R: (a) $200 - 200HZ$; (b) Around the resonant frequencies

resonant frequencies of different pipes in Fig.2.14b. Compared with the body without pipe, the maximum pressure decreases of bodies with pipes are almost the same, about

72%. But the maximum pressure increases vary, and the pressure increase of network 2 is the smallest, about 41.5%. The pressures in a circle around the body at three

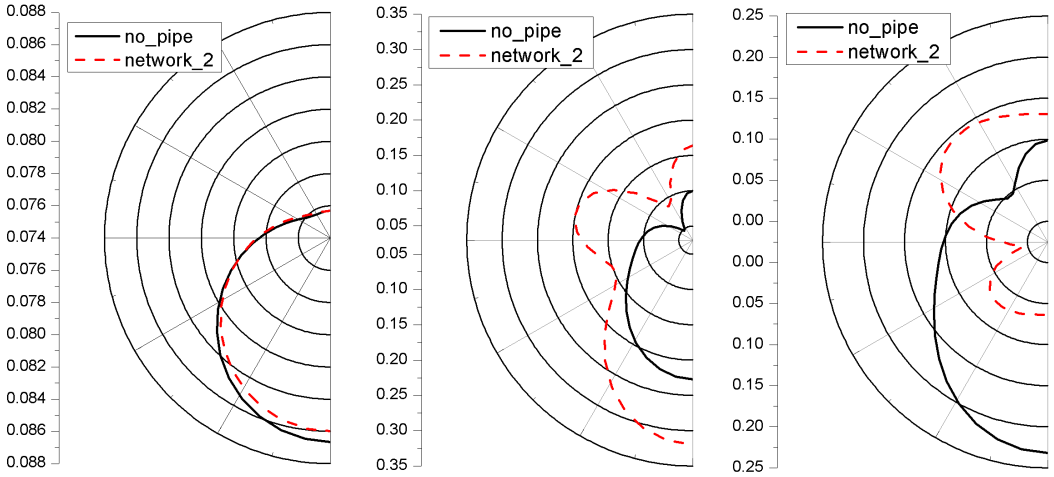

(a) (b) (c)

Figure 2.15: Pressure modulus in a circle around the body (a) Frequency $200Hz$; (b) Frequency $1410Hz$; (c) Frequency $1455Hz$

frequencies ($200Hz$, $1410Hz$ and $1455Hz$) are calculated. At receiver R, network 2 has the maximum pressure at $1410Hz$, and minimum pressure at $1455Hz$. Since plane yz is a plane of symmetry of the body, only half of the circle ($x > 0$) is shown in Fig.2.15a, 2.15b and 2.15c. The circle is in plane xz. The center is at point $(0, 0, 0)$ and its radius is $1m$.

At $200Hz$ the influence of network 2 is quite small, because the wavelength is very long compared to the cross section of network. At $1410Hz$ for network 2 the pressures increase around the body. At $1455Hz$ we can see big reductions in front of the body ($z > 0$) for network 2.

2.5.2 Calculations with losses

From the calculations and comparisons in section 2.5.1 we can see good agreements of different methods we introduced in this chapter. However, we didn't take into account the viscous and thermal conduction losses at the rigid pipe walls in the calculations above. For pipes with large cross-sections, losses are not necessary. But according to previous researches and our experiments, for the pipe dimensions in which we are interested losses should be considered in the simulations. So in this section, we will give some examples to show the influences of viscous and thermal conduction losses on the acoustic fields.

In this section we calculate the acoustic fields of pipes between a round surface and a plane surface in Fig.2.10a. The round surface in this section is a smooth cylinder. Its radius is $0.27m$ and width is $0.15m$. The contact zone between the cylinder and the plane surface is $0.15m \times 0.1m$.

2.5.2.1 Straight pipe

In the contact zone in Fig.2.10a, there is a longitudinal straight pipe at the center. The pipe cross-section is $0.005m \times 0.01m$. Since the pipe is very simple, we can use BEM directly to get the acoustic fields by meshing the cylinder and the straight pipe first. The meshes can be seen in Fig.2.16a. Since the cylinder has a symmetric plane, half of the cylinder is meshed.

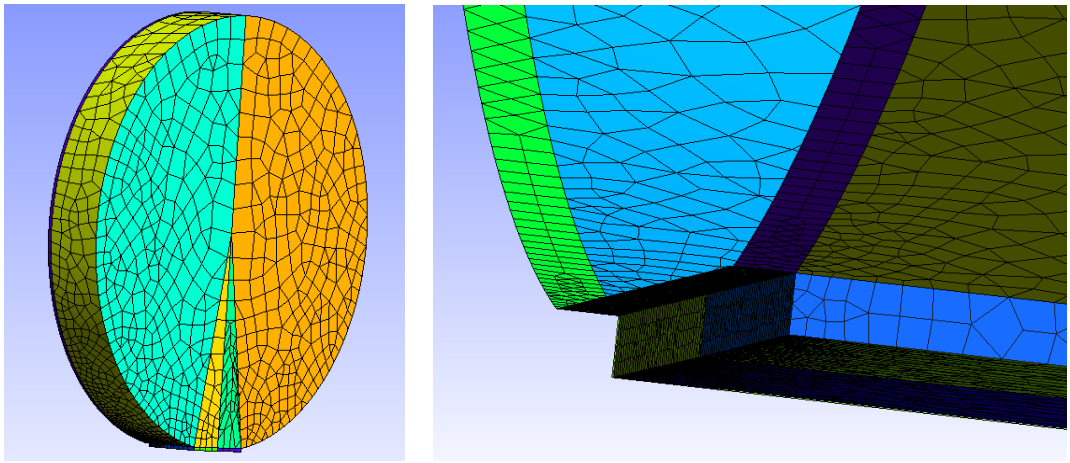

(a) (b)

Figure 2.16: (a) Meshes of half a cylinder with half of a straight pipe at the center of the contact zone; (b) Details of meshes of the contact zone.

The source is at $(0.1, 0, 0.005)$. The results at $(1, 0, 0.06)$ can be seen in Fig.2.17. The solid line, dash line and dot line are results for no pipe, one straight pipe without losses and one one straight pipe with viscous losses respectively. The viscous losses are taken into account in the BEM calculations by an impedance which is given by equation (2.34). The difference of SPL between the solid line and the dot line is $5.5dB$ at the resonant frequency $1430Hz$, and is $6.8dB$ between the solid line and dash line at the resonant frequency $1460Hz$. The resonant frequency has a small shift of $30Hz$. By using the viscous losses, the differences become smaller.

The numerical results of this example will be compared with measurements in chapter 5.

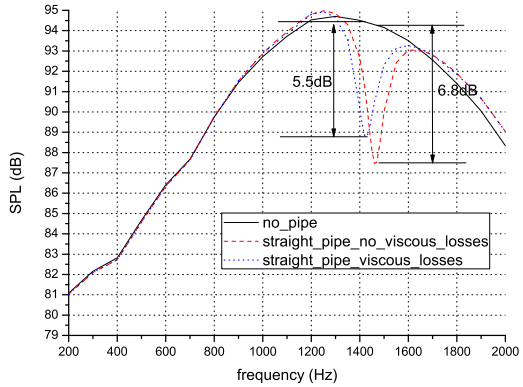

Figure 2.17: Predicted results for a straight pipe between a cylinder and a plane surface

2.5.2.2 Network

In the contact zone in Fig.2.10a, there is a network at the center which can be seen in Fig.2.10b. In the network, there are two longitudinal (x direction in Fig.2.10b) and three transverse branches (y direction). The network has symmetric planes xz and yz. The plane surface is in plane xy. The pipe width is $0.009m$. Since the cylinder has symmetric plane xz, half of the cylinder without network is meshed with 2D elements. Then this problem is solved by the method 'A2BEM' proposed in this work. The source is at $(0.1, 0, 0.005)$.

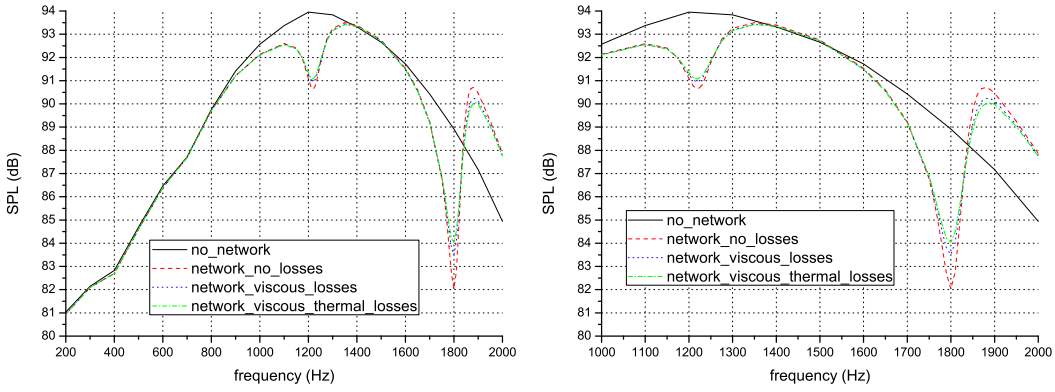

(a) (b)

Figure 2.18: Predicted results for a network between a cylinder and a plane surface: (a) $200 - 2000HZ$; (b) Around the resonant frequencies

The results at $(1, 0, 0.06)$ are shown in Fig.2.18a where we can see two obvious variations of SPL around the resonant frequencies compared to the solid line. The first variations are reductions around $1220Hz$, and the second variations are reductions

and amplifications around $1850Hz$.

From table 2.1 we can see the influences of viscous and thermal conduction losses on the SPL. At the frequencies of three SPL extrema, the more losses we take into account, the smaller the SPL differences between the case without network and the case with one network are.

The numerical results are validated by experiments in chapter 5.

Table 2.1: Differences of SPL in Fig.2.18a between the case without network and the case with one network around resonant frequencies

Frequencies	No losses	Viscous losses	VT losses
1220 Hz	$3.30dB$	$2.98dB$	$2.85dB$
1800 Hz	$6.89dB$	$5.41dB$	$4.88dB$
1880 Hz	$3.13dB$	$2.65dB$	$2.44dB$

Note: Viscous and thermal conduction losses (VT losses)

2.6 Conclusions

From the simple structure solved by the radiation impedance methods, we can conclude that for networks in horn-like structures pipe open ends act as pistons, and the structure surfaces can be considered as flanges. The interactions between the structure and exterior subdomain are acoustic incidences and radiations at pipe open ends, and reflections by the structure surfaces.

The multi-domain coupling methods proposed in this chapter make it possible to calculate the three-dimensional sound pressure field of complex networks with arbitrary flanges. It uses substructuring techniques, transfer matrix for the straight pipe part, analytical acoustic relations for the 2D junctions and numerical methods for the 3D parts to reduce mesh nodes, elements and the matrix size and to save computational costs. It combines the advantages of numerical methods and analytical relations together.

The influence of the network on the acoustic fields mainly results from the pipe resonances. The viscous and thermal conductivity losses can give small corrections. If no viscous and thermal conductivity losses are taken into account, the multi-domain coupling methods can still be applied to the estimation of the tendencies of the acoustic pressure and the resonant frequencies.

The resonances of air columns in networks can be used for reducing sound pressures at resonant frequencies for horn-like structures. However, the resonant frequencies should be estimated correctly first, and this will be introduced in the next chapter.

Chapter 3

Calculation of network resonant frequencies

In networks with arbitrary flange, the sound pressure fields are quite large around the resonant frequencies. So the exterior acoustic fields will be greatly influenced by the networks. In order to calculate this influence, resonant frequencies should be estimated. Methods for estimating resonant frequencies of 1D and 2D flanged pipes with small cross-sections are discussed in this part. For simple pipes, there are analytical solutions, but for complex networks numerical methods should be used. Since the pipes to be discussed may have open ends, end corrections will be introduced first.

3.1 Determination of end corrections

The length is an important parameter for calculating the resonant frequencies of a network with open ends. A short distance should be added to each end of the network to get precise results. This short distance is called the end correction, which makes each straight part of the network a little longer than its physical length.

From the perspective of waves, standing waves occur during the network resonances. The sound waves are reflecting at open ends, which are not perfectly at the end sections of the network, but at small distances (end corrections) outside the network.

3.1.1 Previous researches

The end corrections of the network open ends can be obtained from the radiation impedances which have small but finite values by (3.1) from [3].

$$\tilde{\delta} = \mathbf{Re}[k^{-1} \arctan(\frac{-Z_r}{i\rho c})] \tag{3.1}$$

The upper script $\sim$ means that it is a frequency-dependent quantity. Here only the real part of the end correction is considered, which is the most useful in the present study.

The radiation impedance depends on details of the flange geometry of the open end and the frequencies. For the cases of a circular pipe with circular flanges of infinite and zero radii, there are precise theoretical solutions of the end corrections. In these two extreme cases the end corrections for low frequencies are $0.8216a$ and $0.6133a$, respectively [84–86] where a is the inner radius of the pipe. For a circular flange with finite dimensions the end corrections are between those two cases, and there are experimental and analytical investigations on this. Benade and Murday [87] and Peters *et al.* [88] performed experiments. Ando [89] analytically gave an approximate formula for such a case, but to get accurate results a large number of terms of the expansion should be taken into account, which leads to complex computations and precludes its application.

Dalmont *et al.* [3] used numerical methods and experiments to get fit formulas of end corrections for circular pipes and finite flanges with various radii. Since the values of end corrections for other flange shapes found on wind musical instruments are also very interesting, various other flanges were investigated as well in [3]: spherical and cylindrical flanges, square flanges, the normalised flange, short flaring horns and a disk at a certain distance above the open end.

3.1.2 Numerical procedures

Dalmont's numerical methods of BEM are introduced and used in this part. To estimate the end corrections of the network between a tire and a road, the radiation impedances of the open ends should be calculated first by the impedance transfer equation of acoustic transmission line (3.2) from [3], because Z_r cannot be calculated or measured directly at the pipe end.

$$Z_r = -i\rho c \tan[\arctan(\frac{-Z_l}{i\rho c}) - kl] \tag{3.2}$$

Z_l is the impedance at an abscissa $x = -l$, i.e., at a distance l from the open end. It can be calculated by numerical methods. Boundary element method is used to do the calculations.

Equation (3.2) means that the radiation impedance can be obtained from the case where Z_l is an input impedance of a pipe of length l. Then the end corrections can be obtained by (3.1).

A simple case, consisting in a circular pipe with an infinite flange, is solved by BEM in order to introduce the calculations procedures and to check the feasibility of this numerical methods, because there is a simple fit formula (3.3) ($kr < 3.5$) by Norris and Sheng [90] for this case.

$$\tilde{\delta}_\infty = \delta_\infty [1 + \frac{(0.77kr)^2}{1 + 0.77kr}]^{-1} \tag{3.3}$$

with $\delta_\infty = 0.8216r$ and $k = 2\pi f/c$ where r is the pipe radius and f is the frequency.

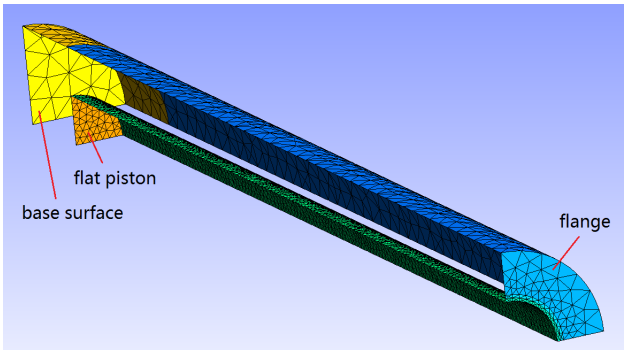

Figure 3.1: Mesh of the boundary element model of a tube with a circular flange (case r/R =1/2)

Since symmetric planes exist, only one-quarter of the geometry is meshed by Gmsh in Fig.3.1. The model is a circular pipe of radius $r = 0.005m$ and length $0.1m$, which has an open end and a closed end. The circular flange of radius $R = 0.6m$ is connected with the open end, and the flange is used to simulate the infinite flange since the pipe radius is very small compared to the flange radius. The closed end acts as a flat piston moving with a prescribed velocity, which is a normal unit velocity. There is a base surface behind the piston and it causes acoustic reflections. A small impedance equal to $0.1P_a \cdot s/m$ is applied to the base surface to minimize the reflections. This is an absorption boundary condition. Other parts of the model are rigid.

The BEM software Samray is used to compute the model. There is a node at the centre of the piston mesh. The acoustic pressure at this node can be calculated by Samray. Since the acoustic velocity is unity, the impedance of the piston can be obtained. Then the radiation impedance is deduced from this impedance by equation (3.2).

Fig.3.2a from paper (3.3) shows the fit formula (3.3), BEM and experimental results of end corrections ($ka < 2$). The agreement between the results is good. For

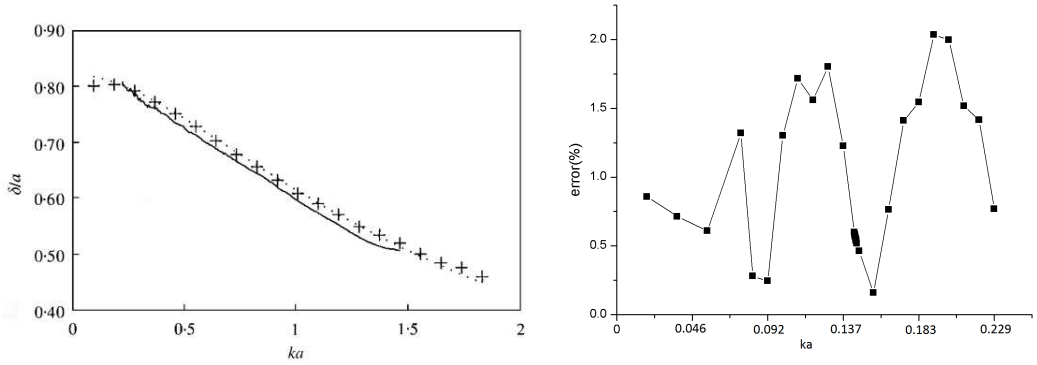

(a) (b)

Figure 3.2: (a) End corrections divided by pipe radius from [3] (ka<2): (dots) fit formula (3.3) results, (plus sign) BEM results by Dalmont, (straight line) experimental results; (b) Errors between fit formula and BEM results (ka<0.23). (Symbol a in the figures represents the radius r)

the computations in this part, ka is less than 0.23, and the maximum error of end corrections between the fit formula (3.3) and our BEM model is about 2%, which can be seen in Fig.3.2b. In Fig.3.2a when $ka < 0.23$ we can also see small differences of the results. Since the end corrections are used to estimate the resonant frequencies around which the acoustic fields will be calculated at several frequencies, the results obtained in Fig.3.2b are good enough and accepted. So this numerical methods can be used to calculate the end corrections of networks with flanges of tire and road surfaces, which is shown in the following section.

3.1.3 Complex flanges and networks

The values of end corrections depend on flange shapes. An open pipe end with different flange shapes has different end corrections. In this section, end corrections of networks with different flanges are calculated by the numerical methods introduced before. In section 3.1.2 the flange is flat, but in this section the flanges are a round surface and a plane surface.

For 2D networks with complex flanges, the numerical procedures introduced before are used to get the end correction of each open end in order to estimate the resonant frequencies. In this part, networks with two types of round flanges are calculated. The first one is a cylinder, and the second one is a tire surface, both of which are on plane surfaces. In Fig.2.10a there is a network between a round surface and a rigid plane surface. In the contact zone, the surface is flat.

As for networks, there are only longitudinal and transverse pipes constituting the

networks and these two types of pipes are perpendicular. Only the end corrections of longitudinal pipes will be discussed. For transverse pipes they can be calculated approximately by Dalmont's fit formula of rectangular flanges (see the calculations in 3.3.2) because the flange of transverse ends is flat.

The longitudinal pipes at different positions have different shapes and dimensions of the flanges. Although their ends may not be in the middle of the flanges, in the interest of simplicity they are assumed in the middle of the flanges.

3.1.3.1 Flange of cylinder

In this section the round surface in Fig.2.10a is a cylinder. There is a network between the cylinder and the rigid plane surface. In the contact zone, the cylinder surface is flat.

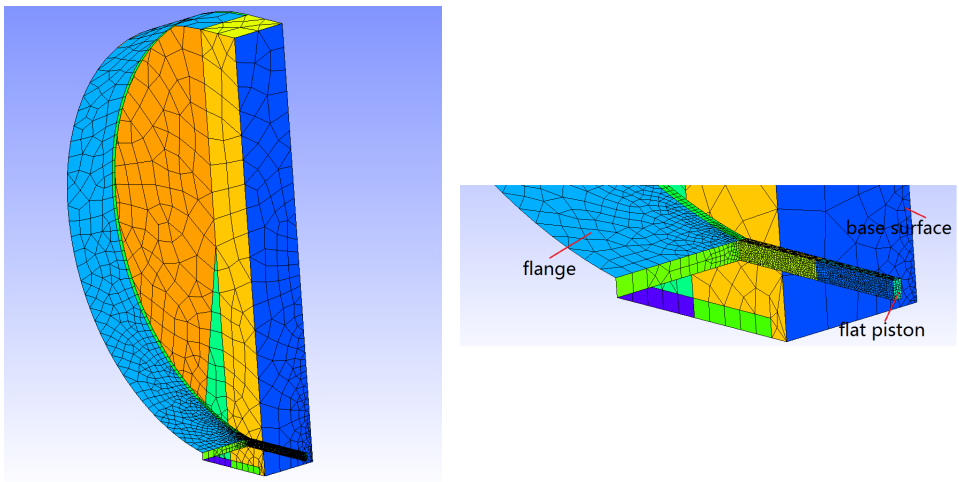

(a) (b)

Figure 3.3: (a) Half of meshes of the boundary element model of a rectangular tube with a flange of cylinder; (b) Details of the mesh of the tube.

In order to calculate the end corrections of longitudinal pipes, half a cylinder is meshed for BEM, which is shown in Fig.3.3a and 3.3b. The model is similar to the one in Fig.3.1. Since the plane surface is rigid, it can be considered as a symmetric plane. Another symmetric plane of the cylinder exists, so only half of the cylinder is meshed. The half pipe has rectangular cross-section with area of $0.0045m \times 0.009m$. The length is $0.1m$. It has an open end and a closed end which has unity velocity as boundary condition. The base surface behind the piston is modelled as flat to reduce the elements because the flange shape behind the piston has no influence on the end correction of the open end of this pipe. It has a very small impedance which is used

to minimize the reflections. Other parts of the model are rigid.

The acoustic pressure at the central node of the closed end is calculated by Samray. The acoustic velocity is unity, so the impedance of the piston is obtained. Then the radiation impedance is calculated from this impedance by equation (3.2).

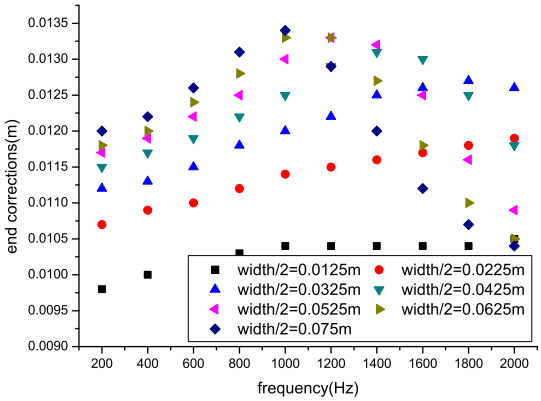

Figure 3.4: End corrections of longitudinal pipes with cylindrical flanges of different widths within $2000Hz$ ($ka < 0.23$)

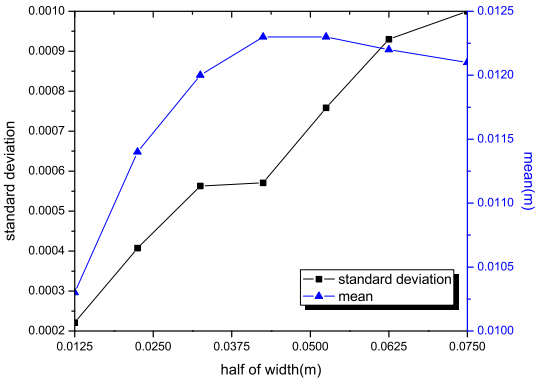

Figure 3.5: Standard deviations and mean values of end corrections of longitudinal pipes with cylindrical flanges of different widths

The end corrections of the longitudinal pipe for cylinders of different widths are shown in Fig.3.4 ($ka < 0.23$), and the frequency interval is $200Hz$. The cylinder radius is $0.27m$. For each width of the cylinder, the end corrections are frequency-dependent, but their standard deviations are very small (see Fig.3.5), which indicates that they tend to be very close to the mean values. The standard deviation is calculated by equation (3.4). So the mean values of end corrections for each width in Fig.3.5 are

used to get a fit formula of end corrections (3.5), in which w is half of the width.

$$\sigma = \sqrt{\frac{1}{N}\sum_{i=1}^{N}(x_i - \mu)^2} \tag{3.4}$$

with $\mu = \frac{1}{N}\sum_{i=1}^{N} x_i$, where x_i is the end correction at each frequency and N is the number of frequencies calculated.

$$\delta = 0.00808 + 0.22128w - 3.72112w^2 + 19.80897w^3 \tag{3.5}$$

The same procedure can be used to get fit formulas for other pipes and flanges of different shapes and dimensions.

3.1.3.2 Flanges of tire

The network between a tire and a road calculated in this part is similar to the cylinder case in section 3.1.3.1. An example of network is on the tire surface which can be seen in Fig.2.12. The road surface can be considered as a rigid plane surface, and the tire surface can be considered as a cylinder with grooves. The network in the contact zone between the tire and the road can be considered as a flanged 2D network. In order to estimate the resonant frequencies of the network, the end correction of each open end should be known.

There are several hypotheses for the discussions of tire/road cases:

a) The contact zone is a rectangle.

b) The network just includes longitudinal and transverse pipes.

c) There is no transverse groove on the tire surfaces except in the contact zone.

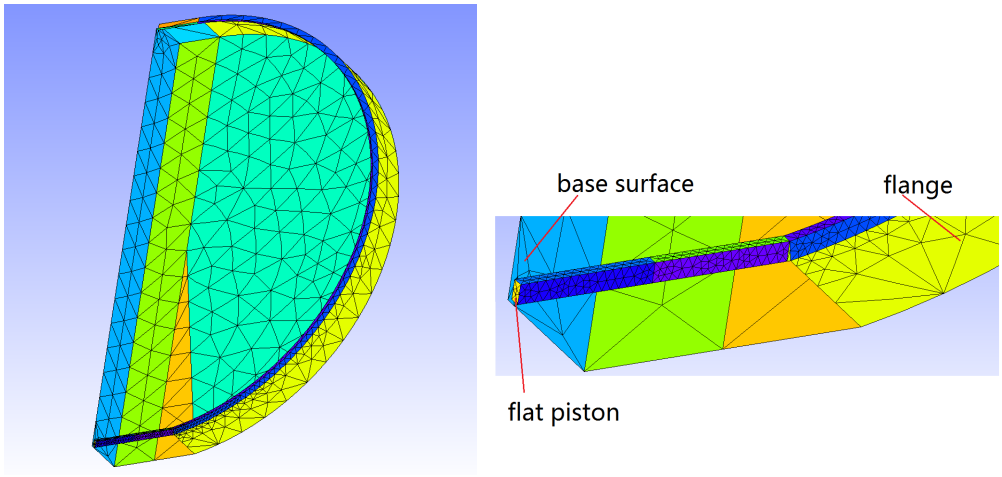

(a) (b)

Figure 3.6: (a) Half of meshes of the boundary element model of a rectangular tube with a part of tire flange; (b) Details of the mesh of the tube.

For calculating the end corrections of longitudinal pipes, the BEM mesh of half tire is shown in Fig.3.6a and 3.6b. The model is similar to the one in Fig.3.1. Since the road is rigid, it can be considered as a symmetric plane. Another symmetric plane of tire exists, so only half of the tire is meshed. The half pipe has a rectangular cross-section with an area of $0.0025m \times 0.005m$. The length is $0.1m$. It has an open end and a closed end which has unity velocity as boundary condition. The base surface behind the piston is modelled as flat to reduce the elements. It has a very small impedance which is used to minimize the reflections. Other parts of the model are rigid.

The acoustic pressure at the central node of the closed end is calculated by Samray. The acoustic velocity is unity, so the impedance of the piston is obtained. Then the radiation impedance is calculated from this impedance by equation (3.2).

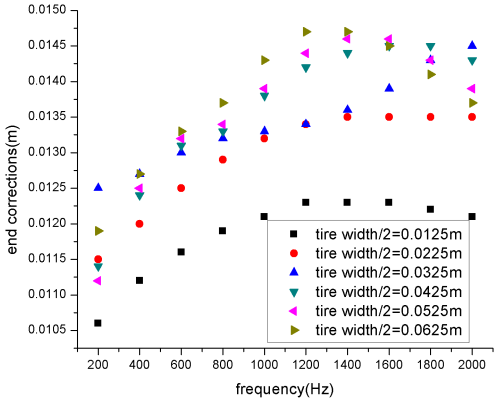

Figure 3.7: End corrections of a longitudinal pipe with tire flanges of different widths within $2000Hz$

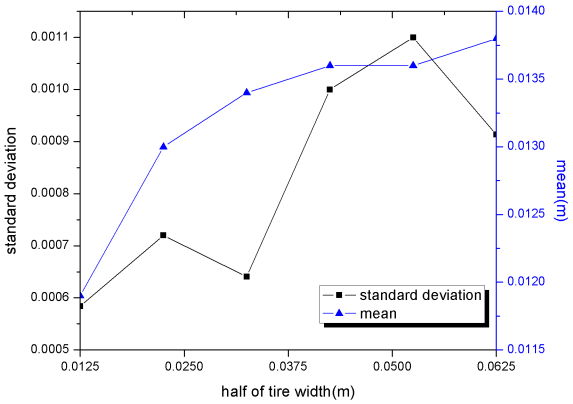

Figure 3.8: Standard deviations and mean values of end corrections of a longitudinal pipe with tire flanges of different widths

The end corrections of the longitudinal pipe for tires of different widths are shown in Fig.3.7, and the frequency interval is $200Hz$. The tire radius is $0.27m$. For each tire width, the end corrections are frequency-dependent, but their standard deviations are very small (see in Fig.3.8), which indicates that they tend to be very close to the mean values. The standard deviation is calculated by equation (3.4). So the mean values of end corrections for each tire width in Fig.3.8 are used to get a fit formula of end corrections (3.6), in which w is half of tire width.

$$\delta = 0.00936 + 0.26929w - 5.77679w^2 + 41.66667w^3 \tag{3.6}$$

The same procedure can be used to get fit formulas for other pipes and tires of different dimensions.

3.2 Resonant frequencies

In the network, there are columns of air. Waves traveling in air will reflect back when they reach the end. A standing wave is created at the network's resonant frequency.

An open network will resonate if there is an anti-node at each open end. These anti-nodes are places where there are maximum velocities and minimum pressures ($p = 0$). However, these zero pressures are not at the physical ends of the network as they are altered by their contacts with air. In fact they are at the end correction positions of the network.

Knowing the resonant frequencies of the network is essential. The network has a great influence on the exterior acoustic field of the tire around the resonant frequencies, and at other frequencies there is no change of acoustic pressure. In order to calculate this influence the resonant frequencies should be estimated first, otherwise all the frequencies should be calculated and it leads to large computations.

There are analytical solutions for simple pipes such as a straight pipe, a T-shaped pipe and so on. However, numerical methods should be adopted in order to get the resonant frequencies of complex networks.

It is assumed that there is a plane wave in the straight parts of the network for the cross-sections are quite small compared to the wavelengths.

3.2.1 Analytical methods

3.2.1.1 Solutions of plane wave

The resonant frequencies of a straight pipe are easy to get. The acoustic pressure solution of the wave equation in a straight pipe is

$$p(z) = acoskz + bsinkz \tag{3.7}$$

with $k = \omega/c$ the wave number, c the speed of sound, $\omega = 2\pi f$, a, b constants and z the longitudinal coordinate of the pipe.

If coordinates z of the physical pipe ends are δ and $l + \delta$, at $z = 0$ and $z = L$ ($L = l + 2\delta$) the pressures should be zero because of the pipe resonances. δ is the end correction and l is the physical length of the straight pipe.

One has $p(0) = 0$, so $a = 0$ in (3.7). And then from $p(L) = 0$, one has $b\sin(kL) = 0$. Thus, the resonant frequencies are

$$f = \frac{nc}{2L} \tag{3.8}$$

where n is a positive integer (1, 2, 3...).

3.2.1.2 Merkli's method

A theoretical model was given by Miles [2] to calculate the pressure and velocity in a T-shaped pipe based on the transmission line and impedance analogy circuit. However, it cannot be used to estimate the resonant frequencies. Merkli [52] proposed a simple model to calculate the resonant frequencies of a T-shaped resonator by using the wave propagation theory. It will be introduced for a T-shaped pipe with three open ends.

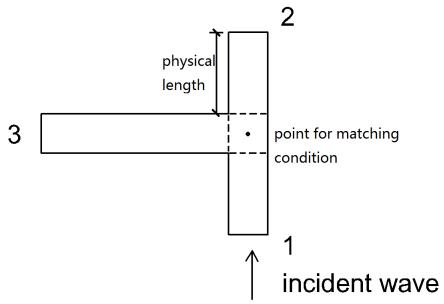

Figure 3.9: T-shaped pipe

For the T-shaped pipe of Fig.3.9, in three branches there are plane waves. The incident wave enters from end 1. The boundary conditions at the junction are that the pressure is single valued,

$$p_{j1} = p_{j2} = p_{j3} \tag{3.9}$$

and that the continuity equation holds

$$v_{j1}\rho S_1 = v_{j2}\rho S_2 + v_j 3\rho S_3 \tag{3.10}$$

where v is acoustic velocity, ρ is density, S is the branch cross-section area and j represents the junction. The three branches have the same S. In terms of the impedance,

$Z = p/v$, (3.9) and (3.10) can be combined to give

$$\frac{1}{Z_{j1}} = \frac{1}{Z_{j2}} + \frac{1}{Z_{j3}} \tag{3.11}$$

For the open ends of the T-shaped pipe, impedances Z_o are zero at the end correction positions at the resonant frequencies. So the impedances at the junctions can be obtained by equation (3.2), in which Z_r is replaced by Z_o and Z_l gives the impedances at the junction. Then equation (3.11) becomes a relation of resonant frequencies. After solving this new equation the resonant frequencies can be obtained. More details can be seen in Merkli's paper [52].

In this model, end corrections for open ends should be considered. Besides, the end correction of each branch at the junction position is also essential. Because the matching condition (3.11) is 'at the junction', but it is hard to say precisely at which point the boundary condition has to be met. The distance from the point of matching condition to the closest physical end is the end correction at the junction position. The position of the point of matching condition should be determined. Merkli used a weighted partition of the common intersection volume of the junction based on the branch lengths, and a transformation of the transition volumes between the junction and each branch. So for each open branch, the effective length includes the physical length of the branch, the end correction at the junction position and the end correction of the open end. In order to determine effective lengths of the branches of T-shaped resonators and get more precise resonant frequencies, Deyu Li [91] compared Merkli's end corrections, hybrid Rayleigh's end corrections [92], simplified impedance models and alternate simplified impedance models with measured results for the case where the three branches have the same circular cross-sections. In his paper [53] published later a new model based on Rayleigh's end corrections was proposed for the same case. But his experimental results showed that this model also works for square cross-sections of branch 1 and 2.

The previous researches are about the T-shaped acoustic resonators which have closed ends, but the T-shaped pipe in this work has three open ends. Merkli's model will be adopted for the estimation of the resonant frequencies, but the end corrections will be calculated by other methods. Dalmont's [3] methods and results will be used for the calculations of the open end corrections. With his methods, the open end flanges could have any shape and dimension. Then the end corrections at the junction position should be obtained, and end corrections similar to the ones from model 1 by Li [53] could be used. In the model 1 by Li [53], first Rayleigh's end correction (3.12) is used for the interior end correction of each branch of the T pipe in Fig.3.9. Then the interior end correction of branch 3 is divided equally and combined into the end

corrections of branch 1 and branch 2. So no interior end correction is used for branch 3, and $1.5\Delta L$ is the interior end correction for branch 1 and 2. Li [53] compared this model 1 and other models with measurements, and found that this model is the best one.

$$\Delta L = \frac{8}{3\pi} r \tag{3.12}$$

In the model 1 in [53] the pipe has a circle cross-section and r is the radius.

3.2.2 Numerical methods

Theoretically, Merkli's model can be applied to other cases such as a L-shaped junction pipe, cross junction pipe or a network. However, when estimating the resonant frequencies the end corrections of branches at the junction positions should be obtained first. There is no precise result. In order to avoid calculating these interior corrections, numerical methods can be adopted.

3.2.2.1 Finite element methods

The resonant frequencies can be obtained by solving an eigenvalue problem (3.13) of an undamped finite element model.

$$(K - \omega^2 M)\phi = 0 \tag{3.13}$$

K is the stiffness matrix, M is the mass matrix, $\omega = 2\pi f$ and ϕ is the eigenvector.

Finite element software Abaqus is chosen to perform the resonant frequencies extraction procedure, which is a linear perturbation procedure. The networks have open ends. The impedance boundary conditions cannot be applied to these ends in Abaqus. So their end corrections should be taken into account in the models. The branches with open ends in finite element models are created a little longer than their physical lengths. Since at the resonant frequencies the pressures are zero at the end correction positions, zero pressure boundary conditions are used. The other boundary conditions are rigid.

For a 2D network whose junctions and branches are in the same plane, an automatic calculation procedure can be implemented to get the resonant frequencies. Abaqus GUI will generate an input file '*.inp' which is sent to the processor while running a simulation. A simple case of a straight pipe is solved to get the '*.inp' file which can be modified for complex networks. In this file, the straight pipe mesh information is deleted, then mesh information of the network to be solved is added. New node and element sets are defined for the zero pressure boundary conditions. The other parts of this file keep the same data as before.

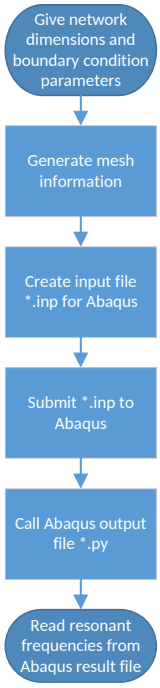

Figure 3.10: Flow chart of Matlab program 2DNRF for calculating network resonant frequencies

Since 2D meshes are quite easy to get, Matlab is used to create the mesh information for the network, and the node and element sets for the boundary conditions. The other information from the old file of straight pipe is written into the new '*.inp' file by Matlab as well.

Abaqus scripting is a powerful tool for combining the functionality of the GUI of Abaqus and the power of the programming language Python. After finishing the actions such as open the Abaqus result file '*.odb' and output the results needed, a script file '*.rpy' will be created including these actions. Then the file '*.rpy' should be renamed as '*.py' which can be submitted directly to Abaqus by commands in order to output the results needed. The results will be saved in a text file.

The automatic procedure for calculating the resonant frequencies of 2D network is: create the '*.inp' by Matlab, submit it to Abaqus by commands in Matlab, and then call Abaqus output script '*.py' in Matlab. This Matlab programme is named as '2DNRF'.

3.2.2.2 Boundary element methods

Boundary element methods will be only used to check the resonant frequencies obtained by analytical methods and FEM. At the resonant frequencies, the pressures at

the physical ends are very small compared to the pressures inside the pipes, but they are much larger than the pressures at other frequencies. By comparing the pressures at open ends at different frequencies and observing the acoustic fields of the pipes, resonant frequencies can be found.

3.3 Examples of resonant frequencies

3.3.1 T pipe

The body of flanges in this example is a hexahedron. There is a T pipe with three open ends at the center (see Fig.2.7). The flange and pipe walls are rigid. The half-width of the square pipe is $a_{sq} = 0.01m$. The cross section of the square flange parallel to x-y plane is $0.3 \times 0.3m$. The branch lengths are $l_1 = l_2 = 0.04m$ and $l_3 = 0.14m$. The three methods introduced above are used to calculate the resonance frequencies of this T pipe.

In analytical methods and FEM, Dalmont's open end corrections (3.14) for square flange and square pipe are used.

$$\delta_{sq} = \delta_{sq\infty} + \frac{a_{sq}}{b_{sq}}(\delta_{sq0} - \delta_{sq\infty}) + 0.057\frac{a_{sq}}{b_{sq}}[1 - (\frac{a_{sq}}{b_{sq}})^5]a_{eff} \tag{3.14}$$

with $\delta_{sq\infty} = 0.811a_{eff}$ and $\delta_{sq0} = 0.597a_{eff}$, in which $a_{eff} = 2a_{sq}/\sqrt{\pi}$. Here, $2a_{sq}$ and $2b_{sq}$ are pipe width and flange width, respectively.

Dalmont's fit formula (3.14) is for square flanges, but the flange $0.1 \times 0.3m$ parallel to y-z plane is not square. Here, the shorter width $0.1m$ will be used as $2b_{sq}$ in the fit formula (3.14) to get the approximate end correction for end 3. Since the flanges $0.3 \times 0.3m$ parallel to x-y plane are square, there is no such problem for ends 1 and 2 and equation (3.14) can be used directly to calculate their end corrections. Thus, the open end corrections for branches $1, 2$ and 3 are $\Delta L_{11} = \Delta L_{21} = 0.009m$ and $\Delta L_{31} = 0.0088m$, respectively, where the subscripts mean the pipe number.

In the analytical methods, for the interior end corrections of each branch at the junction position, the end corrections similar to the ones (introduced in 3.2.1.2) of model 1 in [53] will be used. But the pipe cross-sections here are square, so $\delta_{sq\infty} = 0.811a_{eff}$ is used instead of equation (3.12) according to the relation of area between circles and squares. Thus, for branch 3 no interior end correction will be used, and for branch 1 and 2 the interior end corrections are

$$\Delta L_{12} = \Delta L_{22} = 1.5\delta_{sq\infty} \tag{3.15}$$

The effective lengths of the three branches are

$$L_1 = l_1 + \Delta L_{11} + \Delta L_{12} \tag{3.16}$$

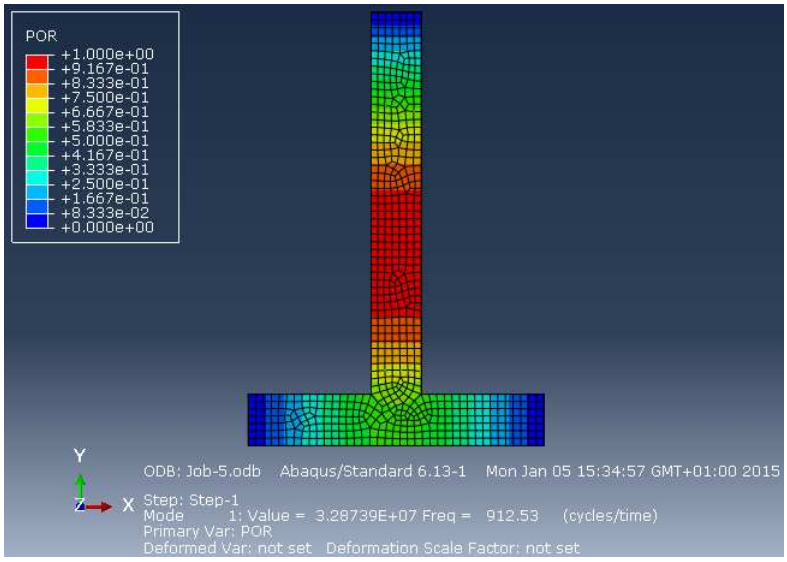

(a)

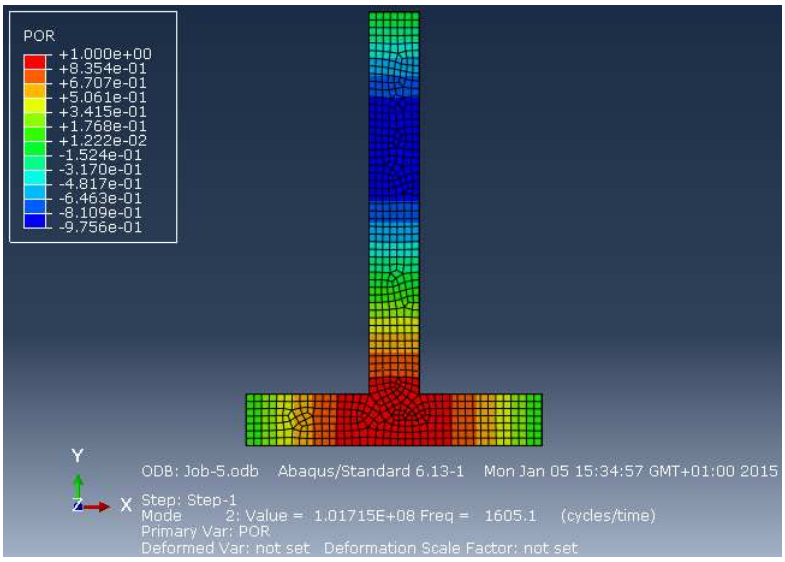

(b)

Figure 3.11: Modes of T pipe within 2000 Hz obtained from Abaqus by 2DNRF: (a) The first resonant frequency $912Hz$; (b) The second resonant frequency $1605Hz$.

$$L_2 = l_2 + \Delta L_{21} + \Delta L_{22} \tag{3.17}$$

$$L_3 = l_3 + \Delta L_{31} \tag{3.18}$$

Then by using Mercli's model introduced in 3.2.1.2, three resonant frequencies are obtained: $897Hz, 1153Hz$ and $1567Hz$.

The T pipe can be considered as two dimensional, so it can be solved by '2DNRF' introduced before, which is a Matlab programme for estimating the resonant fre-

quencies of 2D network by FEM. The open end corrections should be taken into account when inputting the pipe coordinates in '2DNRF'. The coordinates of zero pressure boundary conditions should be given in '2DNRF' as well. After running it, the resonant frequencies are obtained. In Fig.3.11a and 3.11b, there are two resonant frequencies within $2000Hz$.

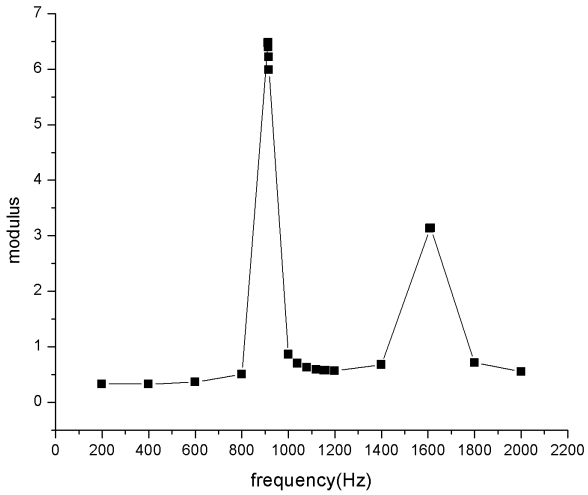

Figure 3.12: Total pressure modulus at the open end of branch 3

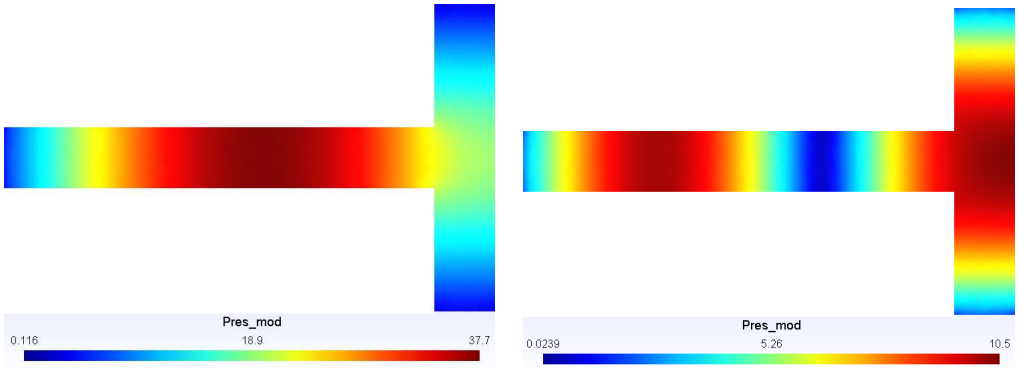

(a) (b)

Figure 3.13: Total pressure modulus distributions on the T pipe surface at resonant frequencies within $2000Hz$ by BEM: (a) The first resonant frequency $914Hz$; (b) The second resonant frequency $1610Hz$.

The boundary of the structure can be meshed with 2D elements and then solved by boundary element software Samray in order to get the acoustic field of the T pipe. The source S is at $(0, 0, -0.1)$. Pressure modulus at open end of branch 3 by BEM is shown in Fig.3.12. At the resonant frequencies $914Hz$ and $1610Hz$, there are two

pressure peaks. The distributions of total pressure can be seen in Fig.3.13a and 3.13b, and the variations of pressure with the coordinates are the same as in Fig.3.11a and 3.11b.

Table 3.1: The resonant frequencies of flanged T pipe

Estimation methods	Analytical	2DNRF	BEM
`First frequency`	$897Hz$	$912Hz$	$914Hz$
`Second frequency`	$1567Hz$	$1605Hz$	$1610Hz$

In table 3.1, the results of FEM and BEM are very close, which means that the end corrections of open ends are adequate. The differences between analytical and numerical results show that the interior end corrections at the junction position need to be further developed. So the analytical methods are not suitable for complex networks. By comparison of the three methods, the FEM '2DNRF' introduced before is suitable for estimating the resonant frequencies of T-shaped pipes.

3.3.2 Networks

A network (in Fig.2.10b) in the contact zone between a round surface and a rigid plane surface is solved in this part in order to validate the estimations of end corrections and the software '2DNRF' which is programmed to calculate the resonant frequencies. The radius of the round structure is $0.27m$ and its width is $0.15m$. In the network, there are two longitudinal (x direction in Fig.2.10b) and three transverse branches (y direction). The network has two symmetric planes xz and yz. The plane surface is in the plane xy.

In order to estimate the resonant frequencies by program '2DNRF', the corrections of network open ends should be taken into account.

All the longitudinal ends have the same corrections, for their flanges are of the same dimensions. These corrections can be calculated by the methods introduced in 3.1.2. Although the results in 3.1.3 are for the case where ends are in the middle of width, in the interest of simplicity they will be used directly for the longitudinal ends in this network. The distances between the longitudinal end 1 and the sides AB or CD of the contact zone are not the same. The shorter distance is used in the fit formulas in 3.1.3 to get the end correction.

The end corrections of transverse branches are obtained by equation (3.14), where b_{sq} is the shorter one of the two distances between the transverse end and the sides AD or BC of the contact zone. Since the rigid road is a symmetric plane, the transverse ends are not square. In equation (3.14), $2a_{sq}$ should be the side of a square end. So

the transverse ends should be transformed into squares according to the equality of end areas.

3.3.2.1 Flange of cylinder

In this section, the round surface in Fig.2.10a is a cylinder whose surface is flat in the contact zone between the cylinder and the rigid plane surface. The pipe width is $0.009m$. Since the rigid plane surface is a symmetric plane, the cross-sections of network ends are $0.009m \times 0.018m$, and a_{sq} in (3.14) is given by $\sqrt{0.009 \times 0.018}/2$. By (3.14) the end corrections for ends 2 and 3 are $0.0057m$ and $0.0054m$, respectively.

The shorter distance (from the end 1 to side AB or CD) $0.0425m$ is used to get the end correction of end 1 by equation (3.5). The longitudinal end correction is $0.012m$ by equation (3.5).

By solving with '2DNRF', two resonant frequencies are found within $2000Hz$: $1232Hz$ and $1823Hz$. The modes can be seen in Fig.3.14a and 3.14b.

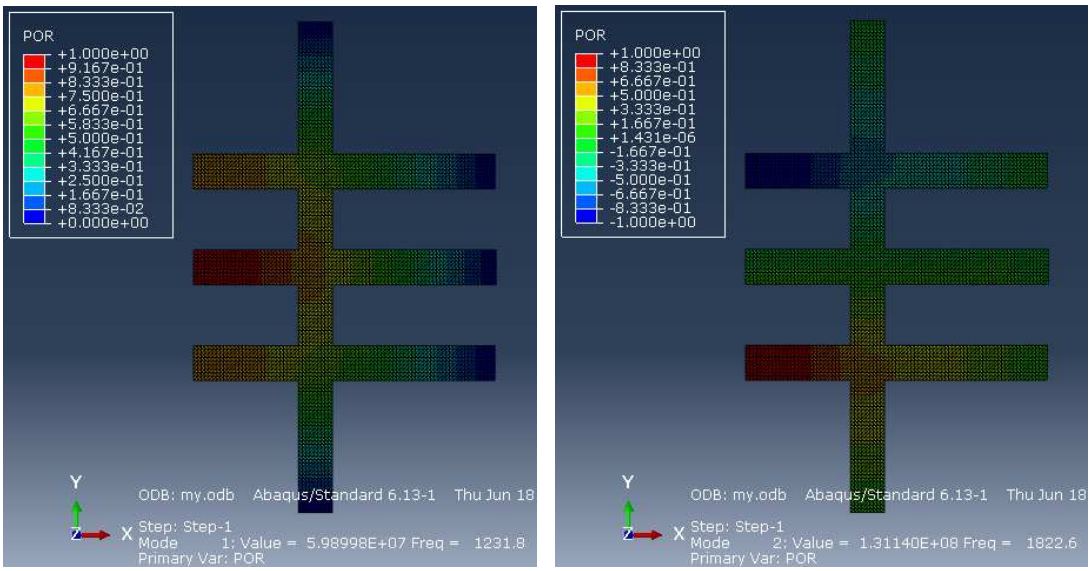

(a) (b)

Figure 3.14: Modes of half network within 2000 Hz: (a) The first resonant frequency $1232Hz$; (b) The second resonant frequency $1823Hz$.

Since the cylinder has a symmetric plane xz, half of the cylinder without network is meshed with 2D elements. Then this problem is solved by the method 'A2BEM' proposed in this work. The source is at $(0.1, 0, 0.005)$. The pressure at end 2 is shown in Fig.3.15. The resonant frequencies are $1230Hz$ and $1825Hz$.

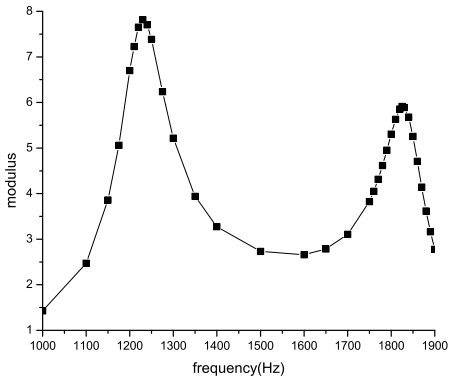

Figure 3.15: Total pressure modulus at the open end 2

Table 3.2: The resonant frequencies of a network with cylindrical flange

Estimation methods	**2DNRF**	**A2BEM**	**Error**
`First frequency`	$1232Hz$	$1230Hz$	$2Hz$
`Second frequency`	$1823Hz$	$1825Hz$	$2Hz$

In table 3.2, the errors of resonant frequencies between these two methods are quite small. The resonant frequencies are validated by measurements in chapter 5.

3.3.2.2 Flange of tire

In this section, the round surface in Fig.2.10a is a tire, and the rigid plane surface is a surface of road. The pipe width is $0.005m$. Since the road is a symmetric plane, the cross-sections of network ends are $0.005m \times 0.01m$, and a_{sq} in (3.14) is given by $\sqrt{0.005 \times 0.01}/2$. By (3.14) the end corrections for ends 2 and 3 are $0.0032m$ and $0.0031m$, respectively.

The shorter distance (from the end 1 to side AB or CD) $0.0425m$ is used to get the end correction of end 1 by equation (3.6). The longitudinal end correction is $0.01357m$ by equation (3.6).

By solving with '2DNRF', two resonant frequencies are found within $2000Hz$: $1224Hz$ and $1770Hz$. The modes can be seen in Fig.3.16a and 3.16b.

Since the tire has a symmetric plane xz, half of the tire without network is meshed with 2D elements, and then half of the network is meshed with Abaqus. Then this problem is solved by the method 'BFEM' proposed in this work. The source is at $(0.1, 0, 0.005)$. The pressure at end 2 is shown in Fig.3.17. The resonant frequencies are $1213Hz$ and $1771Hz$. The pressure distributions are shown in Fig.3.18a and 3.18b. By comparisons with Fig.3.16a and 3.16b, similar pressure distributions can be seen.

In table 3.3, the errors of resonant frequencies between these two methods are

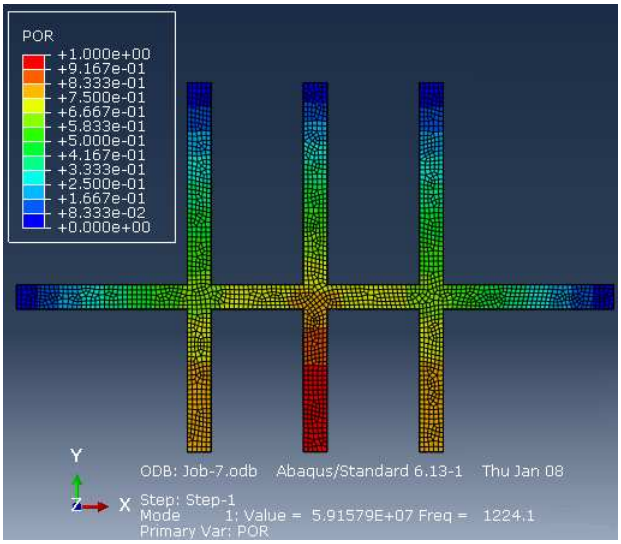

(a)

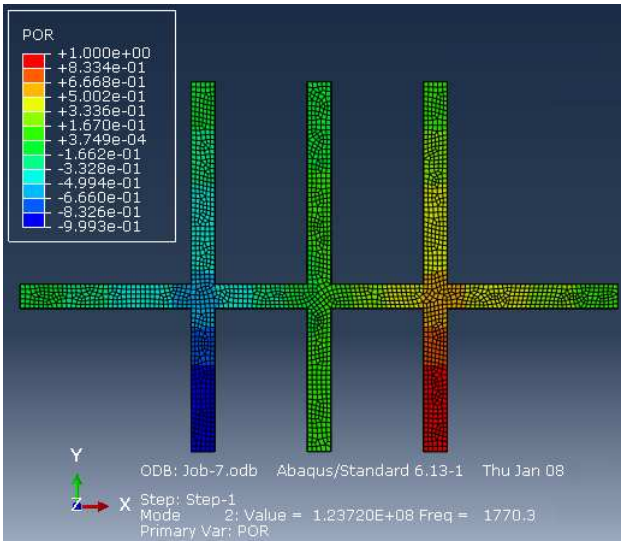

(b)

Figure 3.16: Modes of half network within 2000 Hz obtained from Abaqus by 2DNRF: (a) The first resonant frequency $1224Hz$; (b) The second resonant frequency $1770Hz$.

Table 3.3: The resonant frequencies of a network with tire flange

Estimation methods	**2DNRF**	**BFEM**	**Error**
`First frequency`	$1224Hz$	$1213Hz$	$11Hz$
`Second frequency`	$1770Hz$	$1771Hz$	$1Hz$

quite small. Since '2DNRF' is easy to use and suitable for automatic estimations of different networks, it will be used in the following analyses.

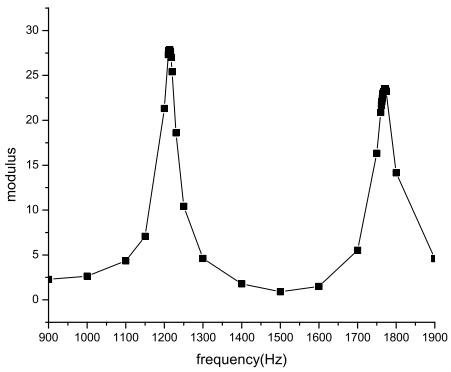

Figure 3.17: Total pressure modulus at the open end 2

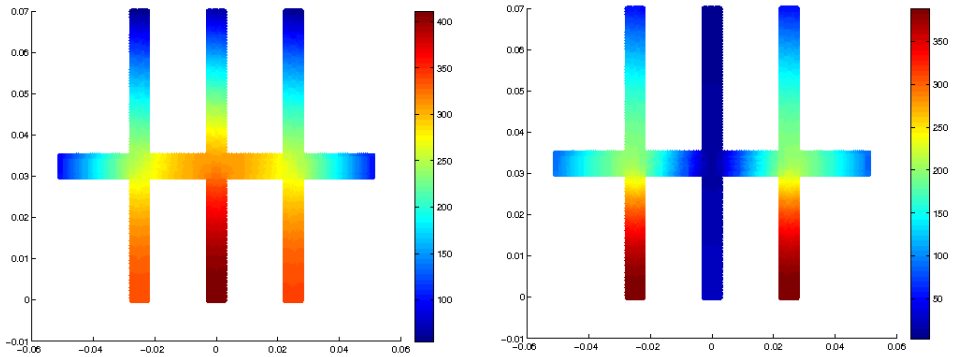

(a) (b)

Figure 3.18: Total pressure modulus distributions of a half network at resonant frequencies within 2000 Hz by BFEM: (a) The first resonant frequency 1213Hz; (b) The second resonant frequency 1771Hz.

If we ignore the end corrections of all the open ends, the resonant frequencies calculated by '2DNRF' are 1379Hz and 1934Hz which are quite different from the results in table 3.3. Because for the tire flange the end corrections are very large compared with the original network dimension and must be taken into account in the estimation of the resonant frequencies.

3.4 Conclusions

In this chapter, previous researches about end corrections of pipe open ends are summarized. Boundary element methods are validated with a simple example by comparing with existing fit formula, and then used to calculate the open end corrections for ends with arbitrary shaped flanges. For given pipe dimensions, end corrections depend on the shape and dimensions of flange, and also vary with frequencies. However for

given flange dimensions, mean values of end corrections at different frequencies can be used approximately as the end correction within $2000Hz$, because the standard deviation of end corrections at different frequencies is small. Thus, a fit formula of end corrections for different flange dimensions can be obtained.

For simple pipes, analytical calculation methods of resonant frequencies are introduced. For complex 2D networks finite element methods are used as it is not easy to get accurate values of interior end corrections at junction positions. Matlab codes '2DNRF' based on the finite element methods are developed to calculate the 2D network resonant frequencies automatically. Once the network dimensions are given and the open end corrections are known, the resonant frequencies can be obtained by '2DNRF'. This method is compared with analytical methods and boundary element methods for T pipes, and also compared with another numerical methods 'BFEM' and 'A2BEM', which are introduced in this work, for a complex network. Good agreements can be seen.

The methods introduced in this chapter make it possible to get the resonant frequencies for 2D networks with perpendicular pipes and arbitrary shaped flanges.

Chapter 4

Optimization of junctions and end positions of 2D networks

Around the resonant frequencies of a network, pressure reductions could be found in the exterior subdomain of horn-like structures. The value and number of resonant frequencies vary according to the network structures. Because of this dependence, it should be possible to find the wanted resonant frequencies or a maximum number of resonant frequencies by optimizing the network structure.

The parameters that describe a network are the number and positions of ends, junction types, junction positions and pipe cross-sections. In this work there are only longitudinal and transverse pipes in a network, so the junction positions depend on the end positions. If the end positions are known, the junction positions are known. The 2D network considered here consists of the three types of junctions shown in Fig.4.1a-4.1c.

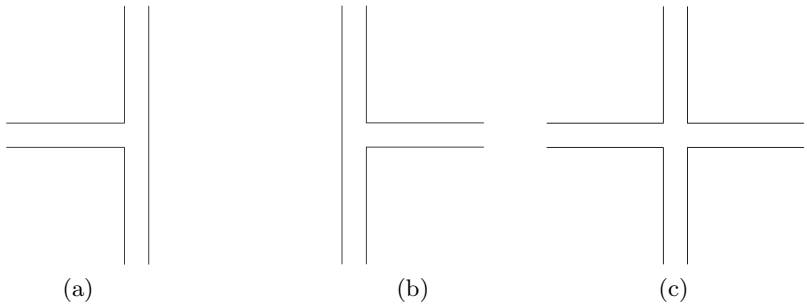

Figure 4.1: (a) T junction with left branch; (b) T junction with right branch; (c) Cross junction

Different networks can be formed by using different parameters. Their resonant frequencies can be estimated by the finite element method 2DNRF proposed before.

By changing the parameters, networks with the wanted resonant frequencies or a maximum number of resonant frequencies can be found. Optimization methods should be adopted to achieve this purpose.

First the optimization methods will be reviewed in this part, and then the appropriate one will be used to optimize and design 2D network structures.

4.1 Genetic algorithm

In order to get the wanted frequencies or a maximum number of resonant frequencies, networks need to be optimized and designed by a optimization method. Genetic algorithm (GA) is used for this purpose. The Genetic Algorithm Toolbox for MATLAB developed by the University of Sheffield is chosen for the optimization.

4.1.1 Population Representation

The chromosome representations should be decided first. GAs operate on a number of potential solutions, called a population of chromosomes, consisting of some encoding of the network parameter set. The binary and integer chromosome representations are supported by the GA Toolbox. For a network, each parameter of junction type is encoded as an integer in $0, 1$ or 2 which represent the junction types in Fig.4.1a-4.1c, and the other parameters of network dimensions (such as end positions, cross-sections and so on) are encoded as binary strings.

Then the initial population can be generated by using a random number generator. There are two parts in a population, a binary part of network dimensions and an integer part of junction types. The Toolbox function, *crtbp*, can be used to initialise binary and integer parts. This function can create a random binary matrix of size $Nind \times Lind$ for the parameters of network dimensions, where $Nind$ specifies the number of individuals and $Lind$ the length of the individuals. For the parameters of junction types, *crtbp* can give a integer ($0, 1$ and 2) matrix of size $Nind \times Lind^{jun}$ where $Lind^{jun}$ is the number of junctions. By combining these two matrices, the initial population is obtained.

Here is an example of an individual in a population of networks

$$[\overbrace{0100...1111, \underbrace{0101...0101}_{l}, ..., 0101....0111}^{m}, \overbrace{2, 1, 0, ..., 1, 0, 2}^{n}] \quad network\ i \tag{4.1}$$

This is the chromosome representation of the network in Fig.4.2. The network has 3 rows and 4 columns. In the first part of the chromosome, there are m dimension parameters and each one has l binary strings which can be converted to a real value by the routine $bs2rv$. So there are m real values, and for this network m is 8. We

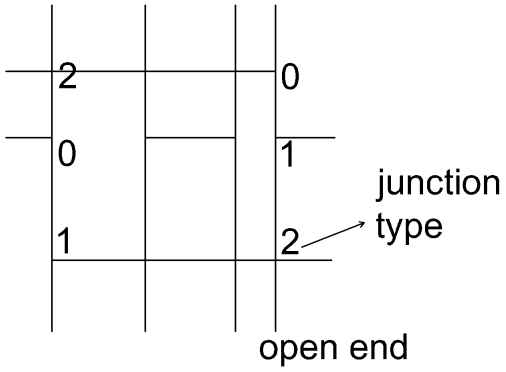

Figure 4.2: An example of network for the chromosome representation

specify the boundary of the network, so the open ends move only on this boundary and along with the junctions. Therefore, we only need to generate the real values for the coordinates of the junctions and the cross sectional area of the network. Since we use the same cross section for the network, only one real value is needed for the area. The other seven real values represent the positions of the three rows and four columns which determine the coordinates of the junctions. In addition, the end corrections of the open ends also depend on the positions of the rows and the columns in the fit formula of end corrections (for example equation (3.6)), so no real value is needed for the end corrections. In the second part of the individual there $n = 12$ junctions and each integer represents the junction type. If this population consists of k networks, its chromosome representation is a $k \times (m + n)$ matrix.

4.1.2 The objective and fitness functions

The purpose of this work is to find the wanted resonant frequencies or as many resonant frequencies as possible by designing and optimizing the network. The 2D FEM, implemented in the MATLAB code '2DNRF' proposed before, has been used for estimating values of f_r and the number of resonant frequencies of a network.

If f_w is the wanted resonant frequency and there are several resonant frequencies for the network i, the objective function for the first purpose is given by

$$ObjV_1(x_i) = min(|f_{r1} - f_w|, |f_{r2} - f_w|, ...) \tag{4.2}$$

where x_i is the chromosome of network i.

If the purpose is to find as many resonant frequencies as possible, the objective function is the number of the resonant frequencies. Since the GA Toolbox is for minimization problems, a minus sign is added. One has

$$ObjV_2(x_i) = -count(f_{r1}, f_{r2}, ...) \tag{4.3}$$

We would like to minimize the two objective functions, which only depends on the parameters of the network, that is its dimensions and junction types.

For the minimization problem, the most fit individuals have the lowest numerical values of the associated objective function. The raw objective values in equation (4.2) or (4.3) are usually only used as an intermediate stage in determining the relative performance of individuals. The fitness function is normally used to transform the objective function value into a measure of relative fitness. To prevent premature convergence, Baker [93] suggests limiting the reproductive range, so that no individual generate an excessive number of offspring. Here, individuals are assigned a fitness according to the rank of their raw objective values in the population rather than the raw performance.

A vector of fitness of the chromosome is obtained by a linear model as equation (4.4). The order of this vector reflects the order of the original objective vector.

$$FitnV(Pos) = 2 - SP + 2 \times (SP - 1) \times (Pos - 1)/(Nind - 1) \tag{4.4}$$

where the selective pressure SP is the chosen maximum fitness value in the population and is set to 2, Pos is the position in the list of objective values of the chromosomes sorted in descending order, and $Nind$ is the number of individuals in the population. More details about equation (4.4) can be seen in the documentation of Sheffield GAToolbox or [93].

4.1.3 Selection

The selection algorithm selects individuals for reproduction based on their relative fitness. It determines the number of times an individual is chosen. There are two steps in the selection process: the first one is to transform the raw objective values into a relative fitness, and the second one is to convert the relative fitness into a discrete number of offspring. The first step is done with the fitness function in section 4.1.2. The second step, sampling, is the probabilistic selection of individuals for reproduction based on the relative fitness.

Roulette wheel mechanism is used by many selection techniques. Here, the circumference of the roulette wheel is determined as the sum of the individuals' relative fitness values in the current population. The size of each individual interval in the roulette wheel depends on the relative fitness value. Stochastic sampling with replacement (SSR) is the basic roulette wheel selection method. Individual are placed in order into contiguous intervals in the roulette wheel. It uses only one pointer to select an individual. In the range $[0, Sum]$, a random number indicated by an arrow in Fig.4.3a is generated. The individual whose segment spans the random number

is selected and in Fig.4.3a the selected individual is the second one. The required number of individuals can be selected by repeating this process. The segment sizes don't change in the whole process.

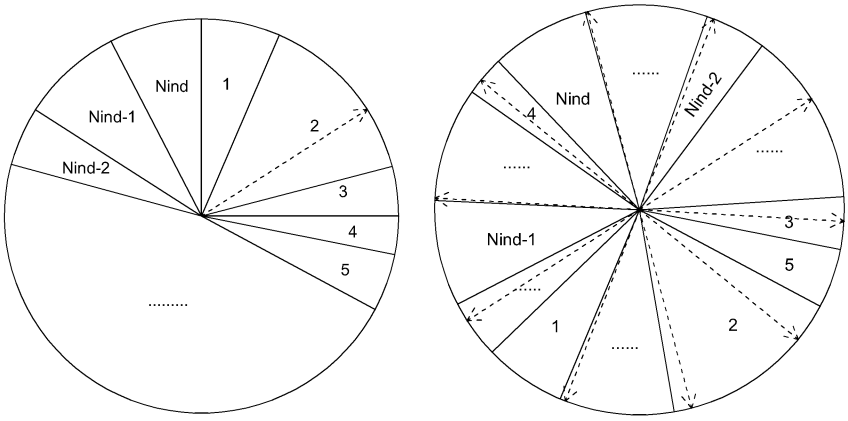

Figure 4.3: (a) Stochastic sampling with replacement (SSR) with one pointer; (b) Stochastic universal sampling (SUS) with ten pointers.

Stochastic universal sampling (SUS) is a little different. The individuals are shuffled randomly. It uses N equally spaced pointers, where N is the number of individuals required. N individuals can be selected simultaneously. In the whole process only a single random number, ptr, in the range $[0, Sum/N]$ is generated. The N pointers are created by a space Sum/N, $[ptr, ptr + Sum/N, ..., ptr + (N-1) \times Sum/N]$. The individuals whose relative fitnesses span the pointers are selected and the number of pointers inside the segment of an individual indicates the times this individual is chosen. In Fig.4.3b an example is shown. There are ten pointers, and individual 2 is selected twice for there are two pointers inside this segment.

When an individual has a really large relative fitness, SSR can have bad performance. However, SUS starts from a small random value ptr, and gives chances to other individuals to be selected. Besides, SUS has high efficiency. So SUS will be used in this work.

The number of selected individuals required can be given by a parameter named generation gap. It is the fraction between the number of the selected individuals and the original population size. Normally it is no more than one.

4.1.4 Crossover(Recombination)

Crossover is a basic operator for producing new chromosomes that have some parts of both parent's genes selected by the selection operator. Single-point crossover is

the simplest approach and will be used in this work. The individuals are combined into pairs whose genetic information are exchanged to produce new individuals. The number of population should be given as even. The single-point crossover selects a random integer position k between 1 and $L-1$, where L is the length of the individual. The variables from position $k+1$ to L are exchanged between the two parent individuals. For example, in Fig.4.4 if the crossover position is $k=3$, the parents has new offsprings

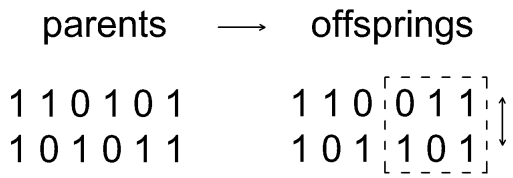

Figure 4.4: Single-point crossover

4.1.5 Mutation

Mutation is a random process for producing new genetic structures. It replaces one allele of a gene by another. The mutation process mutates each individual with a given probability P_m. This process guarantees that any individual has a chance to be searched in case a good genetic material may be lost through the selection and crossover processes.

For a binary population of dimension parameters of the network, the mutation of the gene is within two binaries 0 and 1. For a population of junction types of the network, the gene mutates within three integers 0, 1 and 2 representing three types of junction. In the chromosome of the network in equation (4.1), there are two parts, the dimension parameters and the junction types. The mutation is carried out separately for each part, and then the mutated parts are assembled together.

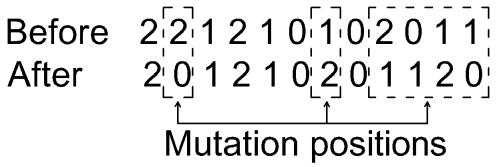

Figure 4.5: Multi-point mutation of an integer individual

Here is an example of mutation of an integer individual in Fig.4.5. Integer mutation changes the value at the location selected as the mutation point within the given integer range $0, 1$ and 2. Mutation is generally applied uniformly to the whole popu-

lation, so an individual may be mutated at more than one point. For the mutation of a binary individual, the process is similar. The value of the bit at the loci selected as the mutation point changes within 0 and 1.

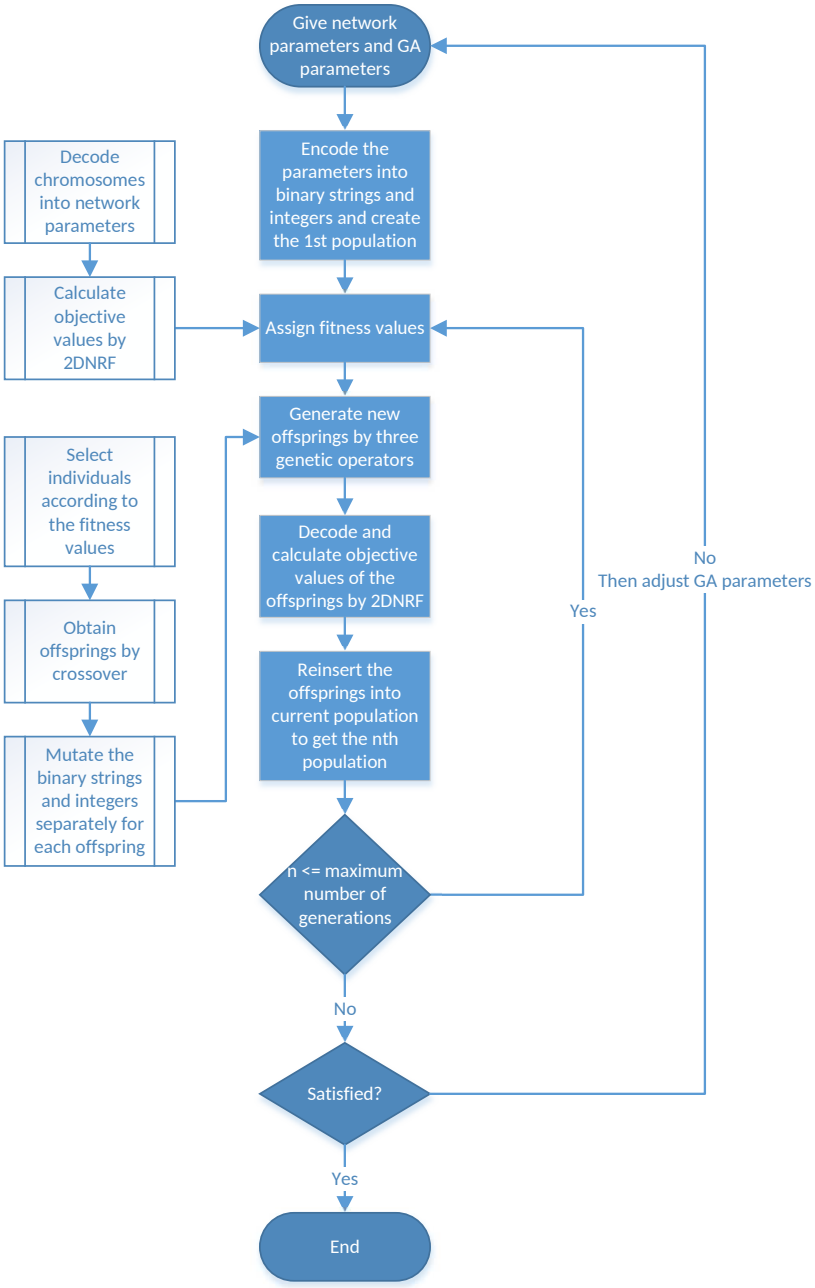

Figure 4.6: Flow chart of GA process

4.1.6 Reinsertion

A new population is produced by the operators above and the new individuals have to be reinserted into the old population to maintain the size of the old population. First the fitness of the new individuals should be determined. Then the least fit members in the old population are replaced by offsprings selected according to their fitness.

4.1.7 Termination of the GA

When GA is terminated, the homogeneity of the fitness values of individuals should be considered. It is difficult to formally specify a convergence criteria because the GA is a stochastic search method. A common practice is to give the number of generations for running GA and then test the best individual. If it is not acceptable, the GA process should be restarted or a new search should be initiated.

The flow process of GA is shown in Fig.4.6.

4.2 Optimizations and designs of 2D networks

In order to illustrate that GA works for the optimization of 2D networks and the resonant frequencies needed can be obtained by the GA process, some examples are given in the following.

The network to be optimized in this section has 14 open ends and 12 junctions. The junction positions are arranged in four columns and three rows, and their coordinates depend on end coordinates. In Fig.4.7 there is an example of the networks generated randomly in the first generation of GA procedure. In Fig.4.7 we can see 14 positions for the open ends, but the network has 12 open ends due to the junction types. The circles represent the junction positions. Three types of junctions introduced at the beginning of this chapter can be seen in this example. They are T junction with left branch, T junction with right branch and cross junction.

The corrections of open ends can be obtained by the methods introduced in chapter 3. If the ends are closed, there is no need to add the end corrections to the origin pipe lengths. All the dimension parameters of the network can be optimized within given ranges during the GA process, but for the sake of simplicity some of them are specified.

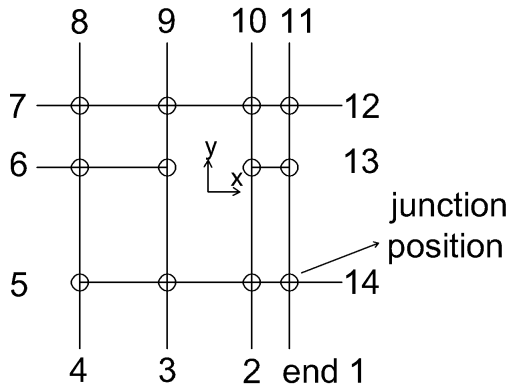

Figure 4.7: An example of the networks generated randomly in the first generation of GA procedure

4.2.1 Unflanged networks

4.2.1.1 Dimension parameters of networks

In this example there is no flange, so the end corrections, $0.001684m$, can be calculated by equation (4.5) which is from paper [3].

$$\delta_{sq0} = 0.597 a_{eff} \tag{4.5}$$

with $a_{eff} = 2a_{sq}/\sqrt{\pi}$ where $2a_{sq}$ is the pipe width.

Transverse (x axis) and some of longitudinal coordinates of the ends are given in table 4.1. The other longitudinal coordinates of the ends vary within the ranges which are shown in table 4.1 as well. The pipe cross-sections are the same, $0.005m \times 0.005m$. Boundary conditions $p = 0$ should be applied to the open ends, where p is the acoustic pressure.

Table 4.1: Coordinates of central points of open ends of a unflanged network

End	x(m)	y(m)	End	x(m)	y(m)
1	0.0475	-0.051684	8	-0.0475	0.051684
2	0.0325	-0.051684	9	-0.0325	0.051684
3	-0.0325	-0.051684	10	0.0325	0.051684
4	-0.0475	-0.051684	11	0.0475	0.051684
5	-0.076684	$[-0.0475, -0.015]$	12	0.076684	$[0.015, 0.0475]$
6	-0.076684	$[-0.01, 0.01]$	13	0.076684	$[-0.01, 0.01]$
7	-0.076684	$[0.015, 0.0475]$	14	0.076684	$[-0.0475, -0.015]$

4.2.1.2 Targeted resonant frequencies

By giving the GA parameters, such as the number of individuals, generation gap, the maximum number of generations and wanted resonant frequencies, and running the GA program once, a optimal network can be found. This network has the closest resonant frequency to the targeted resonant frequency. The GA parameters should be adjusted for each case to obtain acceptable results.

Table 4.2: Results for the targeted resonant frequencies

Case	Targeted(Hz)	Obtained(Hz)	Error(%)
1	1250	1254	0.32
2	1400	1400	0
3	1600	1590	0.625

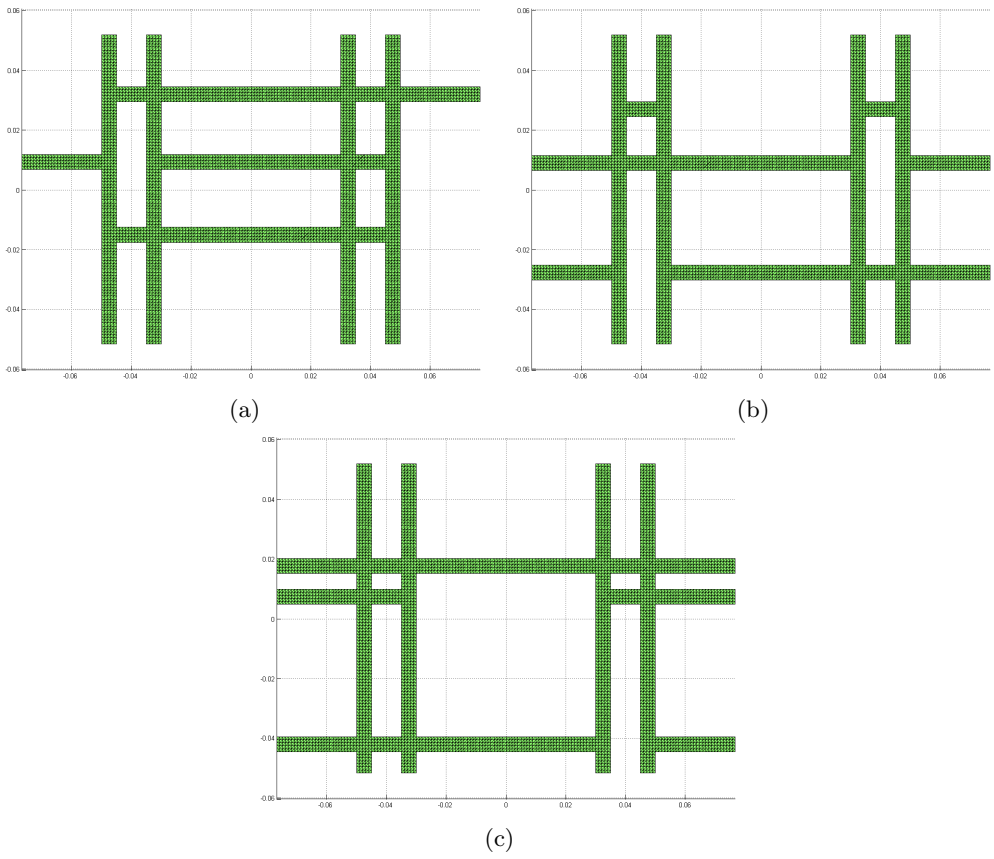

(a) (b)

(c)

Figure 4.8: (a) Network with the resonant frequency $1254Hz$; (b) Network with the resonant frequency $1400Hz$; (c) Network with the resonant frequency $1590Hz$.

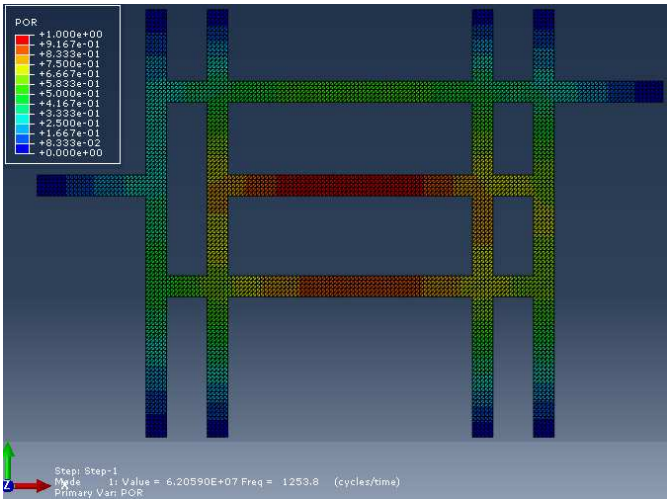

(a)

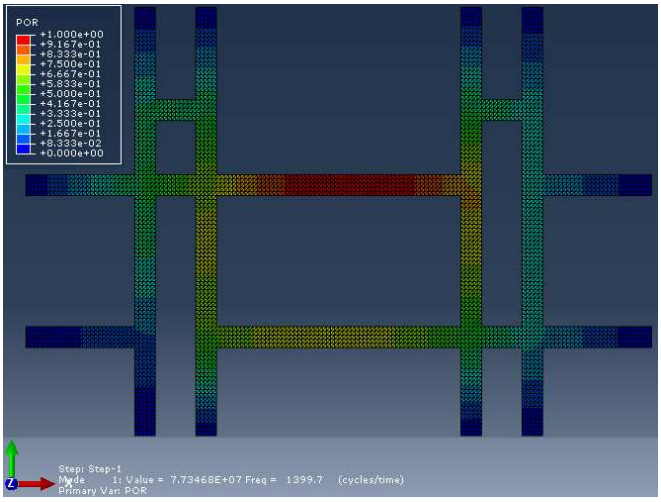

(b)

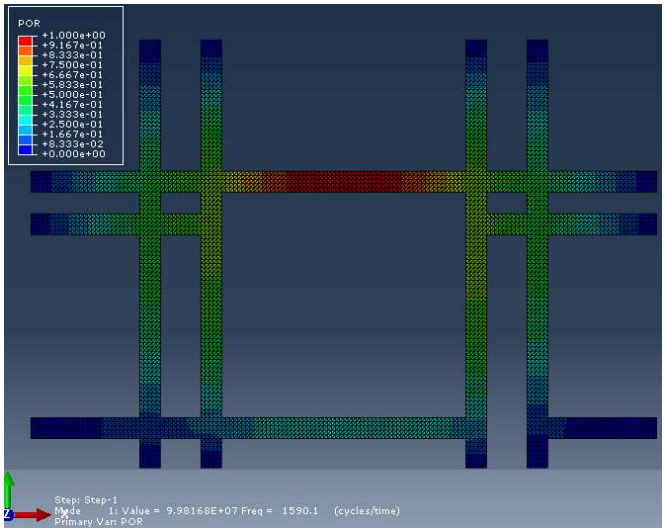

(c)

Figure 4.9: (a) Mode of acoustic pressure at $1254Hz$; (b) Mode of acoustic pressure at $1400Hz$; (c) Mode of acoustic pressure at $1590Hz$

In table 4.2, the wanted resonant frequencies are obtained by optimizing the network structure and the maximum error is less than 1%. The network structures and modes at the resonant frequencies can be seen in Fig.4.8a-4.8c and 4.9a-4.9c.

Besides the resonant frequencies shown in table 4.2, these three networks have other resonant frequencies within $2000Hz$. They are $1926Hz$ in case 1, $1976Hz$ in case 2 and $1947Hz$ in case 3.

In Fig.4.10 we can see the minimum difference between the targeted frequency $1400Hz$ and the resonant frequencies of individuals in each generation in GA procedure. In the first generation the difference is $259.52Hz$. From the second generation it becomes $6.93Hz$. In $7th$ generation a very good result is found. The difference between its resonant frequency and the targeted frequency $1400Hz$ is $0.22Hz$. The number of individuals in each generation used in the GA procedure is 1000.

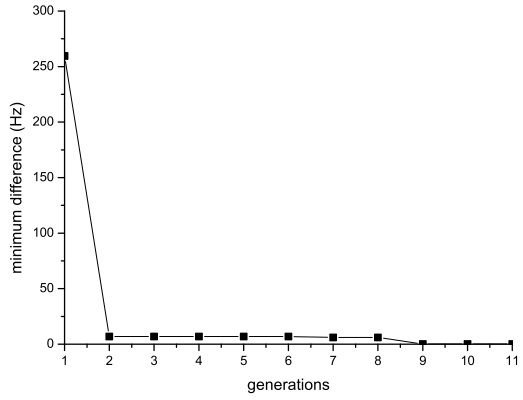

Figure 4.10: The minimum difference between the targeted frequency $1400Hz$ and the resonant frequencies of individuals in each generation in GA procedure

From the above examples one can conclude that the GA process developed before is suitable for the optimization and design of networks. Once the ranges of dimension parameters of networks are given, networks with targeted resonant frequencies can be found.

Experiments will be performed in chapter 5 to validate the optimization of the networks and to see if the frequencies obtained are close to the measured results.

4.2.1.3 Maximum number of resonant frequencies

It is of interest to know how many resonant frequencies one can get at most within a frequency range, for example $0-2000Hz$. With the dimension parameters of networks given before, a network with as many resonant frequencies as possible will be searched by GA.

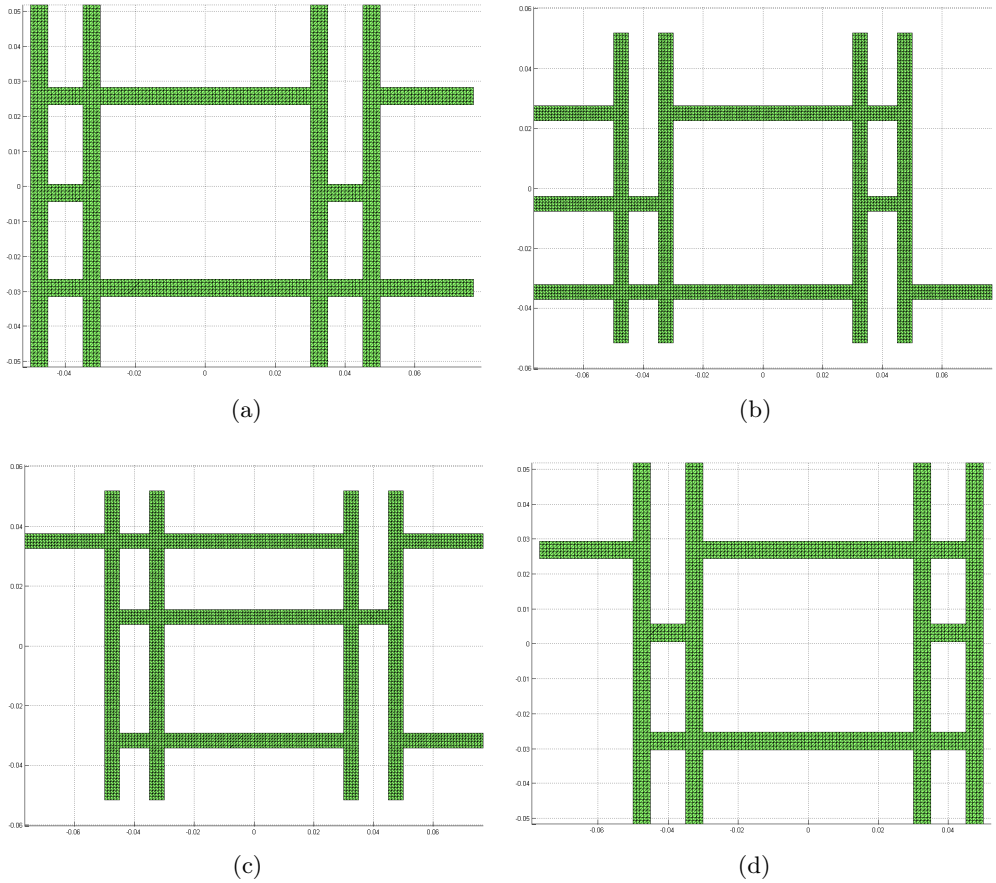

(a) (b)

(c) (d)

Figure 4.11: (a) Network 1; (b) Network 2; (c) Network 3; (d) Network 4

By changing the GA parameters and running GA program several times, three resonant frequencies at most within $0-2000Hz$ are found. There are several networks having 3 resonant frequencies, and some of them are shown in Fig.4.11a-4.11d.

Table 4.3: Networks with three resonant frequencies

Resonant frequency	**Network 1**	**Network 2**	**Network 3**	**Network 4**
$1st$	$1380Hz$	$1442Hz$	$1318Hz$	$1362Hz$
$2nd$	$1781Hz$	$1863Hz$	$1868Hz$	$1735Hz$
$3rd$	$1972Hz$	$1983Hz$	$1960Hz$	$1971Hz$

These four networks have different but close resonant frequencies in table 4.3. The first resonant frequency is around $1400Hz$, the second one is about $1800Hz$ and the third one is close to $2000Hz$.

Their structures can be seen in the Fig.4.11a-4.11d. They have totally different structures, but the resonant frequencies are similar. So it is possible to choose the net-

work according to needs or design a new network by changing the ranges of dimension parameters to satisfy our needs.

4.2.2 Network between a cylinder and a plane surface

4.2.2.1 Dimension parameters of network

In this example the network is between the cylinder and the plane surface used in section 2.5.2. The calculations of open end corrections are presented in section 3.3.2.1. The end corrections of longitudinal open ends can be calculated by formula (3.5). For the transverse ends their corrections, $0.0054m$, $0.0057m$, and $0.0054m$, are given by formula (3.14).

Table 4.4: Coordinates of central points of open ends of network between a cylinder and a plane surface

End	x(m)	y(m)	End	x(m)	y(m)
1	$[0.042, 0.0705]$	$-0.05 - EC$	8	$[-0.0705, -0.042]$	$0.05 + EC$
2	$[0.0045, 0.033]$	$-0.05 - EC$	9	$[-0.033, -0.0045]$	$0.05 + EC$
3	$[-0.033, -0.0045]$	$-0.05 - EC$	10	$[0.0045, 0.033]$	$0.05 + EC$
4	$[-0.0705, -0.042]$	$-0.05 - EC$	11	$[0.042, 0.0705]$	$0.05 + EC$
5	-0.0804	-0.03333	12	0.0804	0.03333
6	-0.0807	0	13	0.0807	0
7	-0.0804	0.03333	14	0.0804	-0.03333

Longitudinal and some transverse coordinates of the ends are given in table 4.4. The other transverse coordinates vary within the ranges which are shown in table 4.4. The pipe cross-sections are the same, $0.009m \times 0.009m$. Boundary condition $p = 0$ should be applied to the open ends, where p is the acoustic pressure.

In table 4.4, EC means the value of longitudinal end correction, which can be calculated by formula (3.5).

4.2.2.2 Maximum number of resonant frequencies

In this section we try to get networks with the maximum number of resonant frequencies within the frequency range $0 - 2000Hz$. With the dimension parameters of networks given before, networks with as many resonant frequencies as possible will be searched by GA. The networks that we want should have repeated junctions in the longitudinal direction (y axis in Fig.4.7). It means in each column of the network in Fig.4.7 the junctions should be the same.

By changing the GA parameters and running the GA programme several times, four resonant frequencies at most within $0 - 2000Hz$ are found. There are 2 networks

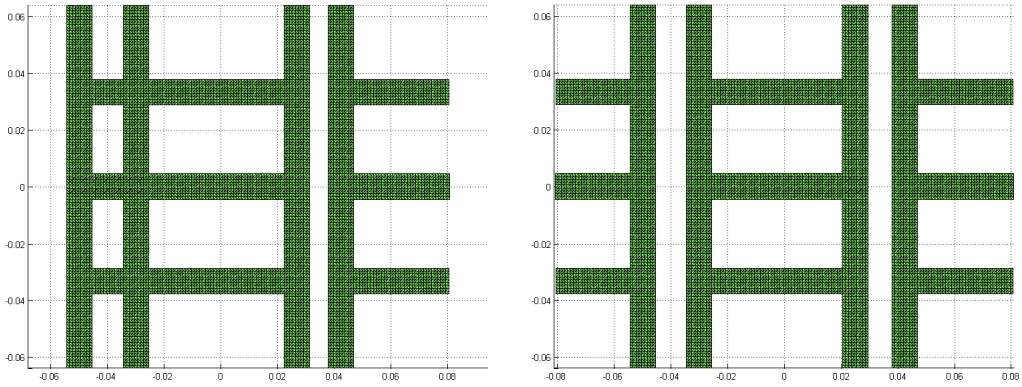

(a) (b)

Figure 4.12: (a) Network 1; (b) Network 2.

Table 4.5: Networks with four resonant frequencies

Resonant frequency	**1st**	**2nd**	**3rd**	**4th**
$Network1$	$1055Hz$	$1797Hz$	$1799Hz$	$1929Hz$
$Network2$	$1201Hz$	$1799Hz$	$1890Hz$	$1989Hz$

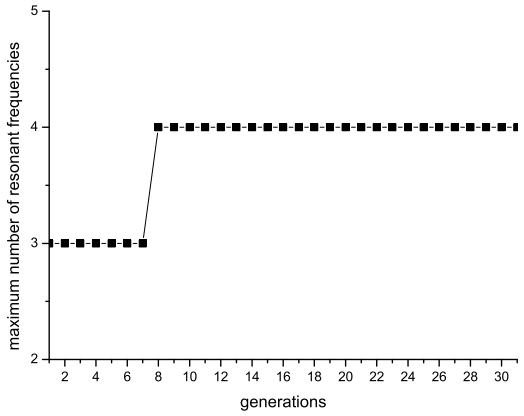

Figure 4.13: The maximum number of resonant frequencies for each generation in GA procedure

having 4 resonant frequencies, and they are shown in Fig.4.12a and Fig.4.12b. The resonant frequencies are shown in table 4.5.

In Fig.4.13, the maximum number of resonant frequencies of a network in the first generation is 3. It changes to 4 in the $8th$ generation and then keeps the same value until the end of the GA procedure. Since we are interested in periodic networks, only networks with repeated junctions could be generated in each generation. So the number of individuals in each generation is just 30.

4.3 Conclusions

Different optimization methods are introduced and compared in this chapter. Genetic algorithms are chosen to design and optimize the 2D network resonators.

A network with 12 junctions is optimized to illustrate that GA procedure developed in this chapter can be used to design networks. The end corrections of open ends should calculated first. No matter the network has flange or not, the networks with targeted resonant frequency or a maximum number of resonant frequencies within a given frequency range can be found by GA after the dimension ranges of networks and GA parameters are given.

We can choose the network according to needs or design a new network by changing the ranges of dimension parameters in the GA procedure developed in this chapter to satisfy our needs.

Chapter 5

Validations with measurements

In this chapter, the multi-domain coupling methods introduced in chapter 2, the matlab codes 2DNRF developed in chapter 3 and optimization methods of resonant frequencies in chapter 4 are validated with measurements.

We use wood to build networks, flanges and plane surfaces, for wood is easy to cut, bend, shape and glue. Besides, wood can give the rigid boundary conditions used in our simulations. A real tire on the road is also measured and calculated in this chapter.

5.1 Sound pressure fields of pipes between a cylinder and a plane surface

The flange-network interaction model has been established in chapter 2. In this section, experiments will be carried out to validate numerical simulations of this model. The flange in the model developed before could have arbitrary shape. For the sake of convenience, a circular flange in Fig.5.2b is used in both numerical simulations and experiments. The radius and width of the cylinder in Fig.5.2b are $0.27m$ and $0.15m$. Its location can be seen in Fig.5.1. The sketch of the experimental setup is shown in Fig.5.1. The locations of source and receiver are exchanged in Fig.5.2a thanks to the reciprocity principle. The experiments are performed in a large testing hall to avoid influences of the reflections from the wall. The plywood on the floor in Fig.5.2a is used to simulate the rigid plane surface. Sweep signals within $2000Hz$ are generated by a generator. The generator, amplifier and B&K pulse data acquisition system can be seen in Fig.5.3a and 5.3b. The center of the speaker is at $(1, 0, 0.06)$. The microphone is at $(0.1, 0, 0.005)$.

First we present the acoustic source used in our experiments. Then the acoustic

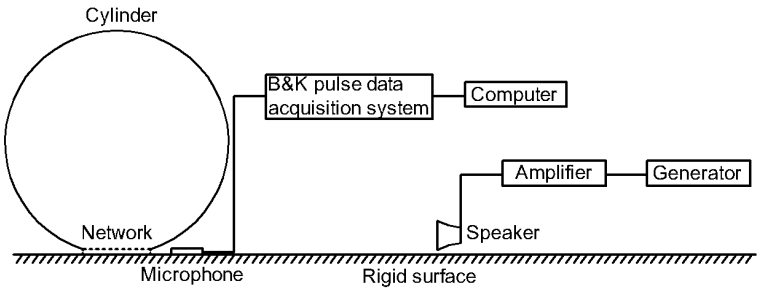

Figure 5.1: Sketch of experimental setup

(a) (b)

Figure 5.2: (a) The experimental set-up; (b) flange used in calculations and experiments

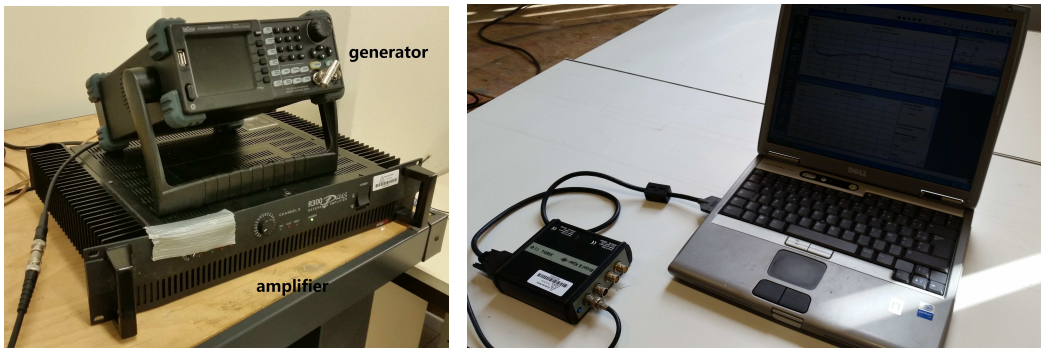

(a) (b)

Figure 5.3: (a) Generator and amplifier; (b) B&K pulse data acquisition system

fields of a cylinder on a plane surface are computed and measured. In this comparison, there is no pipe between the cylinder and the plane surface. Next a straight pipe and a network between the cylinder and the plane surface are measured. Last a optimized network between the cylinder and the plane surface is solved and measured.

5.1.1 Point source

In our simulations, a dimensionless point source is used, and it has been assumed omni-directional. Typical sources used in previous researches are audio speakers [55], audio speakers coupled with circular pipe [94] and electrostatic spark sources [68]. In our study the predicted results will not be compared directly with the measured results. Instead, the general tendencies and frequency-dependant variations of the sound intensity will be compared between the predicted and measured results. Such comparisons are very common and widely used in previous studies such as in [95] and [55]. So it is not necessary to use a omni-directional source in our experiments. A real loudspeak, whose signal is digitally generated, is used as source in the experiments. The dimensions are $0.12 \times 0.12 \times 0.12m$.

5.1.2 Plane surface with or without a cylinder

Since the measurements are performed in a large testing hall, it is essential to know if the influences of reflections from walls and roof can be ignored or not. In this section, two measurements are done for this purpose. In the first case, a cylinder is located on a plane surface, but there is no pipe between the cylinder and the plane surface. In the second case, we move the cylinder away from the plane surface.

The acoustic field of the first case can be calculated by BEM. In the second case the plane surface is rigid, so it can be considered as a symmetric plane. An image source is created in Fig.5.4b. Thus, the second case can be solved by equations (5.1) and (5.2). The predicted results can be seen in Fig.5.5a. The measured results of SPL are shown in Fig.5.5b.

$$p = \frac{e^{ikd_1}}{4\pi d_1} + \frac{e^{ikd_2}}{4\pi d_2} \tag{5.1}$$

where d_1 and d_2 are the distances from the source and the image source to the receiver in Fig.5.4b.

$$SPL = 10\log_{10}\frac{|p|^2}{4 \times 10^{-10}} \tag{5.2}$$

When we compare the predicted results in Fig.5.5a and the measured results in

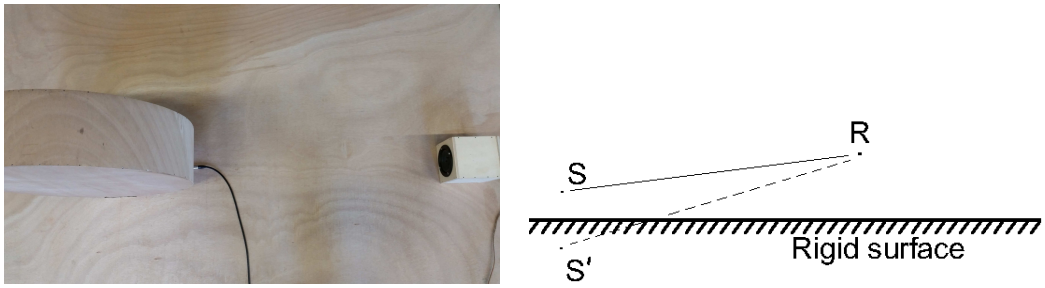

(a) (b)

Figure 5.4: (a) A cylinder on a plane surface (no pipe between the cylinder and the plane surface); (b) A rigid plane surface between a source and an image source.

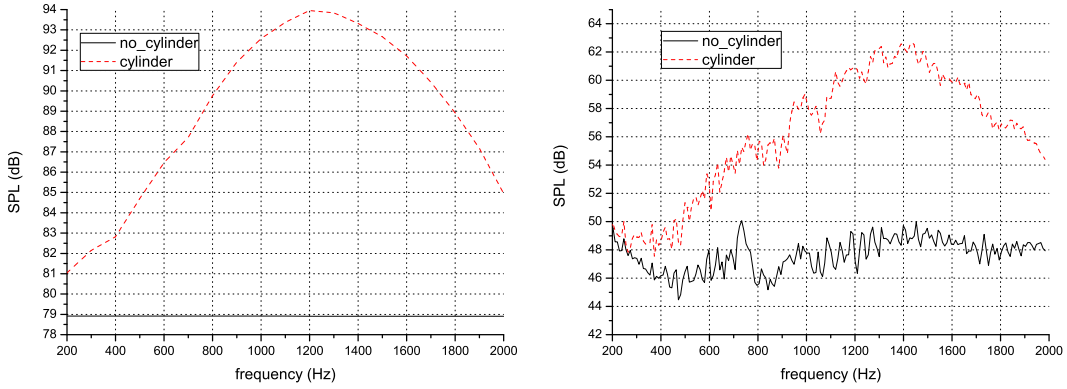

(a) (b)

Figure 5.5: (a) Predicted results; (b) Measured results.

Fig.5.5b, similar tendencies of SPL can be found. The maximum difference of predicted SPL between the case with the cylinder and the case without the cylinder is about $15dB$ around $1250Hz$ in Fig.5.5a. The maximum difference between these two cases of the measured SPL is about $14.5dB$ around $1300Hz$ in Fig.5.5b. The predicted results agree well with the measured results. We can conclude that the reflections from the walls and the roof can be ignored in our experiments.

5.1.3 Straight pipe

The example calculated in section 2.5.2.1 is measured in this section, which can be seen in Fig.5.6. We measured the case with a straight pipe and the case without pipe. In the case without pipe, we close the pipe ends with woods.

The results are shown in Fig.5.7, where we can see a reduction of SPL of $3.5dB$ around the resonant frequency $1460Hz$. The reduction of numerical results with viscous losses in Fig.2.17 is $5.5dB$ at the resonant frequency $1430Hz$. The difference

Figure 5.6: A straight pipe between a cylinder and a plane surface

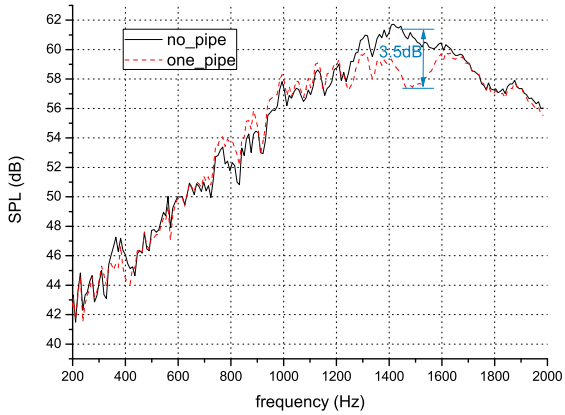

Figure 5.7: Measured results of flange with a straight pipe

of reduction at the resonant frequency between measurement and simulation is $2dB$, which will be smaller if the thermal conduction losses are taken into account. The influence of thermal conduction losses are shown in table 2.1 by solving another case. But in this example the tendencies of numerical SPL are similar to the measurements, and the resonant frequency is estimated correctly.

5.1.4 Network

The network calculated in section 5.1.4 is measured in this part to validate the multi-domain coupling methods proposed in chapter 2. When we measure the case without network, we close the pipe ends in Fig.5.8 with woods.

Table 5.1: Predicted and measured results

Predicted f	Predicted differences	Measured f	Measured differences
$1220Hz$	$2.85dB$	$1200Hz$	$4dB$
$1800Hz$	$4.88dB$	$1800Hz$	$3.5dB$
$1880Hz$	$2.44dB$	$1900Hz$	$3.2dB$

Figure 5.8: A network between a cylinder and a plane surface

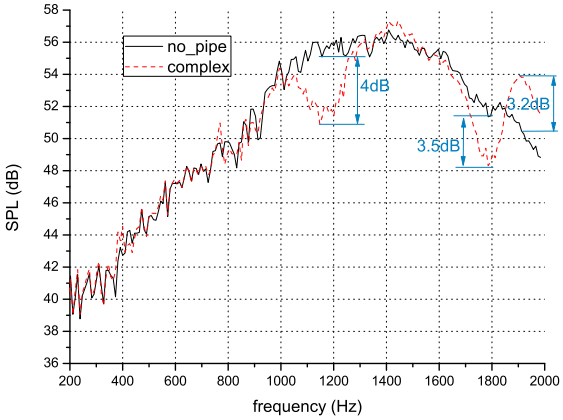

Figure 5.9: Measured results of flange with a network

The experiment is shown in Fig.5.8. The results can be seen in Fig.5.9. There are three SPL extrema around the two resonant frequencies $1232Hz$ and $1823Hz$ which are obtained by 2DNRF in section 3.3.2.1. Around the first resonant frequency $1232Hz$, we can see a reduction. Around the second resonant frequency $1823Hz$, there are a reduction and an amplification. The predicted and measured frequencies of these three extrema and the differences between the case with pipes and the case without pipe are shown in table 5.1.

At the second extremum, the SPL reduction of experimental results between the solid line and the dash line is about $3.5dB$. The SPL reduction $4.88dB$ of numerical results with viscous and thermal conduction losses is closer to the measurements. So for a thin pipe in this work, the viscous and thermal conduction losses should be taken into account. Otherwise, the difference of reductions between experimental and numerical results for the second extremum is too large.

Compared with simulations, the frequencies of these three extrema, which are about $1200Hz$, $1800Hz$ and $1900Hz$, are estimated correctly, and the variations of

these three extrema are also very close. The errors are $1.15dB$, $1.38dB$ and $0.76dB$. Besides, we can see similar tendencies of SPL between experiments and simulations.

The resonant frequencies of this network, $1232Hz$ and $1823Hz$, are estimated in section 3.3.2.1 by 2DNRF. From Fig.5.9 we can see the variations of SPL around these two frequencies. So the resonant frequencies are estimated correctly in section 3.3.2.1.

5.1.5 Optimized network

The network between the cylinder and the plane surface is optimized in section 4.2.2. The acoustic fields of network 1 in Fig.4.12a are calculated by A2BEM and measured in order to validate the A2BEM and GA optimization methods. When we measure the case without network, we close the pipe ends in Fig.5.10 with woods.

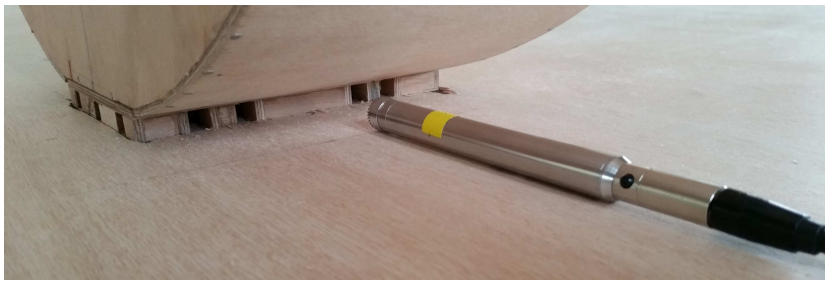

Figure 5.10: A optimized network between a cylinder and a plane surface

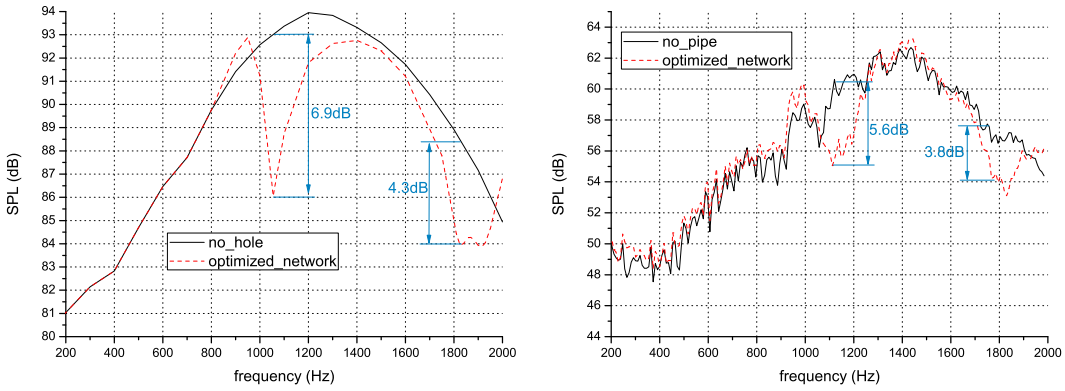

(a) (b)

Figure 5.11: (a) Predicted results of a optimized network between a cylinder and a plane surface; (b) Measured results of a optimized network between a cylinder and a plane surface.

The predicted results are shown in Fig.5.11a. The resonant frequencies of this optimized network are given in section 4.2.2, which are $1055Hz$, $1797Hz$, $1799Hz$ and $1929Hz$. The second and the third resonant frequencies are very close, so just

one extremum can be seen around $1800Hz$ in Fig.5.11a, where we can see two other extrema around $1055Hz$ and $1929Hz$.

The measured results are given in Fig. 5.11b, where the variations of SPL are similar to the predicted results in Fig.5.11a. The reductions of predicted SPL are close to the reductions of measured SPL. Around the first resonant frequency $1055Hz$, we can see a maximum reduction $6.9dB$ in Fig.5.11a, and $5.6dB$ in Fig.5.11b. Another big reduction for the predicted results is $4.3dB$ around $1800Hz$, and $3.8dB$ for the measured results which is also around $1800Hz$.

If we compare this optimized network with the network in section 5.1.4, the results of the optimized network are better. There is no peak around $1900Hz$, whereas we can see a peak around $1900Hz$ in Fig.5.9. Because the optimized network has a resonant frequency at $1929Hz$. This gives reductions of SPL that we can see clearly in Fig.5.11a.

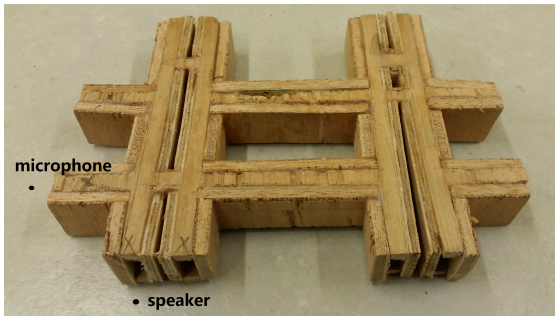

Figure 5.12: Optimized wooden network with the resonant frequency $1400Hz$

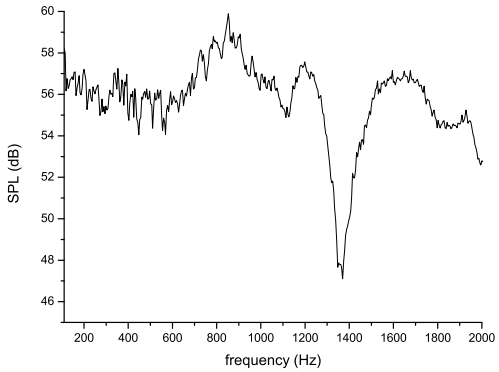

Figure 5.13: Measured SPL for the optimized wooden network with the resonant frequency $1400Hz$

Besides the flanged network given above, an unflanged network in Fig.5.12 is also measured in order to validate the optimization in Fig.4.9b in section 4.2.1.2. The

network in Fig.5.12 is built with wood. A speaker and a microphone are put near the open ends in Fig.5.12.

The network optimized in section 4.2.1.2 is a 2D network, so the depth is not given in the optimization. In the experiments, the depth that we use is $0.01m$.

The SPL obtained by the microphone is shown in Fig.5.13. We can see a deep valley at frequency $1370Hz$ which is close to the targeted resonant frequency $1400Hz$. So the GA optimization procedure developed in chapter 4 can give the resonant frequencies that we want.

5.2 Tire

In order to know whether the tire treads in the contact zone have influences on the acoustic radiation of the tire and road system, measurements of the acoustic fields for a real tire are performed. Then the estimations of the resonant frequencies of the tire treads in the contact zone and the calculations of the sound pressures are done by the methods proposed in the previous chapters.

(a) (b)

Figure 5.14: (a) Tire with an open network; (b) Tire with a closed network.

The tire treads in Fig.5.14a are very complex. There are three longitudinal pipes (pipe $1, 2$ and 3) with large cross-sections, two longitudinal pipes (pipe 4 and 5) with very small cross-sections and many transverse pipes with different cross-sections. For the sake of simplicity, we only investigate the network in the middle of the contact zone. The network consists of the longitudinal pipes 1 and 2 and the large transverse pipes between them in Fig.5.14a. But there are also many small pipes connecting to the network to be studied, so we fill them with silicone. We also fill the longitudinal pipe 3 to make sure that there is no other longitudinal pipe except the pipe 1 and 2 in the network to be investigated.

Two tests are performed. In the first test, the network is open. In the second test,

we fill the network with silicone in the contact zone (see Fig.5.14b). We can see that the ends of the pipes 1 and 2 are closed in Fig.5.14b. These two tests are compared to study the influence of the treads on the acoustic radiation.

We use five concrete cylinders (Fig.5.15a) as the load from the car to get the flat contact zone (Fig.5.15b). In order to obtain the dimensions of the network in the contact zone, first we put the tire on the flour for several minutes (Fig.5.16a). Next we move the tire on a clean surface. Then we lay the tire flat on the surface. In Fig.5.16b we can see the elliptical contact zone which is given by the lumps of flour on the tire or on the road. When we compare the tire with and without the lumps of flour in Fig.5.17, we can see clearly the shape of the contact zone. The length of the contact zone is $0.161m$. The experimental setup is the same as the wooden cylinder case, which is shown in Fig.5.1. The source is at $(1, 0, 0.06)$, and the receiver is at $(0.15, -0.005, 0.005)$.

(a) (b)

Figure 5.15: (a) The load of five concrete cylinders; (b) The contact zone between the tire and the road.

(a) (b)

Figure 5.16: (a) The tire on the flour; (b) The contact area given by the flour.

The network of the real tire to be investigated is simplified and meshed in Fig.5.18a. The pipes between longitudinal pipes 1 and 2 of the real tire are modeled as straight

Figure 5.17: The tire with and without the lumps of flour

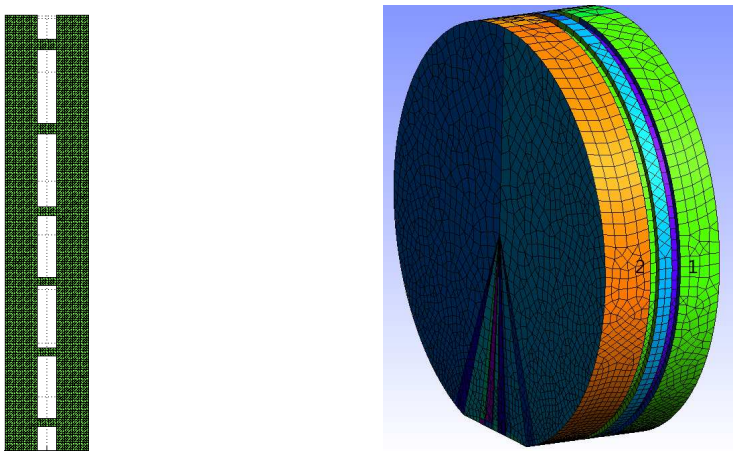

(a) (b)

Figure 5.18: (a) The simplified network; (b) The meshes of the BEM model of the tire used in the multi-domain coupling methods.

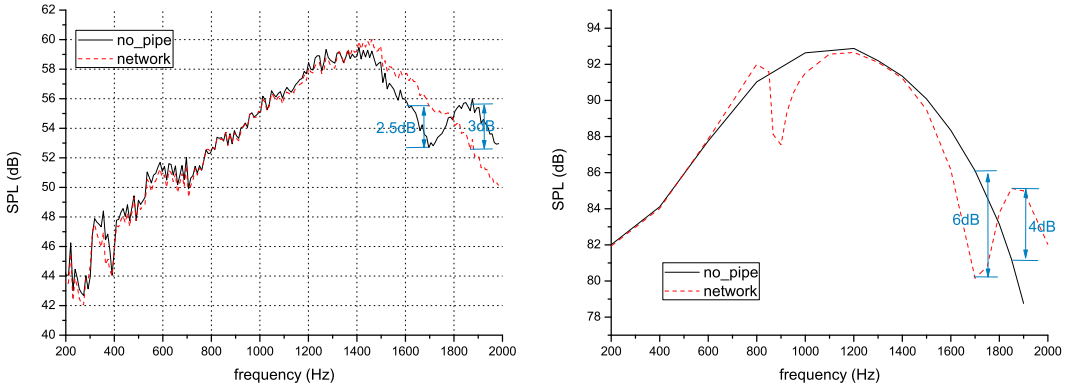

(a) (b)

Figure 5.19: (a) Measured results of the network between a tire and a plane surface; (b) Predicted results of the network between a tire and a plane surface.

pipes. The length of the longitudinal pipe is $0.161m$. The width is $0.012m$. The distance between the two longitudinal pipes is $0.019m$ which is very short, so we can use the same end correction for the two longitudinal pipes. The end correction of the longitudinal pipe is $0.0169m$, and it is calculated by the methods introduced in chapter 3. The widths of the transverse pipes are $0.003m$ or $0.004m$.

The resonant frequencies of the network within $2000Hz$ are $868Hz$ and $1734Hz$. They are estimated by the program 2DNRF proposed in chapter 3. From the modes of the network at $868Hz$ and $1734Hz$ in Fig.5.20a and Fig.5.20b we know that these two resonant frequencies are because of the resonance of the two straight pipes 1 and 2. If we use equation (3.8) to calculate the resonant frequencies of the straight pipe 1 or 2, we can get the resonant frequencies $880Hz$ and $1761Hz$ which are close to the resonant frequencies obtained by 2DNRF.

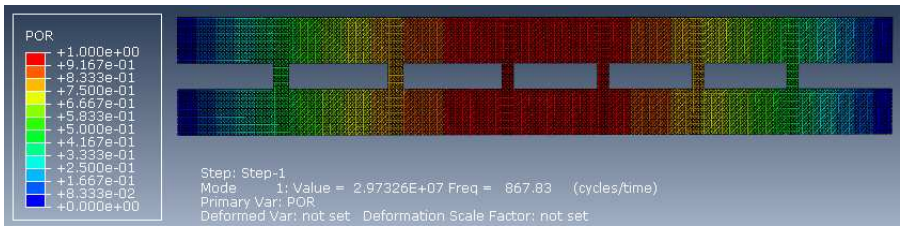

(a)

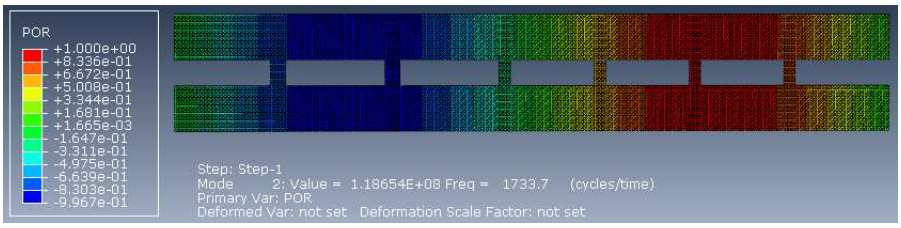

(b)

Figure 5.20: Modes of the network obtained from Abaqus by 2DNRF: (a) The first resonant frequency $868Hz$; (b) The second resonant frequency $1734Hz$.

However, from the measured sound pressures in Fig.5.19a we can see only one resonant frequency around $1734Hz$. There is no variation of SPL around $868Hz$. The reason is not clear. Maybe because the tire is not pressed firmly in the whole contact zone. The load of the five concrete cylinders that we use are too light compared to the load from a real car. When we did the tests of wooden networks, we found that if the woods are not glued firmly no resonant frequency can be found. For the straight pipe we know that the longer the pipe is, the smaller the first resonant frequency is. Since the first resonant frequency in the measured results is about twice as many as the first estimated resonant frequency, the length of the real contact zone may be approximately half of the length used in the estimation. The contact zone where the

tire is pressed firmly may be just the central part of the ellipse in Fig.5.16b. Although the outer parts of the elliptical surface of the tire touch the road, maybe they are not pressed firmly on the road. Besides, the tire in our test is just the tire surface. So it is very difficult to press the whole network in Fig.5.18a firmly on the road.

The same problem can be seen in the experimental results from the report [96]. This experiment is similar to ours. In this experiment, first the open treads are measured, and then these treads are filled and measured again. The results can be seen in Fig.5.21b. The tire footprint in the contact zone is shown in Fig.5.21a where the length of the footprint, about $0.22m$, is measured. For the two longitudinal pipes, we can estimate the resonant frequencies by using the measured length. There should be a resonant frequency around $600Hz$. But there is no SPL variation around $600Hz$ in Fig.5.21b. Above $1000Hz$ we can see obvious differences between the two curves. Besides, from our measured results of the wooden networks and the wooden cylinder we can also see clear variations of SPL above $1000Hz$. Therefore, in this work for the real tire we will put the focus on the frequencies above $1000Hz$ because in this frequency range our calculations and estimations agree with the measured results.

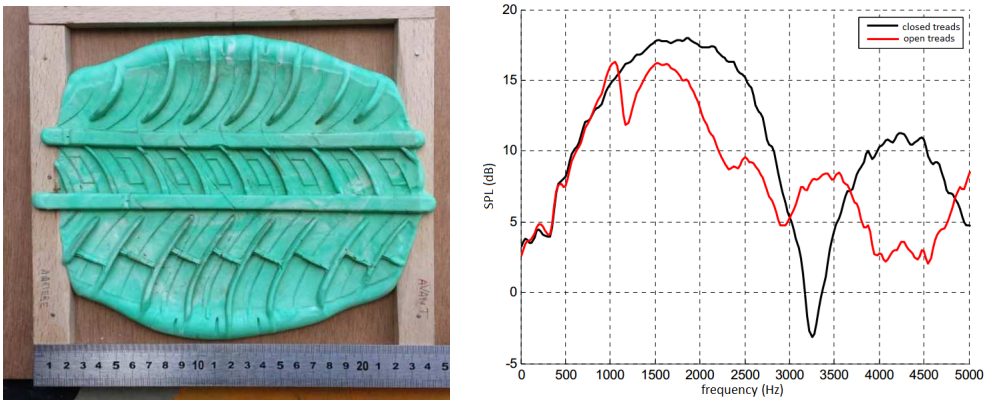

(a) (b)

Figure 5.21: (a) The tire footprint in the contact zone; (b) The measured sound pressure level for a tire with the open or closed treads in the contact zone.

In order to predict the influence of the tire treads on the acoustic fields of our tire and road systems, the network is modeled as the one in Fig.5.18a. The BEM meshes of the tire can be seen in Fig.5.18b. We ignore the transverse grooves on the tire surface except the ones in the network to be studied. We only take into account the two large longitudinal pipes 1 and 2. The other longitudinal pipes are not modeled. The lateral surface in the model is a flat surface. Although the model is not the same as the real tire, it is not very important. Because the model is used to compare the

cases with and without the network and estimate the influence the network on the acoustic fields. In the calculations of these two cases, the network to be investigated will be changed from open ends to closed ends, but the other parts keep the same. The tire width and radius are $0.165m$ and $0.27m$, respectively. The contact zone is $0.161m \times 0.165m$. Two calculations are done. In the first calculation, the ends of the network are open. We use the multi-domain methods given in chapter 2 to solve the problem. In the second calculation, the ends of the network are closed. We use BEM to do the calculations.

The measured and predicted results at receiver $(0.15, -0.005, 0.005)$ are shown in Fig.5.19a and 5.19b. Unlike the wooden cylinder case in section 5.1, the general tendencies of the predicted SPL are not quite similar the measured results. The reason is that the BEM model in Fig.5.18b is not exactly the same as the real tire, for example the lateral surface. But the influences of the network on the acoustic fields around $1734Hz$ are estimated approximately. Around the resonant frequency $1734Hz$ of the network, we can see the variations of SPL in Fig.5.19b. In Fig.5.19a, we can see the similar variations around $1734Hz$. But errors of reductions and amplifications between the measured and predicted results can be seen. These errors are due to the differences between the real tire and the simplified model that we use. Around $868Hz$ there is a resonant frequency in Fig5.19b, but it can not be seen in the measured results. The frequency range of interest is above $1000Hz$, so we ignore this difference.

Although above $1000Hz$ the agreements between the measured and predicted results in our case of the real tire are not as perfect as the agreements in the case of the wooden cylinder and the wooden networks, we can still use our proposed model and methods to estimate the influences of the tire treads on the acoustic fields.

5.3 Conclusions

In this chapter, several flanged or unflanged wooden pipes and a real tire are measured to validate our predictions. Good agreements can be seen for the wooden cases. However, for the real tire some differences between the predicted and measured results are found within $1000Hz$.

By comparing the predicted and measured results of a flanged straight pipe, we can conclude that the viscous and thermal losses should be taken into account in the calculation of the acoustic fields.

For the flanged wooden network, resonant frequencies can be estimated from the predicted and measured SPL curves. These resonant frequencies can also be estimated by the matlab codes 2DNRF. Good agreements are found. Since the calculations and

the measurements of the SPL are quite time-consuming, 2DNRF is an easier and better method for the estimation of the resonant frequencies of the networks.

The tendency and variation of the measured SPL agree well with the predicted results for the flanged wooden pipes, which validates the model and computational methods proposed in chapter 2. The flanged and unflanged wooden networks are optimized by the proposed GA procedure to get the wanted resonant frequencies. From the measured SPL curves, we can find these resonant frequencies. So the GA procedure can be used to get the targeted resonant frequencies.

For the real tire, above $1000Hz$ the predicted resonant frequency and SPL variations agree with the measured results. Therefore, the proposed model and numerical methods will be used to study the influence of the tire treads and the road textures on the acoustic fields above $1000Hz$.

Chapter 6

Optimization of tire treads and road textures

Acoustic radiation from tire and road system is influenced by the horn between the tire and the road and networks formed by tire treads and road textures in the contact zone. Previous researches on acoustic radiation from tires and roads, for example the thesis [97], only considered smooth tires and roads for horn effects. In the researches about tire treads, resonances of pipes are always thought to be a reason of sound enhancement. However, the pipe resonances should be investigated together with horn effects because both of them are noise radiation mechanisms. In fact, the network resonances can reduce the sound pressure at the resonance frequencies, which can be seen in Fig.2.11. Exterior acoustic fields are amplified by the horn between the tire and the road, but the acoustic interactions between the exterior fields and the resonance of networks change the amplifications. In this chapter, the influence of treads and textures on horn effects will be investigated in detail. The treads and the textures will be optimized to reduce the acoustic radiation. The optimization process is shown in Fig.6.1.

There are several assumptions when modelling tire treads and road textures: a. there are only longitudinal grooves on the tire surface and road surface except in the contact zone, b. there are only right-angled junctions in the networks in the contact zone, c. the pipes in the networks have the same cross-section. d. The tire is pressed very firmly on the road in the whole contact zone. An example of network in the contact zone simulating treads between the tire and the road is meshed in Fig.2.12.

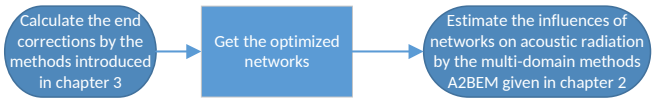

Figure 6.1: Optimization process of tire treads and road textures

6.1 Acoustic excitations

6.1.1 Comparison of excitations

Noise of rolling tires on the road are generated by vibrations and air-pumping. Velocities on a tire surface and a point source are used to simulate the noise generation mechanisms. They are compared for calculating the noise radiations in this section.

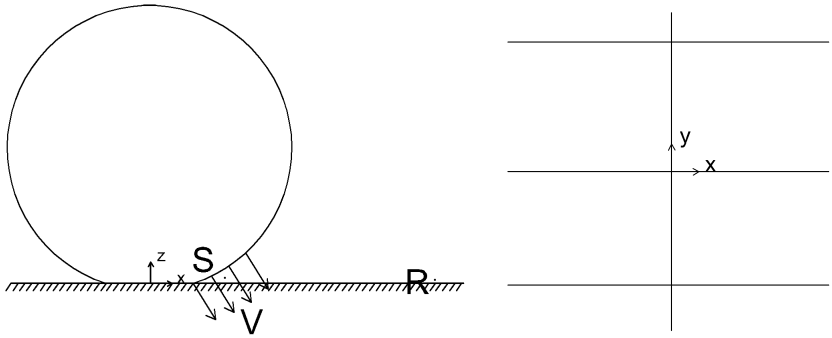

Figure 6.2: (a) Point source and velocity excitation; (b) A simple network between the tire and the road.

In Fig.6.2a, we can see the locations of the point source and the velocities used in the simulations. The network used in the comparison is shown in Fig.6.2b. In the calculation no viscous and thermal conduction losses are taken into account, because these losses only change the amplitudes of the pressure at the resonant frequencies. The amplitudes are not very important to the conclusions in this part.

From Fig.6.3a and 6.3b, we can conclude that under these two types of excitations the resonant frequency is the same and the variations of pressure are similar at the resonant frequency. For a point source, there is a peak of amplification in the case of smooth tires, but for the velocity excitation, we cannot see a peak within $2000Hz$. If higher frequencies are calculated for the velocity excitation case, the peak of amplification will be seen. However, more elements and nodes should be used for higher frequencies, and it will lead to longer computational time. So we will choose the point source as the excitation.

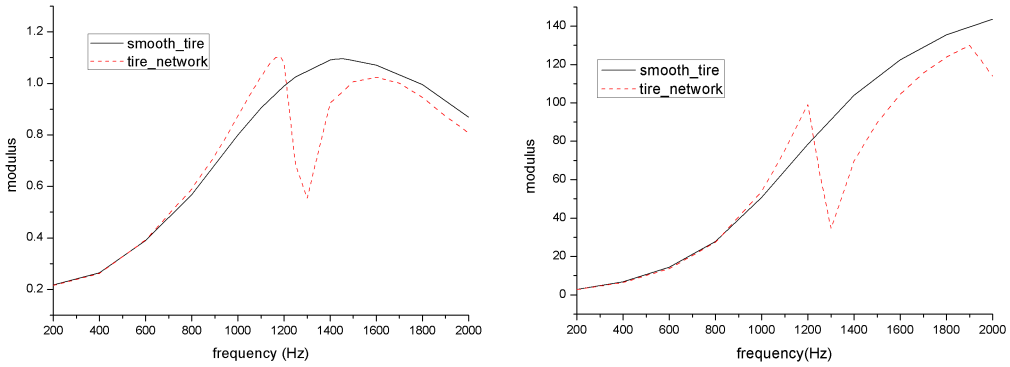

(a) (b)

Figure 6.3: Modulus of pressure at R under different excitations (a) Point source excitation; (b) Velocity excitation on the tire.

6.1.2 Point source position

Different positions of point source are compared in this section. The network in the calculations is the same one, and the tire and receiver positions keep the same. Since we just compare the different source positions, viscous and thermal conduction losses are not very important to the conclusion and will not be taken into account in the simulations.

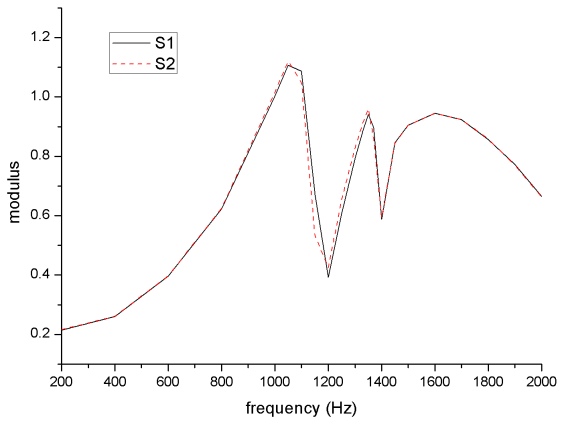

Figure 6.4: Pressure modulus at R $(1, 0, 0.265)$ for different source positions: $S1$ $(0.1, 0, 0.005)$ and $S2$ $(0.1, 0.0325, 0.005)$

In Fig.6.4 we can see that for different source positions in the transverse direction (y axis in Fig.6.2b) the pressure is very close within $2000Hz$. So the source position in the transverse direction between the tire and the road has hardly any influence on the pressure.

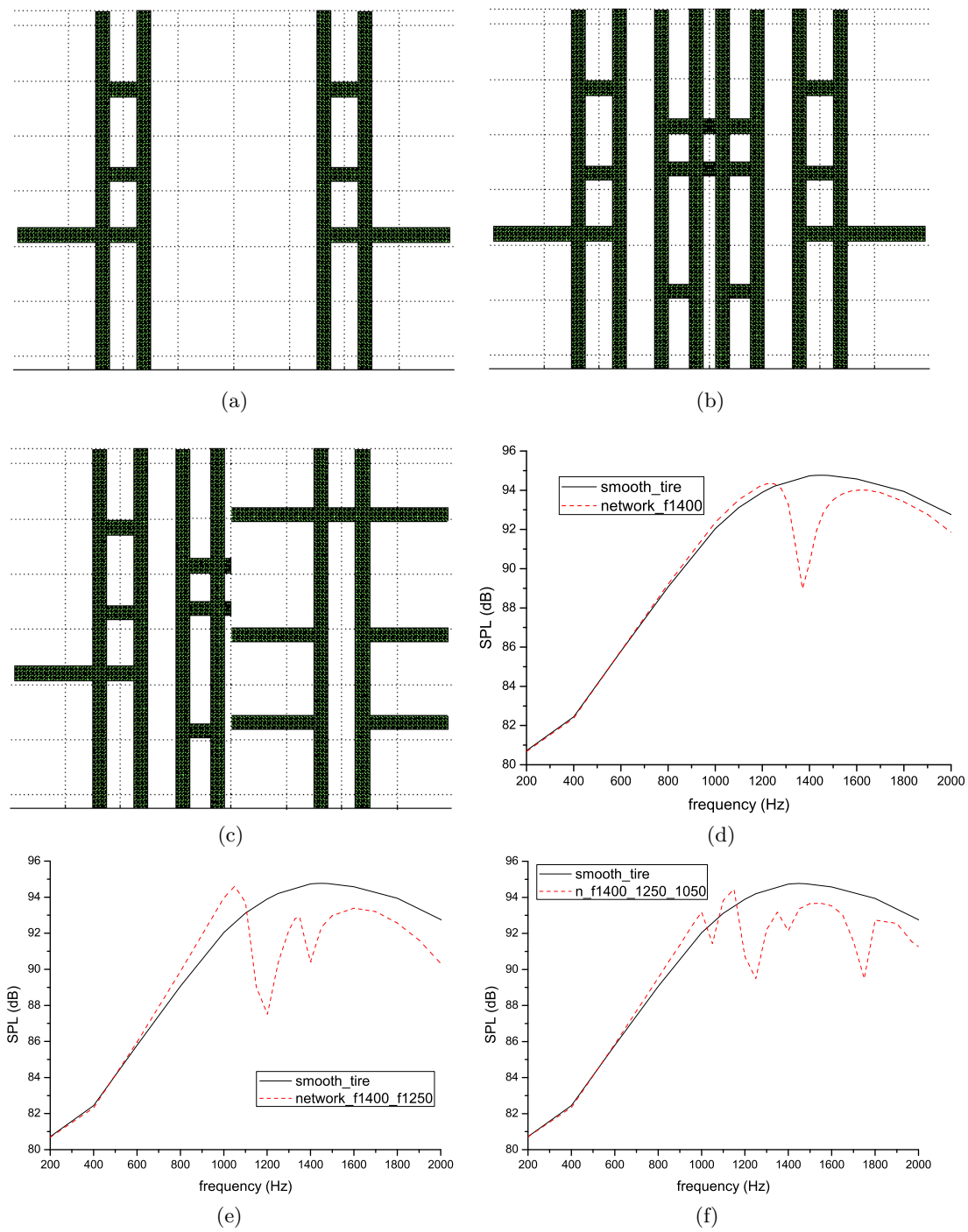

Figure 6.5: Networks (including end corrections) in the contact zone with targeted resonant frequencies (The vertical direction is the rolling direction): (a) $1400Hz$; (b) $1400Hz$ and $1250Hz$; (c) $1400Hz$, $1250Hz$ and $1050Hz$ (There are five closed ends in the middle of the contact zone). SPL at R for a tire with networks in the contact zone: (d) One network targeting $1400Hz$; (e) Two networks targeting $1400Hz$ and $1250Hz$; (f) Three networks targeting $1400Hz$, $1250Hz$ and $1050Hz$.

6.2 Optimization of tire treads

Tire treads in the contact zone are in the same plane, so can be considered as 2D networks. The multi-domain coupling method A2BEM can be used to calculate the acoustic fields. Viscosity and thermal conduction losses at pipe walls will be taken into account in the analytical relations of straight parts of the networks.

The GA procedure proposed in chapter 4 is used to optimize the tire treads. The number of rows and columns in the network should be given in the GA procedure. In our optimization three transverse rows and six longitudinal columns are chosen. The tire dimensions are shown in section 2.5.1.3. Pipe width is $0.005m$.

6.2.1 Parallel networks

In Fig.6.3a, there is a peak of sound pressure for the smooth tire without network in the contact zone. The peak has a wide bandwidth. If a network in the contact zone is optimized to target the frequency of this peak, new peaks will be created around the targeted peak.

By using several parallel networks, bandwidths of the new peaks will become very narrow. In our optimizations the contact zone is divided into several parts in the transverse direction (y axis in Fig.6.2a). In each part a network is inserted. The first network is used to target the original peak, and the following networks are optimized to target the peaks that the last network creates until there is no place for another new network.

Optimizations of the networks in the contact zone are performed by the GA procedure developed in chapter 4. The first network targets the peak $1400Hz$. In Fig.6.5a, there are two symmetrical networks with an optimized resonant frequency $1376Hz$. In Fig.6.5d, we can see the SPL reduction $5.5dB$ at the resonant frequency $1376Hz$. Two new peaks emerge around the frequencies $1250Hz$ and $1600Hz$.

The next network is optimized to target $1250Hz$. In Fig.6.5b, there are two symmetrical networks with resonant frequencies $1240Hz$ besides the networks with frequency $1376Hz$. In Fig.6.5e we can see the SPL reductions $6.4dB$ and $4.3dB$ at the targeted frequencies $1250Hz$ and $1400Hz$. New peaks can also be seen around the resonant frequencies, especially a big new peak around $1050Hz$.

Then we optimize a network for the new peak around $1050Hz$. In Fig.6.5c, we can see a new network with resonant frequencies $1034Hz$, $1754Hz$ and $1972Hz$ besides the two networks optimized before. In Fig.6.5f the peak at $1050Hz$ shifts to $1100Hz$ and its bandwidth becomes narrower. In addition, we can see two more reductions $1.2dB$ and $4.7dB$ at $1050Hz$ and $1754Hz$ thanks to the new optimized network. So

when optimizing the treads, we should choose networks with the maximum number of resonant frequencies.

When we compare the two curves in Fig.6.5f, we can see that although the maximum pressures are close, obvious reductions of acoustic pressure are obtained especially at the targeted frequencies. Furthermore, we can calculate the global reduction between the two curves in Fig.6.5f from $1000Hz$ to $2000Hz$ by equation 6.1. The global reduction is $1.5dB$.

$$GR = 10\log_{10}\frac{\sum_j P^2_{j,smooth}\Delta f_j}{\sum_j P^2_{j,network}\Delta f_j} \tag{6.1}$$

where $P_{j,smooth}$ is the pressure modulus for the smooth tire case, $P_{j,network}$ is the pressure modulus for the tread case and Δf is the frequency bandwidth.

6.2.2 Periodic networks

Through the network optimization in section 6.2.1 good results of reducing the sound pressure can be seen in Fig.6.5f. However, the network obtained in Fig.6.5c is not a periodic network in the contact zone. When the tire is rolling on the road, after a length of the contact zone emerges the optimized network. If the optimized network is a periodic network, it will emerge after a shorter rolling distance. Thus, the acoustic reductions will be better. In this section, a periodic network with the maximum number of resonant frequencies will be searched with the proposed GA procedure.

Three periodic networks with four resonant frequencies are obtained and shown in Fig.6.6a-Fig.6.6c. The acoustic pressure with and without the viscous and thermal conduction losses at receiver R is given in Fig.6.6d-6.6f. Their resonant frequencies within $2000Hz$ can be seen in table 6.1.

Table 6.1: Four resonant frequencies for the three optimized networks

Resonant frequency	**1st**	**2nd**	**3rd**	**4th**
$Network1$	$1060Hz$	$1486Hz$	$1871Hz$	$1961Hz$
$Network2$	$1034Hz$	$1245Hz$	$1803Hz$	$1920Hz$
$Network3$	$1046Hz$	$1187Hz$	$1722Hz$	$1990Hz$

From the pressure without the losses we can see a clear valley at every resonant frequency. But at some resonant frequencies the valleys of the pressure are not very clear if the losses are taken into account. In chapter 5 we know that the viscous and thermal conduction losses should be taken into account because the results with losses are closer to the experimental results.

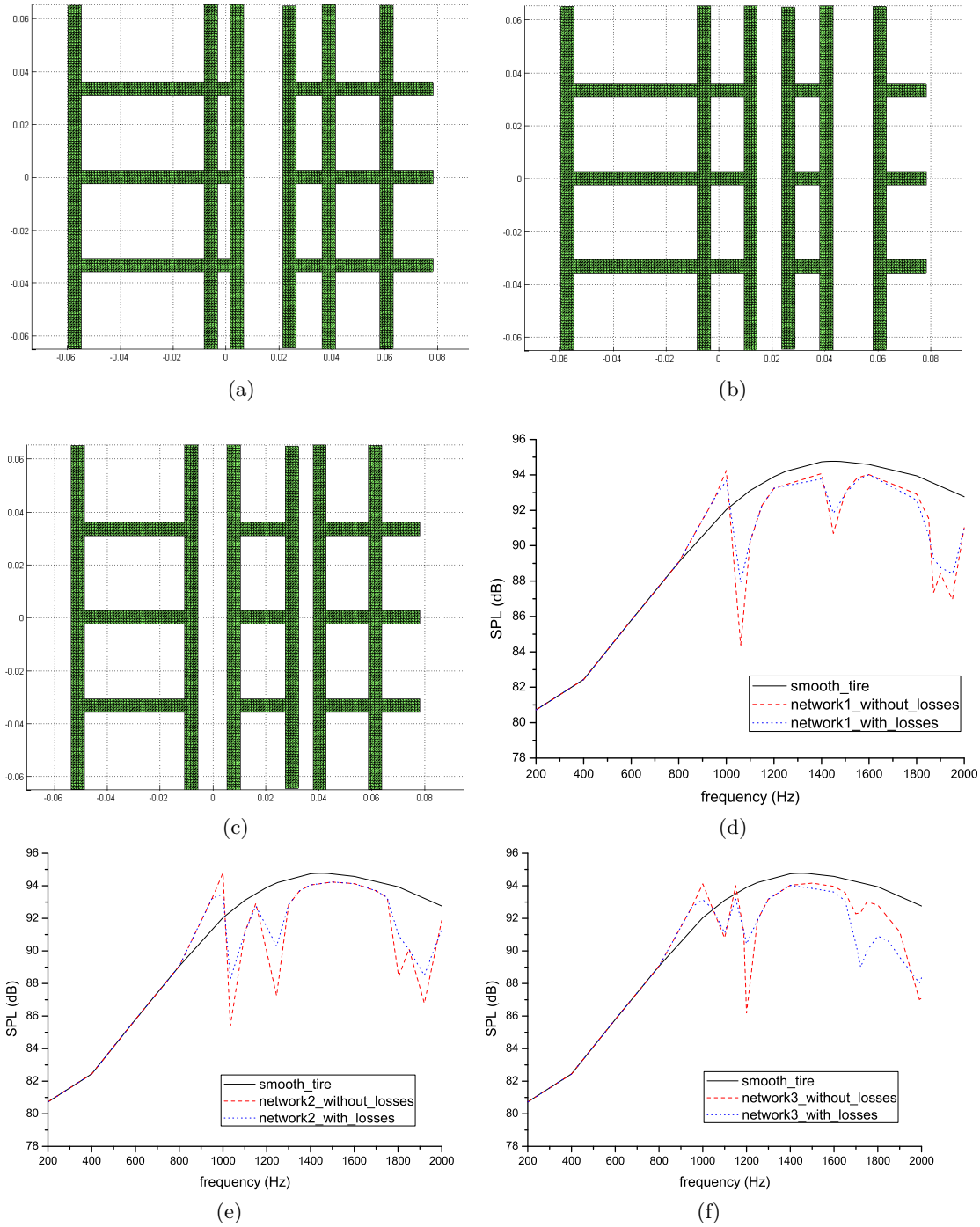

Figure 6.6: Periodic networks (including end corrections) with 4 resonant frequencies (The vertical direction is the rolling direction): (a) Network 1; (b) Network 2; (c) Network 3. SPL at R for periodic networks with 4 resonant frequencies: (d) Network 1; (e) Network 2; (f) Network 3.

Table 6.2: SPL reductions at the resonant frequencies of the three optimized networks

Network \ RF	1st	2nd	3rd	4th
$Network1$	$4.8dB$	$3dB$	$4.3dB$	$4.7dB$
$Network2$	$4.2dB$	$3.9dB$	$3dB$	$4.8dB$
$Network3$	$2dB$	$3.5dB$	$5.3dB$	$4.8dB$

Note: resonant frequency (RF)

Compared with a smooth tire without network in the contact zone, optimized networks can give pressure reductions above $1000Hz$, especially around the resonant frequencies. The SPL reductions at the resonant frequencies can be seen in table 6.2. Besides, we can calculate the global reductions for these three networks from $1000Hz$ to $2000Hz$ by equation 6.1. The global reductions are $1.5dB$, $1.5dB$ and $1.8dB$. If we compare the results of three optimized networks, it is hard to say which one is better. However, we can conclude that the more resonant frequencies the network can give, the better the network is. Because around every resonant frequency we can see obvious reductions.

The networks obtained have three rows and six columns which are the parameters given in the GA optimization. Of course we can change these parameters to see if we can get more resonant frequencies and better reductions of acoustic pressure.

Tire treads not only influence the acoustic radiations from the tire and road system, but also are essential factors for the noise generation mechanisms, such as air-pumping and vibrations. So the optimizations of tire treads are very complicated. When we design the tire treads, both the noise generation and radiation mechanisms should be taken into account. But in this work, we just investigate the impact of treads on tire and road noise from the aspect of acoustic radiation mechanisms.

In Fig.6.7, we compare three networks which have the same structure but different pipe widths, $0.005m$, $0.007m$ and $0.009m$. The network structure that we use is the network 2 in Fig.6.6b. At low frequencies, the results are almost the same, so only the results above $800Hz$ are shown in the figure. The change of pipe width does not influence the number of resonant frequencies. We can see shifts of the resonant frequencies when we compare these three cases. The lengths of the straight parts in the network are changed when the pipe width varies. It could be a reason for the shifts of the resonant frequencies. Above $1300Hz$, the smaller the width is, the larger the pressure is. Between $800Hz$ and $1300Hz$, the results are complicated, but we can see similar variations of sound pressure.

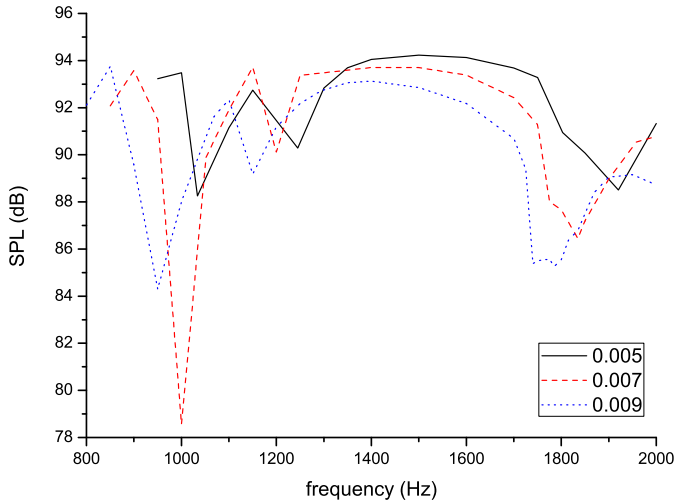

Figure 6.7: SPL at R $(1, 0, 0.265)$ for the network 2 with different cross-sections

6.3 Optimization of road textures

The road tiles texture in Fig.6.8 can also be considered as network resonators between the tire and the road. Smooth tire without treads is used in this section.

Figure 6.8: The road tiles texture

The three steps of the process in Fig.6.1 for optimizing the road textures are shown in this section. First the end corrections of the texture networks are calculated. Then the resonant frequencies of the different networks are estimated. For the optimization of the road textures, we design several networks and choose the ones with maximum resonant frequencies. The GA procedure developed in chapter 4 will not be used for the optimization of textures. Last the acoustic radiations of the chosen networks are computed by the multi-domain coupling methods.

6.3.1 Determination of end corrections

In order to estimate the resonant frequencies, the open end corrections of the networks should be obtained by the numerical methods introduced in chapter 3.

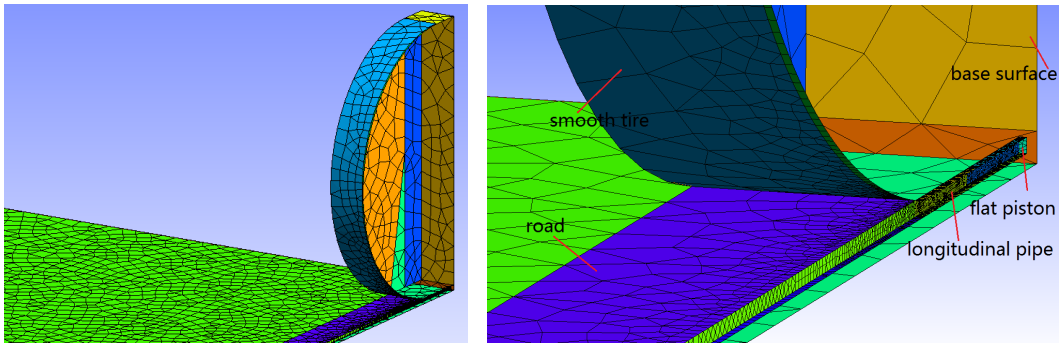

(a) (b)

Figure 6.9: (a) Half of meshes of the boundary element model of a longitudinal tube between a smooth tire and a road; (b) Details of the mesh of the model.

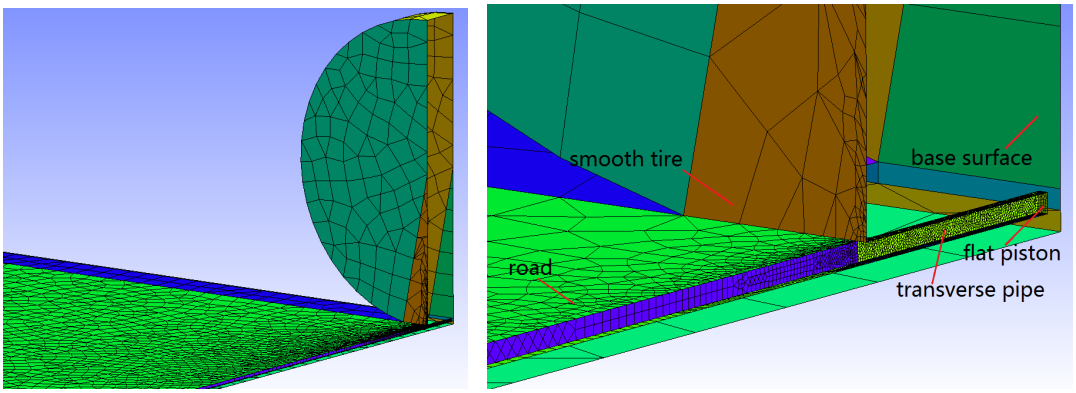

(a) (b)

Figure 6.10: (a) Half of meshes of the boundary element model of a transverse tube between a smooth tire and a road; (b) Details of the mesh of the model.

The determination of the end corrections is similar to the calculation in section 3.1.3. The surface of the smooth tire in the contact patch is flat. The meshes of the longitudinal pipe are shown in Fig.6.9a and Fig.6.9b. The longitudinal pipe is located underneath the smooth tire. The round surface of the smooth tire and the road surface are the flanges of the longitudinal end. In Fig.6.10a and Fig.6.10b we can see a transverse pipe under the smooth tire. The flanges of the end of the transverse pipe are the lateral surface of the tire and the road surface. The longitudinal and

transverse pipes are assumed at the center of the contact zone between the tire and the road.

The pipe has a rectangular cross-section with an area of $0.005m \times 0.005m$. The lengths of the longitudinal and transverse pipes are $0.1m$ and $0.07m$, respectively. The closed ends act as flat piston and have unity velocity as boundary conditions. The base surface behind the piston of the longitudinal pipe is modelled as flat to reduce the elements because the flange shape behind the piston has no influence on the end correction of the open end of this pipe. The base surfaces have very small impedances which are used to minimize the reflections. Other parts of the model are rigid.

The acoustic pressure at the central node of the closed end is calculated by BEM software Samray. The acoustic velocity is unity, so the impedance of the piston is obtained. Then the radiation impedance is calculated from this impedance by equation (3.2).

The end corrections of the longitudinal pipe under the smooth tire of different widths are shown in Fig.6.11a, and the frequency interval is $200Hz$. The tire radius is $0.27m$. For each width of the tire, the end corrections are frequency-dependent, but their standard deviations are very small (see Fig.6.11b), which indicates that they tend to be very close to the mean values. The standard deviation is calculated by equation (3.4). So the mean values of end corrections for each width in Fig.6.11b are used to get a fit formula of end corrections, in which w is half of the width.

$$\delta = 0.00743 + 0.24995w - 4.625w^2 + 27.7778w^3 \tag{6.2}$$

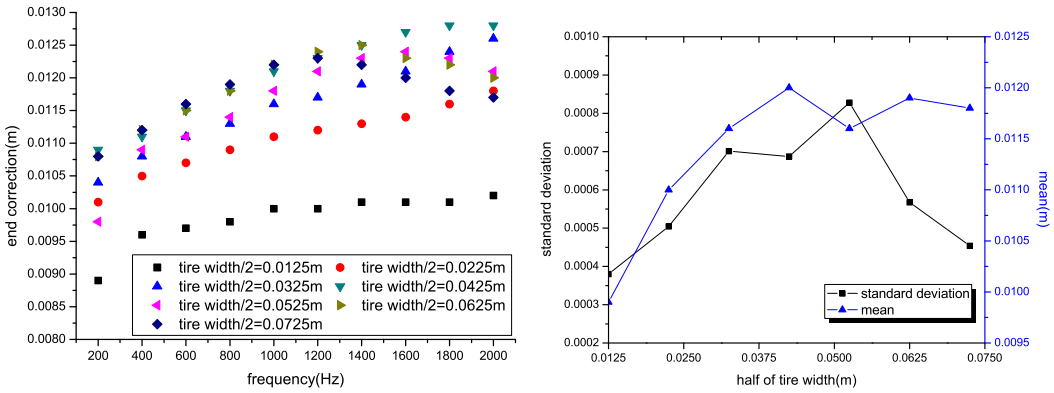

(a) (b)

Figure 6.11: (a) End corrections of longitudinal pipes under tires of different widths within $2000Hz$; (b) Standard deviations and mean values of end corrections of longitudinal pipes under tires of different widths.

The end corrections of the transverse pipe in the middle of the contact zone under the smooth tire are shown in Fig.6.12, and the frequency interval is $200Hz$. The

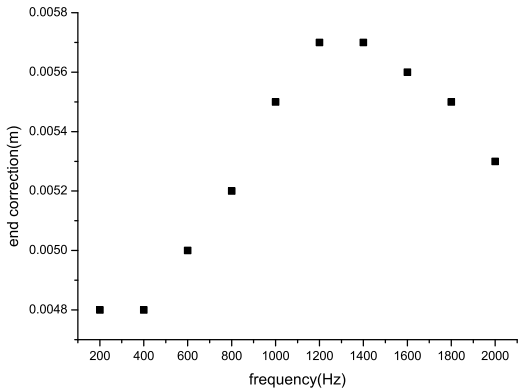

Figure 6.12: End corrections of the transverse pipe in the middle of the contact zone under the tire within $2000Hz$.

standard deviation of the end corrections is very small $3.48 \times 10^{-4}m$, which indicates that they tend to be very close to the mean value $0.0053m$. So the mean value can be used to estimate the resonant frequencies within $2000Hz$. The standard deviation is calculated by equation (3.4).

6.3.2 Estimation of resonant frequencies

For the optimization of the tire treads, GA procedure proposed in chapter 4 is used. The optimized networks with the wanted resonant frequencies are obtained. For the optimization of the road texture, if we use GA we can get similar results. Because both the road textures and tire treads are networks in the contact zone. So in this part, we investigate some simple road textures. We compare the number of the resonant frequencies of these networks and find the one with maximum number of resonant frequencies.

The textures that we study have the same pattern, but different dimensions. The texture junctions are cross junctions. An example of the texture is shown in Fig.6.13. The texture is a periodic network in the directions of x and y axes. The network has the same symmetry axes (x and y axes) as the contact zone. In Fig.6.13, there are two columns and three rows of the network in the contact zone. By changing the distances $D1$ and $D2$ between the adjacent columns and rows of the network, different networks can be obtained, which have different number of the columns and rows in the contact zone. Two parameters, n_c and n_r, represent the number of the columns and rows of the network in the contact zone, and vary in the vectors $[2, 4, 6, 8, 10]$ and $[1, 2, 3, 4, 5]$. We can get 25 networks with different resonant frequencies.

The resonant frequencies can be estimated by the program 2DNRF developed in

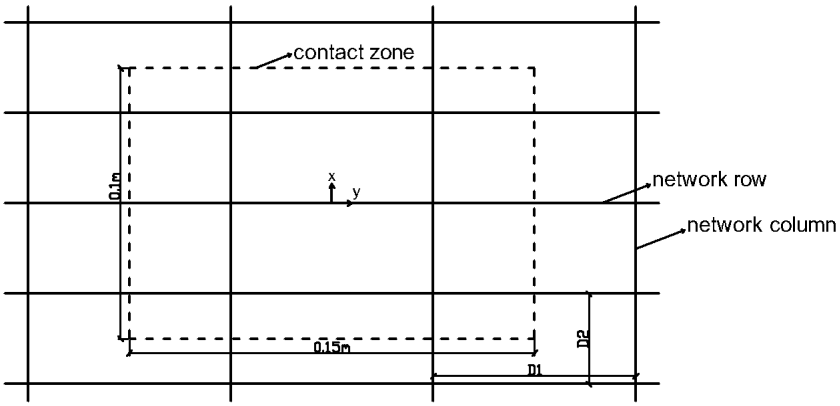

Figure 6.13: Road texture in the contact zone

Table 6.3: The number of resonant frequencies of networks with different number of columns and rows

Nc \ Nr	1	2	3	4	5
2	1	2	3	3	3
4	1	1	1	2	2
6	2	1	1	1	1
8	2	1	1	1	1
10	2	1	1	1	1

Note: the number of columns (Nc), the number of rows (Nr)

chapter 3. The number of the resonant frequencies of the networks with different number of columns and rows are shown in table 6.3. There are three networks with 3 resonant frequencies. Their resonant frequencies are given in table 6.4. From the optimization of the tire treads, we know that the networks with a maximum number of resonant frequencies give better results of reducing the acoustic radiations. So the three networks with 3 resonant frequencies are better than the others.

Table 6.4: The resonant frequencies of networks with 2 columns and $3-5$ rows

(Nc,Nr) \ RF	1st	2nd	3rd
$(2,3)$	$1213Hz$	$1657Hz$	$1888Hz$
$(2,4)$	$1200Hz$	$1615Hz$	$1893Hz$
$(2,5)$	$1190Hz$	$1574Hz$	$1868Hz$

Note: the number of columns (Nc), the number of rows (Nr), resonant frequencies (RF)

6.3.3 Road dimensions

The road in the calculation of acoustic radiations of tire treads is a rigid plane surface. So it can be considered as a symmetric plane and no mesh is needed for the road. But in the calculation of the acoustic radiation of the road textures, the road should be meshed in order to simulate the road textures. Therefore, the road dimensions should be studies in order to reduce the meshes of the road and the computational time.

A longitudinal straight pipe at the center of the contact zone under the smooth tire simulates the road texture. The acoustic fields are calculated by the multi-domain coupling methods BEMT (BEM is used for the exterior subdomain and transfer matrix is used for the interior subdomain which is the straight pipe) developed in chapter 2. So no mesh for the pipe is needed. The BEM meshes of the tire and road are shown in Fig.6.14a. The source and receiver, which can be seen in Fig.6.2a, are at $(0.1, 0, 0.005)$ and $(1, 0, 0.06)$.

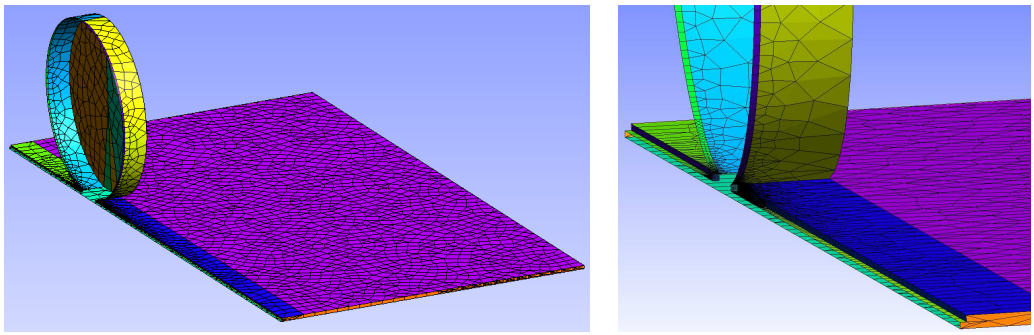

(a) (b)

Figure 6.14: (a) Meshes of half the boundary element model of a longitudinal pipe at the center of the contact zone between a smooth tire and a road; (b) Details of the meshes of the model.

Table 6.5: The modulus of the sound pressure at the receiver for different dimensions of the road

$(l_1, l_2, w)/m$	**modulus**	**error**	$(l_1, l_2, w)/m$	**modulus**	**error**
$(1, 1, 1)$	0.7076	–	$(1.35, 1.35, 1.35)$	0.5974	–
$(1.35, 1.35, 1.35)$	0.5974	18.5%	$(0.55, 1.35, 1.35)$	0.5941	0.6%
$(1.55, 1.55, 1.55)$	0.6217	3.9%	$(0.55, 1.35, 1.075)$	0.5895	0.8%

We change the dimensions of the road and compare the sound pressure at the receiver at $1300Hz$ which is close to the first resonant frequency of the pipe. The smallest dimension with good results at the receiver will be used in the following calculations. The dimension of the road can be seen in Fig.6.15. The results for the

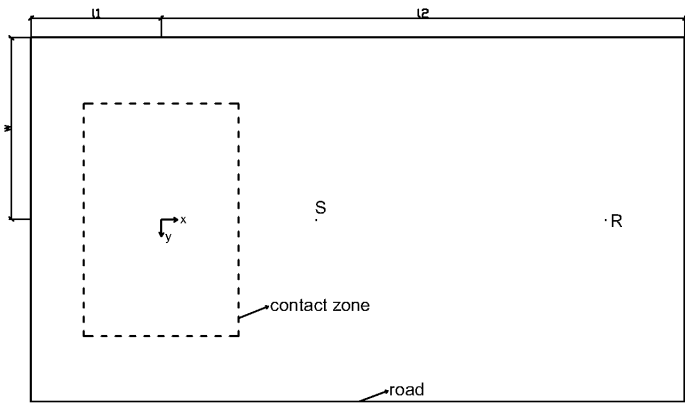

Figure 6.15: Road dimensions

different dimensions of the road are shown in table 6.5. In each column of the modulus of the sound pressure, we compare the modulus with the one above. In the left part of the table, the dimension $(1.35, 1.35, 1.35)m$ is chosen. Then it is compared with smaller dimensions in the right part of the table. The dimension $(0.55, 1.35, 1.075)m$ can give good results and it is small, so it will be used in the calculations of sound fields.

6.3.4 Calculation of acoustic radiations

In this section, we choose the first texture with 3 resonant frequencies within $2000Hz$ in table 6.4, calculate the sound pressure at $(1, 0, 0.265)m$ within $2000Hz$, and compare with the case of the smooth road in order to show the influence of the road texture on the acoustic radiation. In this texture, there are two columns and three rows.

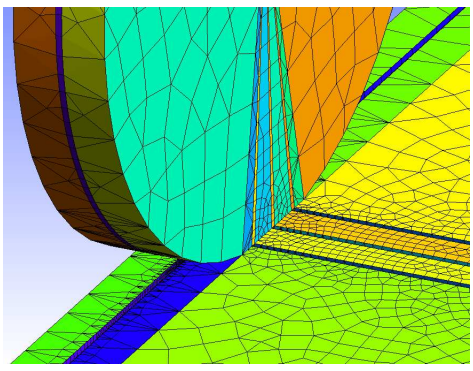

Figure 6.16: Meshes of half the boundary element model of the texture with 2 columns and 3 rows under the smooth tire

The multi-domain methods A2BEM proposed in chapter 2 are used to do the

calculations. The BEM meshes are shown in Fig.6.16. The results can be seen in Fig.6.17. Around the three resonant frequencies we can see the clear SPL reductions $2.1dB$, $2.9dB$ and $1dB$.

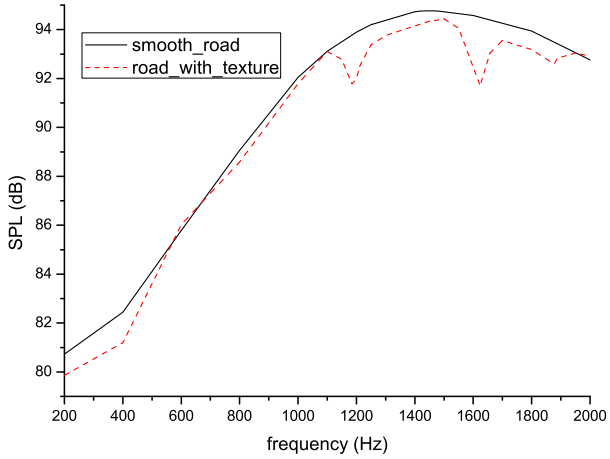

Figure 6.17: SPL at R $(1, 0, 0.265)m$ for the network with 2 columns and 3 rows

6.4 Conclusions

The influence of the network on the acoustic fields can be seen under both of the two types of excitations, the point source and the velocities on the tire surface.

Two ways of the optimization of the tire treads are introduced in this chapter. By inserting several networks with targeted resonant frequencies, the original wide-band peak of the sound pressure within $2000Hz$ becomes a narrow-band peak, and multiple reductions of sound pressure at resonant frequencies can be achieved. The second way is optimizing and designing the periodic networks with the maximum number of resonant frequencies. We can get good reductions of the sound pressure similar to results of the first way. Since periodic tire treads can cause the periodic vibrations of the tire, small transverse pipes without connecting to the optimized network should be inserted into the spaces between the optimized network. The cross-sectional area can result in the shifts of the resonant frequencies, but has no influence on the number of the resonant frequencies.

The same optimization methods as used for the tire treads can be applied to the design of the road texture. Similar conclusions can be obtained, because the road textures are also the network between the tire and the road. So for the road texture, we only investigated the influence of the dimensions of the bricks in the contact zone on the number of resonant frequencies. The optimized dimensions of the bricks with

a maximum number of resonant frequencies are obtained.

Based on the studies in this chapter, we know that by optimizing the networks between the tire and the road, the sound pressure fields can be improved. So we can use the network to reduce the sound pressures at its resonant frequencies.

Chapter 7

Conclusions and future work

7.1 Conclusions

Tire/road noise is the dominant source of the noise from the cars at speeds above approximately $50kph$ for properly maintained automobiles [1]. Many researches have been done to reduce the noise. The generation and radiation mechanisms of the noise are presented and studied by a lot of researchers. However, the horn effect and the pipe resonances, which are two noise radiation mechanisms, should be taken into account in the same model. Thus, new designs of the tire treads and road texture can be found for the noise reduction. In this work, design methods for the tire treads and road textures and computational methods for the noise reduction are developed.

The tire treads and road textures can be seen as the networks in the contact zone between the tire and the road. Around the resonant frequencies, the amplification of the sound pressure by the horn effect can be reduced by the networks. So numerical methods for the calculation of the resonant frequencies of the network are developed. Since the network has open ends for which the end correction should be taken into account when we calculate the resonant frequencies, numerical methods for the determination of the end corrections of the pipes with arbitrary flanges are proposed. In order to reduce the amplification of the horn effect around the wanted resonant frequencies, an optimization method of the network structure based on the genetic algorithm is developed. By optimizing the junction types and the positions of the network, we can get the network with wanted resonant frequencies. The more resonant frequencies the network has within $2000Hz$, the more reductions of the amplifications can be obtained. Therefore, we can also use the optimization methods to design networks with maximum number of the resonant frequencies within $2000Hz$. The tire/road system and the networks in the contact zone can be considered as the

flanged networks. In order to estimate the value of the reduction, multi-domain coupling methods are developed. The network in the contact zone is a two dimensional structure. The multi-domain coupling methods can also be applied to solve three dimensional networks with arbitrary flanges.

The methods proposed in this work are validated with measurements. First we use a wooden cylinder and several wooden networks to compare the predicted results obtained by the methods introduced before and the measured results. The availability and effectiveness of the methods are proved by good agreements. Then a real tire is measured and calculated. Since it is difficult to estimate the dimension of the network in the contact zone, the agreements between the predicted and measured results are not as perfect as the agreements in the wooden cases. But based on the results that we have, we can still conclude that the resonances of the networks can reduce the amplification around the resonant frequencies, and the methods that we developed can be applied to the design and optimization of the tire treads and the road textures.

The systematic analysis tools developed for the flanged networks are used for the real tire and road. By optimizing the tire treads, multiple reductions of the amplification of the horn effect can be seen. Two types of optimized tire treads are obtained. In the first optimization, we optimize the treads for the targeted resonant frequencies, and for the second type the treads are optimized to get the periodic structures with the maximum number of resonant frequencies. Since the tire treads also influence other noise generation mechanisms, such as air-pumping and tire vibration, we can not give the optimal tire treads from the aspect of noise radiation. The systematic analysis tools should be used together with other design tools for other mechanisms. Otherwise, the networks that we design maybe cause other enhancement of the noise, for example tire vibrations.

For the road textures, we can get the similar conclusions as for the tire treads, because both of them can be seen as the networks in the contact zone. So only the dimension of the road bricks in the contact zone is studied. Then we choose the texture with maximum resonant frequencies to estimate the influence on the horn effect. We can see the reductions of amplifications of the horn effect by the texture around the resonant frequencies.

7.2 Future work

From the aspect of the tire/road noise radiation, systematic analysis tools of the tire treads and road textures for the reductions of the amplifications of the horn effect are developed. Based on the present work, future work can be continued:

(1) The road in this work is modeled as the rigid surface. Porous road should be taken into account in the model.

(2) In the multi-domain coupling method, the equations for two dimensional networks are only suitable for the networks with square junctions. These equations should be developed for the rectangular junctions.

(3) Besides the horn effect and the pipe resonances, more mechanism should be studied together in order to reduce the tire/road noise.

(4) More possible applications of the network resonators should be explored for the noise control.

Bibliography

[1] Robert Bernhard, Roger L Wayson, John Haddock, Narayanan Neithalath, Ahmed El-Aassar, Jan Olek, Terhi Pellinen, and W Jason Weiss. An introduction to tire/pavement noise of asphalt pavement. *Institute of Safe, Quiet and Durable Highways, Purdue University*, 2005.

[2] John W Miles. The diffraction of sound due to right-angled joints in rectangular tubes. *The Journal of the Acoustical Society of America*, 19(4):572–579, 1947.

[3] J-P Dalmont, CJ Nederveen, and N Joly. Radiation impedance of tubes with different flanges: numerical and experimental investigations. *Journal of sound and vibration*, 244(3):505–534, 2001.

[4] Ulf Sandberg and Jerzy A Ejsmont. *Tyre/road noise reference book*. INFORMEX, 2002.

[5] Birgitta Berglund, Thomas Lindvall, Dietrich H Schwela, et al. Guidelines for community noise. In *Guidelines for community noise*. OMS, 1999.

[6] OECD-ECMT. Urban travel and sustainable development. *European conference of ministers of transport, organisation for economic co-operation and development, Paris, France.*, 1995.

[7] J. Lambert and M. Vallet. Study related the preparation of a communication on a future ec noise policy(report no. len 9420, december 1994). *INRETS, Bron Cedex, France*, 1994.

[8] MJ Gagen. Novel acoustic sources from squeezed cavities in car tires. *The Journal of the Acoustical Society of America*, 106(2):794–801, 1999.

[9] Ulf Sandberg. The multi-coincidence peak around 1000 hz in tyre/road noise spectra. In *Euronoise conference, paper ID*, volume 498, 2003.

[10] JF Hamet. Reduction of tire road noise by acoustic absorption: numerical evaluation of the pass-by noise level reduction using the normal incidence acoustic absorption coefficient. 2004.

[11] J Perisse. A study of radial vibrations of a rolling tyre for tyre–road noise characterisation. *Mechanical Systems and Signal Processing*, 16(6):1043–1058, 2002.

[12] K Larsson and W Kropp. A high-frequency three-dimensional tyre model based on two coupled elastic layers. *Journal of sound and vibration*, 253(4):889–908, 2002.

[13] U Nackenhorst. The ale-formulation of bodies in rolling contact: Theoretical foundations and finite element approach. *Computer Methods in Applied Mechanics and Engineering*, 193(39):4299–4322, 2004.

[14] Tatsuo Fujikawa, Hiroshi Koike, Yasuo Oshino, and Hideki Tachibana. Definition of road roughness parameters for tire vibration noise control. *Applied acoustics*, 66(5):501–512, 2005.

[15] IF Kozhevnikov. The vibrations of a free and loaded tyre. *Journal of applied mathematics and mechanics*, 70(2):223–228, 2006.

[16] E Rustighi and SJ Elliott. Stochastic road excitation and control feasibility in a 2d linear tyre model. *Journal of Sound and Vibration*, 300(3):490–501, 2007.

[17] Byoung Sam Kim, Gi Jeon Kim, and Tae Keun Lee. The identification of sound generating mechanisms of tyres. *Applied Acoustics*, 68(1):114–133, 2007.

[18] JF Hamet and Ph Klein. Evaluation of tire road noise from road texture profiles using inrets rolling tire model: Evaluation from a profile measured by the lcpc. 2004.

[19] Richard E Hayden. Roadside noise from the interaction of a rolling tire with the road surface. *The Journal of the Acoustical Society of America*, 50(1A):113–113, 1971.

[20] C Deffayet et al. Air-pumping phenomena in road cavities. In *INTROC 90-International Tire/Road Noise Conference 1990, Gothenburg, Sweden*, 1990.

[21] D Ronneberger. Experimentelle und theoretische untersuchungen spezieller mechanismen der rollgeräusche. *Mitteilungen des Instituts für Straßen-, Eisenbahn-und Felsbau an der ETH Zürich*, 57:55, 1984.

[22] D. RONNEBERGER. Towards quantitative prediction of tyre/road noise. In *workshop on rolling noise generation, Institut fur Technische Akustik, Technische Universitat Berlin.*, 1989.

[23] W. Kropp, F.X. Becot, and S. Barrelet. On the sound radiation from tyres. *Acta Acustica united with Acustica*, 86(5):769–779, 2000.

[24] RAG Graf, CY Kuo, AP Dowling, and WR Graham. Horn amplification at a tyre/road interface-part i: experiment and computation. In *Proceedings of internoise 99-the 1999 international congress on noise control engineering held in fort lauderdale, Florida, USA, 6-8 December 1999, volume 1*, 1999.

[25] RAG Graf, C.Y. Kuo, AP Dowling, and WR Graham. On the horn effect of a tyre/road interface, part i: Experiment and computation. *Journal of Sound and Vibration*, 256(3):417–431, 2002.

[26] C.Y. Kuo, RAG Graf, AP Dowling, and WR Graham. On the horn effect of a tyre/road interface, part ii: Asymptotic theories. *Journal of sound and vibration*, 256(3):433–445, 2002.

[27] Fabienne Anfosso-Ledee. Tyre / road noise horn effect : 2d modelling by analytical and numerical models. Technical report, national PREDIT project, 2000.

[28] F. Anfosso-Ledee, P. Klein, A. Fadavi, and D. Duhamel. Tire/road noise: comparison of 2d and 3d models for horn effect. In *Internoise 2000. Proceedings of the 29th international congress on noise control engineering, held 27-31 August 2000, Nice, France.*, volume 1, 2000.

[29] A. Fadavi. Tire/road noise: 3d model for horn effect. In *The 29th International Congress and Exhibition on Noise Control Engineering*, 2000.

[30] W.K. Lui and K.M. Li. A theoretical study for the propagation of rolling noise over a porous road pavement. *The Journal of the Acoustical Society of America*, 116:313, 2004.

[31] C. Zwikker and C.W. Kosten. *Sound Absorbing Materials: by C. Zwikker and C.W. Kosten*. Elsevier Publishing Company, 1949.

[32] H Tijdeman. On the propagation of sound waves in cylindrical tubes. *Journal of Sound and Vibration*, 39(1):1–33, 1975.

[33] Fredericus Joseph Marie Eerden. *Noise reduction with coupled prismatic tubes*. University of Twente, 2000.

[34] CD Field and FR Fricke. Theory and applications of quarter-wave resonators: A prelude to their use for attenuating noise entering buildings through ventilation openings. *Applied Acoustics*, 53(1):117–132, 1998.

[35] William M Ihde. Tuning stubs to silence large air handling systems. *Noise Control Engineering*, 5(3):131–136, 1975.

[36] W Neise and GH Koopmann. Reduction of centrifugal fan noise by use of resonators. *Journal of Sound and Vibration*, 73(2):297–308, 1980.

[37] GH Koopmann and W Neise. The use of resonators to silence centrifugal blowers. *Journal of Sound and Vibration*, 82(1):17–27, 1982.

[38] Z Zhu, Y Li, and S Fang. Experimental investigation of centrifugal fan noise by use of resonator and theoretic analysis of resonance frequency. In *Proceedings of Internoise'86 Congress*, pages 199–203, 1986.

[39] Kyoji Fujiwara. Sound shielding efficiency of a barrier with soft surface. *Proc. Inter Noise 90*, pages 343–346, 1990.

[40] K Fujiwara and T Ohkubo. Sound shielding efficiency of a noise barrier with soft surface and soft round obstacle at the edge. In *Proceedings of the 15th International Congress on Acoustics*, pages 97–100, 1995.

[41] Kyoji Fujiwara, David C Hothersall, and Chul-hwan Kim. Noise barriers with reactive surfaces. *Applied acoustics*, 53(4):255–272, 1998.

[42] C. D. Field and F. R. Fricke. The attenuation of noise entering buildings using quarter-wave resonators. *Proceedings of the Australian Acoustical Society Annual Conference 1995*, pages 131–134, 1995.

[43] C. D. Field and F. R. Fricke. A multiple quarter-wave resonator system for the attenuation of noise entering buildings through ventilation openings. *Proceedings of Internoise '96 Congress*, pages 1769–1772, 1996.

[44] C. D. Field and F. R. Fricke. Ventilation of buildings located in noisy environments. *Proceedings of the 15th International Congress on Acoustics*, 1995.

[45] Bradley W Ross and Ricardo A Burdisso. Low frequency passive noise control of a piston structure with a weak radiating cell. *The Journal of the Acoustical Society of America*, 106(1):226–232, 1999.

[46] Marieke Henriette Cathrien Hannink. *Acoustic resonators for the reduction of sound radiation and transmission*. University of Twente, 2007.

[47] FJ Fahy and C Schofield. A note on the interaction between a helmholtz resonator and an acoustic mode of an enclosure. *Journal of Sound and Vibration*, 72(3):365–378, 1980.

[48] WV Slaton and JCH Zeegers. Acoustic power measurements of a damped aeroacoustically driven resonatora). *The Journal of the Acoustical Society of America*, 118(1):83–91, 2005.

[49] A Cummings. The effects of a resonator array on the sound field in a cavity. *Journal of Sound and Vibration*, 154(1):25–44, 1992.

[50] A Doria. Control of acoustic vibrations of an enclosure by means of multiple resonators. *Journal of Sound and Vibration*, 181(4):673–685, 1995.

[51] Octávio Inácio, Lui Henrique, José Antunes, et al. Design of duct cross sectional areas in bass-trapping resonators for control rooms. *Noise control engineering journal*, 55(2):172–182, 2007.

[52] P Merkli. Acoustic resonance frequencies for a t-tube. *Zeitschrift für angewandte Mathematik und Physik ZAMP*, 29(3):486–498, 1978.

[53] Deyu Li and Jeffrey S Vipperman. On the design of long t-shaped acoustic resonators. *the Journal of the Acoustical Society of America*, 116(5):2785–2792, 2004.

[54] Deyu Li. *VIBROACOUSTIC BEHAVIOR AND NOISE CONTROL STUDIES OFADVANCED COMPOSITE STRUCTURES*. PhD thesis, University of Pittsburgh, 2003.

[55] Ganghua Yu. *Acoustic resonators for noise control in enclosures: modelling, design and optimization*. PhD thesis, The Hong Kong Polytechnic University, 2009.

[56] Deyu Li and Jeffery S Vipperman. Noise control of mock-scale chambercore payload fairing using integrated acoustic resonators. *Journal of spacecraft and rockets*, 43(4):877–882, 2006.

[57] Steven A Lane, Robert E Richard, and Scott J Kennedy. Fairing noise control using tube-shaped resonators. *Journal of spacecraft and rockets*, 42(4):640–646, 2005.

[58] MA Jaswon and MA Jaswon. Integral equation methods in potential theory. i. *Proceedings of the Royal Society of London. Series A. Mathematical and Physical Sciences*, 275(1360):23–32, 1963.

[59] F. J. Rizzo. An integral equation approach to boundary value problems of classical elastostatics. *Q. Appl. Math*, 25:83–95, 1967.

[60] AJ Burton and GF Miller. The application of integral equation methods to the numerical solution of some exterior boundary-value problems. *Proceedings of the Royal Society of London. A. Mathematical and Physical Sciences*, 323(1553):201–210, 1971.

[61] Y. Liu. *Fast multipole boundary element method*. Cambridge university press, 2009.

[62] J. Barnes and P. Hut. A hierarchical 0 (n log iv) force-calculation algorithm. *nature*, 324:4, 1986.

[63] V. Rokhlin. Rapid solution of integral equations of classical potential theory. *Journal of Computational Physics*, 60(2):187–207, 1985.

[64] L. Greengard and V. Rokhlin. A fast algorithm for particle simulations. *Journal of computational physics*, 73(2):325–348, 1987.

[65] J. Carrier, L. Greengard, and V. Rokhlin. A fast adaptive multipole algorithm for particle simulations. *SIAM Journal on Scientific and Statistical Computing*, 9(4):669–686, 1988.

[66] V. Rokhlin. Diagonal forms of translation operators for helmholtz equation in three dimensions. Technical report, DTIC Document, 1992.

[67] L. Greengard and V. Rokhlin. A new version of the fast multipole method for the laplace equation in three dimensions. *Acta numerica*, 6(1):229–269, 1997.

[68] Alexandre Jolibois. *A study on the acoustic performance of tramway low-height noise barriers: gradient-based numerical optimization and experimental approaches*. PhD thesis, Paris Est, 2013.

[69] Young-Bum Park, Hyeon-Don Ju, and Shi-Bok Lee. Transmission loss estimation of three-dimensional silencers by system graph approach using multi-domain boundary element method. *Journal of Sound and Vibration*, 328(4):575–585, 2009.

[70] Ting-Wen Wu. Multi–domain boundary element method in acoustics. In *Computational Acoustics of Noise Propagation in Fluids-Finite and Boundary Element Methods*, pages 367–386. Springer, 2008.

[71] C.A. Brebbia and S. Walker. *Boundary Element Techniques in Engineering*. Newnes-Butterworths, 1980.

[72] C. R. Cheng. *Boundary Element Analysis of Single and Multidomain Problems in Acoustics*. PhD thesis, University of Kentucky., 1988.

[73] H. Utsuno, T. W. Wu, A. F. Seybert, and T. Tanaka. Prediction of sound fields in cavities with sound absorbing materials. *AIAA Journal*, 28:1870–1876, November 1990.

[74] CYR Cheng, AF Seybert, and TW Wu. A multidomain boundary element solution for silencer and muffler performance prediction. *Journal of Sound and Vibration*, 151(1):119–129, 1991.

[75] Chao-Nan Wang, Chuan-Cheung Tse, and Yih-Nan Chen. A boundary element analysis of a concentric-tube resonator. *Engineering analysis with boundary elements*, 12(1):21–27, 1993.

[76] Manchar Lal Munjal and ML Munjal. *Acoustics of ducts and mufflers with application to exhaust and ventilation system design*. Wiley New York (NY) et al., 1987.

[77] A Craggs and DC Stredulinsky. Analysis of acoustic wave transmission in a piping network. *The Journal of the Acoustical Society of America*, 88:542, 1990.

[78] G Lou, TW Wu, and CYR Cheng. Boundary element analysis of packed silencers with a substructuring technique. *Engineering Analysis with Boundary Elements*, 27(7):643–653, 2003.

[79] Denis Duhamel. *L'acoustique des problèmes couples fluide-structure-Application au contrôle actif du son*. PhD thesis, Ecole des Ponts ParisTech, 1994.

[80] Lawrence E Kinsler, Austin R Frey, Alan B Coppens, and James V Sanders. Fundamentals of acoustics. *Fundamentals of Acoustics, 4th Edition, by Lawrence E. Kinsler, Austin R. Frey, Alan B. Coppens, James V. Sanders, pp. 560. ISBN 0-471-84789-5. Wiley-VCH, December 1999.*, 1, 1999.

[81] 杜功焕. 声学基础, 2012.

[82] John W Miles. The analysis of plane discontinuities in cylindrical tubes. part i. *The Journal of the Acoustical Society of America*, 17(3):259–271, 1946.

[83] John W Miles. The analysis of plane discontinuities in cylindrical tubes. part ii. *The Journal of the Acoustical Society of America*, 17(3):272–284, 1946.

[84] Louis V King. Vi. on the electrical and acoustic conductivities of cylindrical tubes bounded by infinite flanges. *The London, Edinburgh, and Dublin Philosophical Magazine and Journal of Science*, 21(138):128–144, 1936.

[85] Harold Levine and Julian Schwinger. On the radiation of sound from an unflanged circular pipe. *Physical review*, 73(4):383, 1948.

[86] Yûkichi Nomura, Ichirô Yamamura, and Sakari Inawashiro. On the acoustic radiation from a flanged circular pipe. *Journal of the Physical Society of Japan*, 15(3):510–517, 1960.

[87] Arthur H Benade and JS Murday. Measured end corrections for woodwind toneholes. *The Journal of the Acoustical Society of America*, 41(6):1609–1609, 1967.

[88] MCAM Peters, Avraham Hirschberg, AJ Reijnen, and APJ Wijnands. Damping and reflection coefficient measurements for an open pipe at low mach and low helmholtz numbers. *Journal of Fluid Mechanics*, 256:499–534, 1993.

[89] Y Ando. On the sound radiation from semi-infinite circular pipe of certain wall thickness. *Acta Acustica united with Acustica*, 22(4):219–225, 1969.

[90] AN Norris and IC Sheng. Acoustic radiation from a circular pipe with an infinite flange. *Journal of Sound and Vibration*, 135(1):85–93, 1989.

[91] Deyu Li. *Vibroacoustic behavior and noise control studies of advanced composite structures*. PhD thesis, University of Pittsburgh, 2003.

[92] Lord Rayleigh. The theory of sound, 1894. *Republished by Dover Publications, New York*, 1945.

[93] James Edward Baker. Adaptive selection methods for genetic algorithms. In *Proceedings of an International Conference on Genetic Algorithms and their applications*, pages 101–111. Hillsdale, New Jersey, 1985.

[94] Byung-Joo Jin, Hyun-Sil Kim, Hyun-Ju Kang, and Jae-Seung Kim. Sound diffraction by a partially inclined noise barrier. *Applied acoustics*, 62(9):1107–1121, 2001.

[95] A Cummings. The effects of a resonator array on the sound field in a cavity. *Journal of Sound and Vibration*, 154(1):25–44, 1992.

[96] P. Klein J.M. Clairet. Mesures d'amplification par effet dièdre pneumatique sculpté/sol lisse. *Rapport*, 2015.

[97] Ali Fadavi. *Modélisation numérique des vibrations d'un pneumatique et de la propagation du bruit de contact*. PhD thesis, Ecole Nationale des Ponts et Chaussées, 2002.